Bergische Universität Wuppertal
Fakultät 4 - Mathematik und
Naturwissenschaften

BERGISCHE
UNIVERSITÄT
WUPPERTAL

Measurement of electroweak W + Jets Production and Search for anomalous Triple Gauge Boson Couplings with the ATLAS Experiment at $\sqrt{s} = 8\,\mathrm{T}e\mathrm{V}$

Dissertation zur Erlangung des Grades
Doktor der Naturwissenschaften (Dr. rer. nat)

vorgelegt der
Bergischen Universität Wuppertal
Fakultät 4: Mathematik und Naturwissenschaften

von
Julia Fischer

Erstgutachter: *Prof. Dr. Christian Zeitnitz*
Zweitgutachterin: *PD. Dr. Ulrike Blumenschein*

Wuppertal, 6. Mai 2016

Contents

1 — Introduction

The glory of friendship is not the outstretched hand,
not the kindly smile, nor the joy of companionship;
it is the spiritual inspiration that comes to one
when you discover that someone else believes in you
and is willing to trust you with a friendship.
- Ralph Waldo Emerson

The frontiers of physics are driven by the study of nature. Physicists want to understand what the world is made of and therefore study the phenomena of subatomic particles at very small scales up to very large scales in the Astrophysics. To describe the known fundamental particles and their interactions a powerful theory was developed, the so-called Standard Model of particle physics (SM), which is based on the fundamental ideas of quantum field theory. The SM was probed in the previous decades in numerous tests of various experiments confirming its predictions to high precision. The deeper physicists look into matter to understand what it is built of, the higher are the energies that are needed in the experiments.

With the Large Hadron Collider (LHC) the most powerful particle accelerator that has ever been built, started its regular operation in 2010. A successful Run I was performed with center-of-mass energies of $\sqrt{s} = 7\,\mathrm{TeV}$ in 2010 and 2011 as well as $\sqrt{s} = 8\,\mathrm{TeV}$ in 2012. About $25\,\mathrm{fb}^{-1}$ of data were recorded by the main experiments A Toroidal LHC ApparatuS (ATLAS) and Compact Muon Solenoid (CMS) in these two years, which made it possible to address the first main goal of the LHC by discovering a new spin-0 particle with a mass of approximately $125\,\mathrm{GeV}$. Today, this particle is identified with the Higgs boson, which was the last missing piece of the SM. The Higgs boson has been predicted first in the 1960's and its existence is essential for the SM, as the coupling of the fundamental particles to the Higgs field provides their masses.

The discovery of the Higgs-like boson is a huge success on the way to confirm the SM as a quantum field theory being able to describe the dynamics of the elementary particles. Nevertheless, the properties of the new boson have to be studied in detail, to confirm that is it really the Higgs boson that is predicted by the theory. Therefore, at the experiments at the LHC the measurement of the production and the decay of the Higgs-like boson as well as its further properties continues. Moreover there are observations in nature which cannot be explained by the SM, for example the overwhelming amount of dark energy and

dark matter that is found in the universe. Therefore, also the search for new physics that extends the SM theory, continues. A well established concept is the SM being a low energy approximation of a more general theory, which can explain all discovered phenomena. Besides direct searches for new (heavy) particles, the interactions of the known particles are tested for new unexpected phenomena. An important coupling in this respect is the vertex of three vector bosons, $WWZ/WW\gamma$. This coupling is precisely predicted in the SM and can be tested for deviations from the theory.

In this thesis the production of two jets in association with a W boson as a pure electroweak process is measured. In this process the W boson can be produced by the fusion of two heavy vector bosons, a so-called Vector Boson Fusion (VBF) process. The event topology consists of two high energy forward jets and a centrally produced W boson. Besides the W boson, also the Higgs boson and the Z boson can be produced via VBF. Common property is the event characteristics of two forward jets. The production via VBF is the second most frequent production mode of the Higgs boson and thus an important test to confirm that the observed particle is indeed the Higgs boson. The electroweak (EW) production of a W boson in association with two jets has a larger cross section than the Higgs production and therefore is the optimal channel to probe VBF production, in turn this knowledge can be used to improve the measurement of the Higgs boson.

Furthermore, the VBF coupling of the electroweak dijet production in association with a W boson contains a vertex of the three vector bosons $WWZ/WW\gamma$. Therefore, this process can be used to probe the SM prediction for this coupling and is particularly sensitive to beyond Standard Model (BSM) physics.

The cross section of the electroweak W + jets production is measured with an integrated luminosity of $20.3\,\mathrm{fb}^{-1}$ recorded with the ATLAS detector in 2012 in a phase space that enhances the VBF component of the process. In particular the VBF topology is used to separate a relatively small signal process from W boson production with jets produced by strong vertices. The production cross section for this background is approximately a factor 100 higher than for the pure electroweak production. In addition the electroweak W + jets production is used to set limits on deviations from the SM couplings by using the approach of anomalous couplings with and without a form factor to ensure tree-level unitarity. In addition to CP conserving parameters, also first limits on CP violating parameters from the effective lagrangian of the anomalous couplings approach are set. These limits are also converted into limits of an effective field theory (EFT) as an alternative approach to parameterise deviations from the SM in a model-independet way.

The thesis is structured as follows: In the next chapter the theoretical background is given, by introducing the SM as a relativistic quantum field theory as well as explaining details of the signal process and two approaches to parameterise the deviations from the SM of the three boson vertex. The following chapters introduce the LHC and the ATLAS experiment as well as the reconstruction and identification of the objects in the experiment, followed by an explanation of the simulation of physical processes by using Monte Carlo (MC) techniques. Chapter 7 introduces the kinematic cuts applied on the objects and events in order to suppress the background and enhance the signal. The only background that is not predicted by MC techniques is the multijet background, that consists mainly

of jets that are mis-identified as leptons. For this background a data-driven technique is developed that selects a template from collision data by loosening the lepton quality criteria. The strategy for the background estimate is discussed in chapter 8. In the following chapters, first the general sources of uncertainties, which are considered in the analysis, are explained (chapter 9), followed by the detailed discussion of the cross section measurement of the electroweak W + jets production in chapter 10. The limits on the three boson couplings are presented in chapter 11. Finally, chapter 12 summarises the thesis.

2 — Theoretical Background

The SM of particle physics is a theory which describes the known elementary particles and interactions. In this chapter the fundamental concept of the SM is introduced, starting with a summary of the particles and their interactions followed by a short introduction to Quantum Field Theory (QFT). The QFT provides the mathematical framework to formulate the SM, where the particles occur as excitations of fundamental fields. Furthermore the theories of the electromagnetic interactions (Quantum Electrodynamics (QED)), the Unification of the QED with the weak force, the so called electroweak theory and the strong force, known as Quantum Chromodynamics (QCD), are explained. In the last part of this chapter an overview of the description of Triple Gauge boson Coupling (TGC), and how to access deviations from the SM by searching for anomalous couplings is given. This is followed by an introduction to W-boson production at hadron colliders and the VBF production mode.
This chapter is mainly based on [1, 2] for the general SM description and on [3–6] for the TGC description.

2.1 Elementary Particles and Fundamental Interactions

All matter particles carry spin 1/2 and belong to the group of fermions. There are 12 of them in total, six quarks and six leptons. The fermions are grouped into three generations, whereof only the particles of the first generation (the electron and the electron-neutrino, ν_e, as well as the up and down quarks) build the matter around us. The particles from the second and third generations have the same physical properties but have higher masses. An overview of fermions from all generations is given in table 2.1. The different types of matter particles can be distinguished by the way they interact and hence the charges they carry. Quarks are the only particles which are colour-charged and therefore the only particles that are sensitive to the strong force. Together with the electric-charged leptons, they participate also in the electromagnetic interaction. The weak interaction is the only force where all particles are sensitive to, including neutrinos which carry neither colour-charge nor electromagnetic charge.
In the SM the fundamental forces are mediated by spin-1 particles, which are also called vector bosons. A full list of the bosons with their spatial range is listed in table 2.2. The photon is a massless boson that mediates the electromagnetic interaction and couples to particles that carry electric charge. The weak force is carried by three massive bosons, the charged W and the neutral Z bosons. Finally, the massless eight gluons mediate the strong force and bind the quarks to (colour-neutral) hadrons.
The three fundamental forces only describe the kinematics of the particles but not their masses. As shown in table 2.1 and 2.2 some of the particles have a (not-negligible) mass, that was experimentally found. With the Brout-Englert-Higgs (BEH) mechanism, based

Table 2.1: Overview of the fermions and some of their properties, like charge and mass, in the SM. The masses for the neutrinos are just upper bounds as the direct measurement of the mass in not possible todate. Uncertainties are only quoted when they are significant [7].

Leptons			Quarks		
Flavour	Mass [GeV]	Charge [e]	Flavour	Mass [GeV]	Charge [e]
electron e	$511 \cdot 10^{-6}$	-1	up u	$(2.3^{+0.7}_{-0.5}) \cdot 10^{-3}$	+2/3
e-neutrino ν_e	$< 3 \cdot 10^{-9}$	0	down d	$(4.8^{+0.7}_{-0.6}) \cdot 10^{-3}$	-1/3
muon μ	$106 \cdot 10^{-3}$	-1	charm c	1.28 ± 0.03	+2/3
μ-neutrino ν_μ	$< 0.19 \cdot 10^{-3}$	0	strange s	$(95 \pm 5) \cdot 10^{-3}$	-1/3
tau τ	1.78	-1	top t	$173.2 \pm 0.51 \pm 0.71$	+2/3
τ-neutrino ν_τ	$< 18.2 \cdot 10^{-3}$	0	bottom b	4.18 ± 0.03	-1/3

Table 2.2: Known interactions and the corresponding bosons with their mass and the spatial range [7].

Force	Boson	Mass [GeV]	Range [m]
Electromagnetism	Photon	0	∞
Weak Force	$W^\pm$	80.385 ± 0.015	10^{-18}
	Z^0	91.1876 ± 0.0021	
Strong Force	Gluons	0	10^{-15}

on the principle of electroweak symmetry breaking it is possible to generate the mass of the particles. Hereby a new massive boson is predicted, the so called Higgs boson, that was finally discovered in 2012 at the LHC [8, 9]. The BEH mechanism is explained in more details in section 2.5.

2.2 Introduction to Quantum Field Theory

The QFT combines the principles of special relativity and quantum mechanics. Its basic concepts were developed in the 1920's, first of all only to describe the interaction of photons and electrons in the QED. Later on it was possible to include the strong and the weak force, thus the QFT became the framework to describe the particles, which correspond to certain fields, and interactions among them. In the QFT it is possible to create and annihilate particles by converting energy in mass and vice versa. In the framework of QFT symmetries play an important role, where a symmetry is described by a set of transformations under which the equations of motion are invariant. The SM is build from the principle of gauge invariance, where each gauge symmetry gives rise to one of the fundamental forces.
The combination of the electromagnetic and the weak force is described by the $SU(2)_L \times U(1)_Y$ gauge group [10–12], while the strong force corresponds to the $SU(3)$ gauge group [13–15]. Both of the gauge symmetries are non-abelian which means that there is a direct self-coupling between the gauge bosons of the gauge group due to non-commuting elements.

2.3 Quantum Electrodynamics

The QED describes the interaction between photons and charged fermions as a quantum field theory. In the following, the general procedure to build the Lagrangian of the interaction, which is invariant under the transformation of a certain symmetry group (for QED the underlying gauge group is the $U(1)$), will be explained and taken as a basis for the electroweak theory and the QCD, which are constructed in the same way, but with different underlying symmetry groups.
The QFT makes use of a similar Lagrange formalism that is already known from classical field theories. Therefore a free spin-1/2 fermion $\psi(x)$ can be described by the Dirac Lagrangian:

$$\mathcal{L}_{\text{Dirac}} = \bar{\psi}(x)(i\gamma^\mu \partial_\mu - m)\psi(x) \tag{2.1}$$

where γ^μ are the gamma matrices and m is the mass. This Lagrangian is Lorentz invariant and also invariant under a global $U(1)$ gauge transformation, if the transformation is considered as $\psi(x) \to e^{i\alpha}\psi(x)$ with a phase α being an arbitrary real constant independent of the space-time point x.
A transformation is called local if the phase α depends on the space-time coordinates $\alpha \to \alpha(x)$. If a theory is invariant under a local transformation this would imply that the

physics of the theory remains the same at each space-time coordinate. This is obviously a stronger requirement than the global invariance. In equation 2.1 only the mass term $\bar{\psi}m\psi$ remains invariant under the local transformation, the part involving the derivative ∂_μ not. In order to make the entire Lagrangian invariant under the $U(1)$ local transformation another field $A_\mu(x)$ is introduced which transforms in the following way:

$$A_\mu(x) \to A_\mu(x) - \frac{1}{e}\partial_\mu\alpha(x) \tag{2.2}$$

where e is the coupling constant between the particle and the gauge field. In addition the covariant derivative is introduced

$$\partial_\mu \to D_\mu = \partial_\mu - ieA_\mu. \tag{2.3}$$

To describe the interaction between the fermions and the spin-1 field $A_\mu(x)$ an interaction term has to be added to the Lagrangian:

$$\mathcal{L}_{\text{int}} = eA_\mu(x)\bar{\psi}(x)\gamma^\mu\psi(x) \tag{2.4}$$

The resulting Lagrangian is invariant under local $U(1)$ transformation but the field A_μ cannot propagate and therefore another extension of the Lagrangian, given by the Proca-Lagrange equation is needed:

$$\mathcal{L}_{\text{Proca}} = -\frac{1}{4}F^{\mu\nu}F_{\mu\nu} + \frac{m^2}{2}A^\mu A_\mu \tag{2.5}$$

where $F_{\mu\nu} = \partial_\mu A_\nu - \partial_\nu A_\mu$ is the electromagnetic field strength tensor[1]. The first term of equation 2.5, describing the kinematics of the photon, is invariant under the local transformation. The second term, which would give the mass of the photon field, is not invariant under the local gauge transformation, so it turns out that the photon field has to be massless ($m = 0$) and therefore leads to massless photons.
Finally, the interaction of the fermion field ψ with the photon field A_ν is given by the following Lagrangian of the QED:

$$\mathcal{L}_{\text{QED}} = \bar{\psi}(x)(i\gamma^\mu D_\mu - m)\psi(x) - \frac{1}{4}F^{\mu\nu}F_{\mu\nu} \tag{2.6}$$

2.4 Electroweak Theory

The electroweak theory is the unified description of the QED and the weak force with the $SU(2)_L \times U(1)_Y$ as the underlying gauge group. Here, $U(1)_Y$ denotes the unitarity group of degree 1 and $SU(2)_L$ the special unitarity group of all unitary 2×2 matrices with determinant 1. There are four gauge fields connected to this symmetry. The photon field which corresponds to the $U(1)$ gauge symmetry as shown in section 2.3 and the fields of the charged W and the neutral Z boson which belong to the weak interaction described

[1]Here and everywhere else, if not explicitly noticed, the implicit summation technique is used.

by the $SU(2)_L$ gauge group.
Before the Lagrangian of the electroweak interaction is constructed in a similar way to the Lagrangian of the QED in section 2.3, it is important to mention that the weak interaction treats left and right-handed particles different. The handedness is defined as the sign of the projection of the spin vector onto the momentum vector. A negative sign leads to left handed particles and a positive sign to right handed. In the SM left-handed fermions are grouped in doublets, while right handed particles occur as singlets. The local $SU(2)$ symmetry group only acts on the left-handed doublets while the right-handed singlets are left unaltered [16]. Table 2.3 shows the singlets and doublets of the $SU(2)$ group.

Table 2.3: This table gives an overview of the left-handed doublets and the right-handed singlets of the $SU(2)$ symmetry group.

Generation	Leptons	Quarks
1	$\begin{pmatrix}\nu_e\\ e\end{pmatrix}_L, e_R$	$\begin{pmatrix}u\\ d\end{pmatrix}_L, u_R, d_R$
2	$\begin{pmatrix}\nu_\mu\\ \mu\end{pmatrix}_L, \mu_R$	$\begin{pmatrix}c\\ s\end{pmatrix}_L, c_R, s_R$
3	$\begin{pmatrix}\nu_\tau\\ \tau\end{pmatrix}_L, \tau_R$	$\begin{pmatrix}t\\ b\end{pmatrix}_L, t_R, b_R$

This leads to two different transformations for the electroweak interaction, one for the left-handed doublets which transform under the $SU(2)$ and $U(1)$ gauge group and one transformation for the right-handed singlets where only the $U(1)$ participates. Those two transformations are given in equation 2.7

$$\begin{aligned}\psi_L &= \frac{1}{2}(1-\gamma_5)\psi \rightarrow e^{i\alpha^j(x)\mathcal{T}_j + i\beta(x)\mathcal{Y}}\psi_L \\ \psi_R &= \frac{1}{2}(1+\gamma_5)\psi \rightarrow e^{i\beta(x)\mathcal{Y}}\psi_R,\end{aligned} \tag{2.7}$$

with the Pauli matrices $\mathcal{T}_j (j = 1, 2, 3)$ being the generators of the $SU(2)_L$ gauge group and $\mathcal{Y}$ the one generator of $U(1)_Y$. The fact that the $SU(2)$ symmetry group treads left and right handed particles differently violates the parity (P) symmetry and the charge (C) symmetry. The parity transformation changes left-handed systems into right-handed ones and therefore produces left-handed anti-neutrinos from right-handed anti-neutrinos. The $SU(2)$ symmetry group is also not invariant under the charge-conjugation transformation, where each particle is transferred into its anti-particle. This does not change the handedness of particles and left-handed neutrinos would become left-handed anti-neutrinos, which are again not allowed. It was further assumed that the $SU(2)$ symmetry group is invariant under the combination, CP, of the two transformations, as this would convert left-handed neutrinos into right-handed anti-neutrinos. In 1964 the CP violation of the electroweak theory was experimentally found in the decay of neutral kaons [17]. The C, P and CP

violation is observed only for the weak interaction and not for the strong and the electromagnetic interaction. To construct the $SU(2)_L \times U(1)_Y$ invariant Lagrangian four gauge vector fields are introduced similar to the section before. The $\mathcal{B}_\mu$ is associated with the $U(1)$ and $\mathcal{W}^i_\mu (i = 1, 2, 3)$ are associated with the $SU(2)_L$. Like in section 2.3 a covariant derivative is defined:

$$\partial_\mu \rightarrow D_\mu = \partial_\mu + ig\mathcal{T}_i\mathcal{W}^i_\mu + ig'\frac{\mathcal{Y}}{2}\mathcal{B}_\mu \tag{2.8}$$

g is the coupling constant between the fermions and the $SU(2)$ boson, while g' gives the strength of the coupling between fermions and the $U(1)$ boson. The resulting Lagrangian for the electroweak interaction is given by:

$$\begin{aligned}\mathcal{L}_{\mathrm{EW}} = &\sum_f [\bar{f}_L\gamma^\mu(i\partial_\mu - g\mathcal{T}_i\mathcal{W}^i_\mu - g'\frac{\mathcal{Y}}{2}\mathcal{B}_\mu)f_L + \bar{f}_R\gamma^\mu(i\partial_\mu - g'\frac{\mathcal{Y}}{2}\mathcal{B}_\mu)f_R] \\ &- \frac{1}{4}\mathcal{W}^i_{\mu\nu}\mathcal{W}^{\mu\nu}_i - \frac{1}{4}\mathcal{B}_{\mu\nu}\mathcal{B}^{\mu\nu}\end{aligned} \tag{2.9}$$

where $\mathcal{W}^i_{\mu\nu}$ and $\mathcal{B}_{\mu\nu}$ are the field strength tensors of the four gauge fields:

$$\mathcal{B}_{\mu\nu} = \partial_\mu\mathcal{B}_\nu - \partial_\nu\mathcal{B}_\mu \tag{2.10}$$

$$\mathcal{W}^i_{\mu\nu} = \partial_\mu\mathcal{W}^i_\nu - \partial_\nu\mathcal{W}^i_\mu - g\epsilon_{ijk}\mathcal{W}^j_\mu\mathcal{W}^k_\nu \tag{2.11}$$

The kinematics of the fermions and their interaction with the gauge fields are given by the terms inside the sum of the Lagrangian. The terms outside the sum describe the kinematics of the gauge fields as well as the self-interaction of the $\mathcal{W}^i_\mu$ fields. The fact that the field strength tensor $\mathcal{W}^i_{\mu\nu}$ of the $SU(2)$ in equation 2.11 contains bilinear terms leads to trilinear and quadrilinear self-couplings of the $\mathcal{W}^i_{\mu\nu}$ fields. At this point the fields cannot directly be connected to the physical fields of the four gauge bosons $W^\pm$, Z^0 and γ, as they are still massless and do not have the right charge. To explain the mass of the gauge bosons (and the fermions) the mechanism of spontaneous symmetry breaking is necessary, which will be explained in the next section.

2.5 Spontaneous Symmetry Breaking and the Brout-Englert-Higgs Mechanism

Just adding the mass terms for the gauge bosons (and the fermions), e.g. $M^2W_\mu W^\mu$, to the Lagrangian in equation 2.9 would break the gauge invariance. To keep the photon massless and to provide masses to the W and Z bosons, a mechanism is needed that does not break the $U(1)$ symmetry but the $SU(2)$ symmetry [18]. This can be achieved by the BEH mechanism [19–21] which introduces a new scalar field, Higgs field, in the following way:

$$\Phi = U(x)\begin{pmatrix}0\\ \rho(x)/\sqrt{2}\end{pmatrix} \equiv \begin{pmatrix}\phi^+\\ \phi^0\end{pmatrix} \tag{2.12}$$

with $\rho(x)$ being the density distribution of the new charge and $U(x) = e^{\frac{i\tau_j \Theta^j(x)}{2}}$ a general SU(2) gauge transformation. To describe the kinematics of the Higgs fields an additional term is added to the Lagrangian in 2.9, that is invariant under the $SU(2)_L \times U(1)_Y$ gauge symmetry and couples the new scalar fields to the gauge bosons through the covariant derivative D_μ:

$$\mathcal{L}_{\text{Higgs}} = (D_\mu \Phi)^\dagger (D^\mu \Phi) - V(\Phi) \tag{2.13}$$

The self-coupling of the Higgs field is described by the potential $V(\Phi)$ which is defined as

$$V(\Phi) = -\mu^2 \Phi^\dagger \Phi + \lambda (\Phi^\dagger \Phi)^2 \tag{2.14}$$

This is the Higgs potential, shown in figure 2.5 which is also known as "mexican hat" potential.

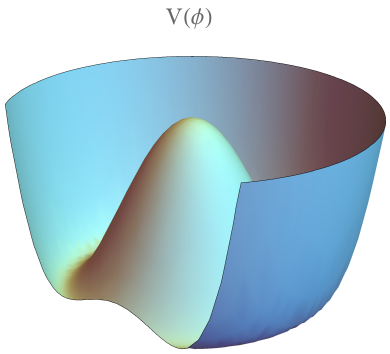

Figure 2.1: The potential $V(\Phi)$ of the Higgs field.

Under the assumption that μ^2 and λ are both positive, the minimum of the potential is found when

$$\Phi^\dagger \Phi = -\frac{\mu^2}{2\lambda}. \tag{2.15}$$

This minimum has the vacuum expectation value:

$$\langle \Phi \rangle = \langle 0|\Phi|0\rangle = \frac{1}{\sqrt{2}} \begin{pmatrix} 0 \\ v \end{pmatrix} \tag{2.16}$$

with

$$v = \sqrt{\frac{\mu^2}{\lambda}}$$

The mass terms of the vector bosons are given by the covariant derivative, which can be derived by a perturbative expansion of the potential around the minimum:

$$D_\mu \Phi = (\partial_\mu - ig\mathcal{W}_\mu^a \tau^a - \frac{i}{2} g' \mathcal{B}_\mu)\Phi \tag{2.17}$$

The masses that can now be calculated are still not the masses of the real gauge bosons but those can be derived from a linear combination in the following way:

$$\begin{pmatrix} W_\mu^+ \\ W_\mu^- \end{pmatrix} = \begin{pmatrix} 1/\sqrt{2} & -i/\sqrt{2} \\ 1/\sqrt{2} & i/\sqrt{2} \end{pmatrix} \begin{pmatrix} \mathcal{W}_\mu^1 \\ \mathcal{W}_\mu^2 \end{pmatrix} \tag{2.18}$$

$$\begin{pmatrix} Z_\mu^0 \\ A_\mu \end{pmatrix} = \begin{pmatrix} \cos\theta_W & -\sin\theta_W \\ \sin\theta_W & \cos\theta_W \end{pmatrix} \begin{pmatrix} \mathcal{W}_\mu^3 \\ \mathcal{B}_\mu \end{pmatrix} \tag{2.19}$$

The angle θ_W is the weak mixing angle, also called Weinberg angle, and is defined by:

$$\begin{aligned} \cos\theta_W &= \frac{g}{\sqrt{g^2 + g'^2}} \\ \sin\theta_W &= \frac{g'}{\sqrt{g^2 + g'^2}} \end{aligned} \tag{2.20}$$

By introducing the BEH mechanism and the spontaneous symmetry breaking a full description of the electroweak theory including the massive gauge boson of the weak interaction is in place. A_μ is still massless and describes the photon field, which couples to both left and right handed particles with the same strength. The neutral Z boson is given by the Z_μ^0 field also couples to both, left and right handed particles, but with different strength, while the charged W bosons only couples to the left-handed doublets.

Another feature brought by the $W_\mu^\pm$ fields is the fact that they can change the flavour in a particle decay. This is only possible because the weak eigenstates of the fermion doublets, listed in table 2.3, differ from the mass eigenstates, which leads to a mixing between the flavours and not only within a doublet. For the quarks the transition probability between the different quark flavours is given by the Cabibbo-Kobayashi-Maskawa matrix, V_{CKM}:

$$\begin{pmatrix} d' \\ s' \\ b' \end{pmatrix} = V_{CKM} \begin{pmatrix} d \\ s \\ b \end{pmatrix} = \begin{pmatrix} V_{ud} & V_{us} & V_{ub} \\ V_{cd} & V_{cs} & V_{cb} \\ V_{td} & V_{ts} & V_{tb} \end{pmatrix} \begin{pmatrix} d \\ s \\ b \end{pmatrix} \tag{2.21}$$

while V_{ud}, V_{cs} and V_{tb} are close to one the off-diagonal elements are small, which means that even if mixing is possible the transition within a weak doublet is still favoured [22, 23]. After describing the mechanism for the gauge boson masses in detail, there are still two missing pieces, which will not be explained in detail. The first is the presence of the new boson coming along with the Higgs field. The Higgs boson, which was predicted when the BEH mechanism was introduced in the 1960's and could experimentally found in 2012 with the data from the LHC experiment. Till then only the range for the Higgs mass

could be set by experimental searches and theoretical constraints. It was finally found to have a mass of $m_H = 125.7 \pm 0.4\,\text{GeV}$ [7]. The second missing piece is the mass of the fermions, which are derived also from the coupling to the Higgs field via the Yukawa couplings. It turns out that every fermion has its own coupling and thus the masses are not predictable and have to be measured experimentally.

2.6 Quantum Chromodynamics

At this point only a brief overview of the QCD will be given. It is constructed as a quantum field theory similar to the QED. The underlying gauge group is the $SU(3)$ with the colour as the conserved quantity of the QCD. Each quark can have three different colour states, red, green or blue, while the anti-quark carries the corresponding anti-colour. The QCD is mediated by massless bosons, the gluons, which themselves are colour-charged, carrying colour and anti-colour. This leads to self-interaction between the gluons and introduces triple and quadric gluon vertices. To construct the Lagrangian of the QCD one starts like in the QED with a new field and a kinematic term, which needs an additional index, a, for the colour charge:

$$\mathcal{L}_{\text{kin}} = -\frac{1}{4} F^a_{\mu\nu} F^{\mu\nu}_a \tag{2.22}$$

$F^a_{\mu\nu}$ is the field strength tensor, given by:

$$F^a_{\mu\nu} = \partial_\mu A^a_\nu - \partial_\nu A^a_\mu - g_s f^{abc} A^b_\mu A^c_\nu \tag{2.23}$$

where f^{abc} represents the structure constants of the $SU(3)$, g_s the coupling constant of the QCD and A^i_ν the gluon fields. With this information the Lagrangian of the QCD can be written as:

$$\mathcal{L}_{\text{QCD}} = -\frac{1}{4} F^a_{\mu\nu} F^{\mu\nu}_a + \bar{q}_i (i\gamma^\mu (D_\mu)_{ij} - m\delta_{ij}) q_j \tag{2.24}$$

with q_i being the quark fields with mass m.

Another difference between the QED and the QCD, which leads to a completely different behaviour, is the size of the coupling constant. The coupling of the QED is given by the fine-structure constant $\alpha \approx \frac{1}{137}$. Each electroweak vertex in a given process introduces a factor α and hence the coupling is < 1, the probability of a process decreases with increasing numbers of electroweak vertices. The situation is different for the QCD, where at low energies the coupling constant α_s is larger than one, which means processes with a large number of strong vertices get more important. Besides this, it was found that the strong coupling constant is actually not constant[2] and increases with the distance between the interacting particles. In the range of the size of a proton the coupling is small

[2]To be precise: The electroweak couplings constant is also not constant but the effect is much smaller.

and so is also the interaction of quarks inside the proton, where they behave like free particles. This phenomenon is called *asymptotic freedom*. Once the interaction particles get separated, the coupling constant increases and hence the potential energy between the particles gets larger. At some point the energy is large enough to produce a new quark-anti-quark pair. Furthermore, quarks never occur as free "coloured" particles, they always form colour-neutral hadrons, this phenomenon is called *confinement*. These bound states consist either of two quarks, carrying colour and corresponding anti-colour or of three quarks where the colours add up to "white", like in the proton. The former are named mesons, while the latter are called baryons.

2.7 Triple Gauge Boson Couplings

After a general overview of the SM in the last sections, a description of the coupling of three gauge bosons is given in the following subsection. The mathematical reason for the self-coupling of the bosons is the electroweak symmetry group being non-abelian and therefore has non-commuting elements. In the search for new physics this vertex is particularly interesting as it may show deviations from the SM before the scale of new physics can directly be observed. Therefore, two approaches to parametrise deviations from the SM of the three boson couplings, namely the effective Lagrangian and the Effective Field Theory (EFT), will be introduced in the following. The weak boson vertex in the SM can be described in the following way:

$$\begin{aligned}\mathcal{L}^{\mathrm{SM}}_{\mathrm{TGC}} = &- ig_{\gamma WW}\left[g_1^{\gamma}A_{\mu}(W^{-\mu\nu}W^{+}_{\nu} - W^{+\mu\nu}W^{-}_{\nu}) + \kappa_{\gamma}F^{\mu\nu}W^{-}_{\mu}W^{+}_{\nu}\right] \\ &- ig_{ZWW}\left[g_1^{Z}Z_{\mu}(W^{-\mu\nu}W^{+}_{\nu} - W^{+\mu\nu}W^{-}_{\nu}) + \kappa_{Z}Z^{\mu\nu}W^{-}_{\mu}W^{+}_{\nu}\right]\end{aligned} \tag{2.25}$$

with the electromagnetic field strength tensor $F^{\mu\nu}$. Equation 2.25 shows that there are only two TGCs allowed in the SM: γWW and ZWW. Vertices with an odd number of W bosons (WVV or WWW, with $V = Z\,\mathrm{or}\,\gamma$) are forbidden because they violate charge conservation, while neutral vertices VVV are not possible because the bosons carry neither electric charge nor electroweak hyper charge to couple to. Figure 2.2 shows two processes in which the triple boson vertex can occur in the SM.

On the left hand side the neutral boson V, which can be either a Z or a γ decays into the two opposite charged W bosons. The momentum transfer in this graph is time-like and differs from the one on the right hand side, where the momentum transfer is space-like. This is the so-called Vector Boson Fusion process where two bosons fuse and produce a third boson. This leads to only one boson in the final state and can therefore be well separated from the other process. In principle one can rotate the Feynman diagrams in figure 2.2 to produce other final state particles, like the single Z boson in the VBF graph or a WZ pair instead of two W bosons, but this does neither change the vertex nor the kinematics due to space-like and time-like momentum transfer. What can be also mentioned is that the coupling strength in the vertex depends on the momentum due to the derivative in each term of the Lagrangian [25].

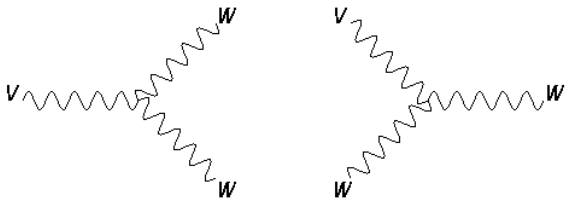

Figure 2.2: The left hand side Feynman diagram [24] shows the decay of a neutral boson into two charged bosons, whereas in the Feynman diagram on right hand side, two of the bosons fuse to the third one. One important difference when studying the triple gauge boson vertex is that the momentum transfer is time-like on the left hand side plot and space-like on the right hand side plot.

2.7.1 Beyond-SM Contributions

The SM is a powerful theory that describes the known particles and interactions very well and allows to make precise predictions. Nevertheless, there are aspects seen in nature, like dark matter and dark energy, that cannot be explained by the SM. With the knowledge that there has to be some physics beyond our theory, physicist are searching for those missing parts. A common idea is that the SM is only a low energy approximation of a more general concept at high energies. The fact that there are yet no direct observations of new physics, like new heavy particles, leads to the assumption that the energy scale of the new physics, Λ, is well beyond the energy that can be accessed with the current experiments. Besides the direct search for new heavy particles, another way to access new physics is to look for new or modified interactions of the known particles. Depending on the nature of the new physics this would potentially be measurable at current experiments. The most common way to look for those effects is a model-independent search for new phenomena with e.g. an effective theory. Far away from the scale of new physics the known interactions are replaced or extended by effective vertices, which can be used to test for deviations from the SM without detailed assumptions on the new phenomena. Ideally the effective approach gives a hint of the scale of new physics.

In the following the approach with an EFT will be described, which is the most general model-independent way to search for deviations in the three boson coupling. Furthermore the access to new physics via anomalous couplings/an effective Lagrangian[3] will be explained. This approach needs additional unitarisation requirements to not violate unitarity at tree level, which is a disadvantage compared to the EFT. These two approaches have been developed in parallel in the past, before the Higgs boson was found and the spontanous symmetry breaking nature of the electroweak theory was confirmed. Most of the previous analysis used the effective Lagrangian approach to test the charged three boson couplings and still most simulations only allow to vary the coupling in terms of

[3]Depending on the reference, the term *effective Lagrangian* is either used for the resulting Lagrangian of the EFT or denotes the Lagrangian of the approach via the anomalous couplings. In this thesis *effective Lagrangian* is used for the anomalous couplings approach unless otherwise stated.

the anomalous couplings approach. At the end of section 2.7.3 it will be explained how the results from the effective Lagrangian approach can (under certain circumstances) be converted into results from the EFT and vice versa.

2.7.2 Effective Field Theory Approach

A model-independent way to extend the SM is via an EFT. This respects the symmetries of the SM, namely the Lorentz invariance and the $SU(3)_C \times SU(2)_L \times U(1)_Y$ gauge symmetry. Up to now all operators in the Lagrangian of the of the SM are of dimension four or less. In the EFT the SM Lagrangian is extended with operators of higher dimensions. This includes one operator of dimension five that generates the Majorana masses of the neutrinos, and can therefore be neglected in this analysis. There are a couple of operators with mass dimension six, where only the few that contribute to the description of the three boson vertex are further considered. All parameters have coefficients that have inverse powers of mass and therefore operators of higher orders are suppressed when the scale of new physics is large compared to the energies in the experiment. To effectively describe the three boson vertex, the SM Lagrangian can be extended in the following way:

$$\mathcal{L}_{\text{EFT}} = \mathcal{L}_{\text{SM}} + \sum_n \sum_i \frac{c_i}{\Lambda^2} \mathcal{O}_i \tag{2.26}$$

where Λ denotes the scale of the new physics and $\mathcal{O}_i$ dimension-six operators describing the non-SM couplings of the three vector bosons. The coefficients c_i are dimensionless and parametrise the strength of the coupling between particles. For $\Lambda \to \infty$ the dimension-six operators would vanish and the EFT would recover the SM. This shows the limits of the EFT, as in energy regimes close to Λ higher-dimensional operators must not be neglected, as they are no longer suppressed. Therefore the effective approach is only valid at a certain scale far enough from the new physics. In terms of the WWZ couplings there are 3 CP conserving parameters left, denoted as $\mathcal{O}_{WWW}$, $\mathcal{O}_W$ and $\mathcal{O}_B$ as well as two parameters that violate C and/or P, namely $\mathcal{O}_{\tilde{W}WW}$ and $\mathcal{O}_{\tilde{W}}$. They are defined as:

$$\mathcal{O}_{WWW} = \text{Tr}[\mathcal{W}_{\mu\nu}\mathcal{W}^{\nu\rho}\mathcal{W}^{\mu}_{\rho}] \tag{2.27}$$

$$\mathcal{O}_W = (D_\mu \Phi)^\dagger \mathcal{W}^{\mu\nu}(D_\mu \Phi) \tag{2.28}$$

$$\mathcal{O}_B = (D_\mu \Phi)^\dagger \mathcal{B}^{\mu\nu}(D_\mu \Phi) \tag{2.29}$$

$$\mathcal{O}_{\tilde{W}WW} = \text{Tr}[\tilde{\mathcal{W}}_{\mu\nu}\mathcal{W}^{\nu\rho}\mathcal{W}^{\mu}_{\rho}] \tag{2.30}$$

$$\mathcal{O}_{\tilde{W}} = (D_\mu \Phi)^\dagger \tilde{\mathcal{W}}^{\mu\nu}(D_\mu \Phi) \tag{2.31}$$

with D_μ being the covariant derivative from equation 2.8 and $\mathcal{W}_{\mu\nu}$ and $\mathcal{B}_{\mu\nu}$ being the field strength tensors of the electroweak theory, which have already be defined in equation 2.11. The Higgs doublet field is denoted as Φ. A detailed discussion about the resulting dimension-six operators can be found in [5, 26].

2.7.3 Effective Lagrangian for Triple Gauge Boson Coupling

The deviations of the SM in the boson self-coupling can also be parameterised in terms of anomalous couplings. Therefore the Lagrangian in equation 2.25 is extended by additional operators. The most general Lorentz invariant WWV vertex is given by the following effective Lagrangian:

$$\begin{aligned}\mathcal{L}_{eff}^{WWV} =& ig_{WWV}\Big(g_1^V(W_{\mu\nu}^+W^{-\mu} - W^{+\mu}W_{\mu\nu}^-)V^\nu + \kappa_V W_\mu^+ W_\nu^- V^{\mu\nu} + \frac{\lambda_V}{M_W^2}W_\mu^{\nu+}W_\nu^{-\rho}V_\rho^\mu \\ &- ig_5^V\epsilon^{\mu\nu\rho\sigma}\big(W_\mu^+\partial_\rho W_\nu^- - \partial_\rho W_\mu^+ W_\nu^-\big)V_\sigma \\ &+ ig_4^V W_\mu^+W_\nu^-(\partial^\mu V^\nu + \partial^\nu V^\mu) + \tilde{\kappa}_V W_\mu^+W_\nu^-\tilde{V}^{\mu\nu} \\ &+ \frac{\tilde{\lambda}_V}{M_W^2}W_\mu^{\nu+}W_\nu^{-\rho}\tilde{V}_\rho^\mu\Big) \end{aligned} \tag{2.32}$$

with $g_{WWZ} = -e\cot\theta_W$, $g_{WW\gamma} = -e$ and $V = Z$ or γ and the dual tensor $\tilde{V}^{\mu\nu} = \epsilon^{\mu\nu\rho\sigma}V_{\rho\sigma}$. In this Lagrangian all operators of dimension eight and higher have been cut off. This is valid if the scale of new physics is far away from the energy that is accessible in the experiment. Electroweak gauge invariance requires $g_1^\gamma = 1$. Furthermore, comparing with equation 2.25, it turns out that in the SM $g_1^Z = \kappa_V = 1$ while all other parameters are zero.

The above given parameters can be divided into three groups according to their properties regarding C, P and CP conservation. The parameters in the first row g_1^V, κ_V and λ_V conserve CP as well as C and P separately, while g_5^V conserves CP but violates C and P. The parameters g_4^V,$\tilde{\lambda}_V$ and $\tilde{\kappa}_V$ given in the last two rows violate CP, while g_4^V violates also C, $\tilde{\lambda}_V$ and $\tilde{\kappa}_V$ conserve C but violate P [25]. In the following, only the terms g_1^V, κ_V, λ_V, $\tilde{\lambda}_V$ and $\tilde{\kappa}_V$ will be considered, because they can be directly converted into coefficients of the EFT. The two remaining operators of dimension six (according to λ_V and $\tilde{\lambda}_V$) are responsible for the Lagrangian not being renormalisable, such that close to the scale of new physics the effective approach breaks down and tree-level unitarity will be violated. The unitarity violation can be prevented by introducing (arbitrary) form factors that reduce the amplitudes at high energies, but of the costs that the whole approach is no longer completely model-independent. Each of the couplings is then modified in a way that the form factor is introduced and will reduce the amplitude at high energies:

$$\alpha(\hat{s}) = \frac{\alpha_0}{(1+\hat{s}/\Lambda_{FF}^2)^n} \tag{2.33}$$

where α_0 is the bare coupling and Λ_{FF} can be interpreted as the mass scale where the new physics can be observed directly, e.g. in terms of new particles, and n is chosen to ensure unitarity[4]. For charged vertices n is typically set to 2 (dipole form factor), while for neutral vertices $n = 3$ [6]. The choice of the optimal value of Λ_{FF} is fairly complex and depends on the kinematic of the processes. For the production of two bosons the dependence of Λ_{FF} from the expected limits on the TGC parameters is given in [3]. This

[4] Λ_{FF} is not equal to Λ from section 2.7.2, as the former is more or less arbitrarily chosen, while the later denotes the true scale of new physics

calculation can be adopted for the VBF process, although the kinematic is different [27]. The expected limits are estimated by calculations with $\Lambda_{FF} = 100\,\text{TeV}$, which means actually that no form factor is applied for a center-of-mass energy $\sqrt{s} = 8$ TeV. It turns out that $\Lambda_{FF} = 4\,\text{T}e\text{V}$ is the highest possible form factor that ensures unitarity conservation for all TGC parameters. Besides the fact that introducing form factors to ensure tree level unitarity makes the effective Lagrangian no longer model-independent, it does also not automatically respect the $SU(2)_L \times U(1)_Y$ gauge symmetry. This can be achieved by requiring certain relations between the parameters of the effective Lagrangian. Therefore the parameters are tested in the so-called *LEP scenario* [5], which effectively reduces the number of free parameters and ensures the gauge symmetry:

$$\Delta\kappa_\gamma = -\frac{\cos^2\theta_W}{\sin^2\theta_W}(\Delta\kappa_Z - \Delta g_1^Z), \tag{2.34}$$

$$\lambda_Z = \lambda_\gamma, \tag{2.35}$$

$$\Delta\tilde{\kappa}_\gamma = -\frac{\cos^2\theta_W}{\sin^2\theta_W}\Delta\tilde{\kappa}_Z, \tag{2.36}$$

$$\tilde{\lambda}_Z = \tilde{\lambda}_\gamma, \tag{2.37}$$

where $\Delta\kappa_{Z/\gamma} = \kappa_{Z/\gamma} - 1$, $\Delta g_1^Z = g_1^Z - 1$ and $\Delta\tilde{\kappa}_Z = \tilde{\kappa}_Z - 1$. The LEP scenario reduces the nine independent parameters to five parameters: g_1^Z, κ_Z, $\lambda_{Z/\gamma}$, $\tilde{\lambda}_{Z/\gamma}$ and $\tilde{\kappa}_Z$.
As mentioned in the previous section, there are certain circumstances where the parameters from the effective Lagrangian and the ones from the EFT can be converted into each other. In this case no form factor must be applied on the effective Lagrangian. Therefore, limits are set with the from factor $\Lambda_{FF} = 100$ TeV, which reflects, as described above, effectively the absence of a form factor. This is only valid, as it can be assumed that the scale of new physics is well beyond the accessible energy of the experiment. The resulting relation between the parameters of the two approaches are found to be:

$$\frac{c_W}{\Lambda^2} = \frac{2}{M_Z^2}(g_1^Z - 1), \tag{2.38}$$

$$\frac{c_B}{\Lambda^2} = \frac{2}{\tan^2(\Theta_W)M_Z^2}(g_1^Z - 1) - \frac{2}{\sin^2(\Theta_W)M_Z^2}(\kappa_Z - 1), \tag{2.39}$$

$$\frac{c_{WWW}}{\Lambda^2} = \frac{2}{3g^2M_W^2}\lambda_\gamma = \frac{2}{3g^2M_W^2}\lambda_Z, \tag{2.40}$$

$$\frac{c_{\tilde{W}}}{\Lambda^2} = -\frac{2}{\tan^2(\Theta_W)M_W^2}\tilde{\kappa}_Z, \tag{2.41}$$

$$\frac{c_{\tilde{W}WW}}{\Lambda^2} = \frac{2}{3g^2M_W^2}\tilde{\lambda}_\gamma = \frac{2}{3g^2M_W^2}\tilde{\lambda}_Z, \tag{2.42}$$

where c_W, c_B and c_{WWW} denote the three CP conserving parameters, whereas $c_{\tilde{W}}$ and $c_{\tilde{W}WW}$ are given as the CP violating parameters.

2.8 Basics of Proton-Proton Interactions

The probability of a certain process to occur in a proton-proton collision is given by its cross section σ. This cross section depends on the center-of-mass energy $\sqrt{s}$ and can be calculated in the SM. Protons are no fundamental particles, only the constituents of the proton interact and therefore the actual collision energy of the parton-parton interaction is unknown. The hadron with four-momentum P, which energy is equal to the beam energy, can be described by its constituents. Those partons carry only a fraction of the hadron momentum: $p_i = x_i P$, which has to be considered in the cross section calculation. The factorisation theorem [28] states that the cross section calculation can be split into the calculation of the partonic cross section $\sigma_{ab\to cd}$ and the probability density to find the partons a and b in a proton with their given momentum fraction x_a and x_b. The factorisation relies on the (arbitrary chosen) factorisation scale μ_F, which separates the two energy regimes of the short-distance and the long-distance physics. Finally the cross section for the final state, involving the partons c and d, from a collision of the protons A and B can be expressed as:

$$\sigma_{(AB\to cd)} = \sum_{a,b} \int f_a(x_a, \mu_F^2)\, f_b(x_b, \mu_F^2) \cdot \sigma_{ab\to cd}(\hat{s}, \mu_F^2) \mathrm{d}x_a \mathrm{d}x_b \tag{2.43}$$

where $\hat{s}$ denotes the square of the center-of-mass energy of the colliding partons and $f_i(x_i, \mu_F^2)$ the Parton Distribution Function (PDF) of the parton i, which describes the probability to find a parton of flavour i with the momentum fraction x_i. The PDFs of the proton can not be calculated perturbatively and are constrained with data from previous experiments. Figure 2.3 shows the probability to find a constituent of the proton with a given momentum fraction x for the CT10 PDF [29], with the factorisation scale set to the W boson mass, $\mu_F = 80\,\mathrm{GeV}$. Only the up and down quarks occur as valence quarks in the proton and thus at high momentum fractions it is more likely to find one of them, whereas at lower momentum gluons have the highest probability to appear.
In contrast to the PDF the partonic cross section can be calculated with perturbative QCD, as it involves a high-momentum transfer. For the cross section the Matrix Element (ME) of the process is needed, which is a sum of all possible Feynman diagrams that contribute to the process. This would include, besides the Leading Order (LO) diagrams at tree level, also diagrams in higher order of QCD, which include gluon radiation and internal loops. The number of Feynman diagrams increases significantly with the additional strong vertices and the calculation gets more complicated. Therefore, most processes are only considered at LO or Next-to-Leading Order (NLO), only very few processes include corrections up to Next-to-Next-to-Leading Order (NNLO). The ME is further integrated over the phase space to derive the partonic cross section. If the ME contains higher order corrections divergences in the integration can appear. Therefore the calculation has to be renormalised which ensures a finite expression for the ME. An (arbitrary) energy scale is introduced, at which the renormalisation is performed, that is called the renormalisation scale μ_R. The renormalisation and the factorisation scale are only needed because of the infinite length of the perturbative expansion and the influence of their chosen values has to be evaluated in the analysis.

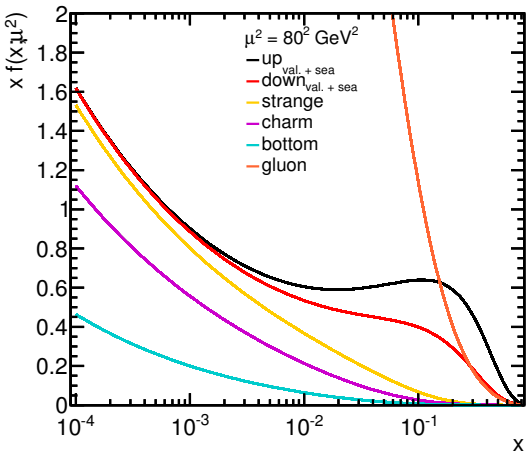

Figure 2.3: CT10 PDF [29] of the proton as a function of the parton momentum fraction x using the factorisation scale $\mu_F = 80\,\mathrm{GeV}$. The plot was compiled with data from ref. [30]

2.9 W-Boson Production and Decay at Hadron Colliders

The W boson was experimentally discovered in 1983 at the Super Proton anti-Proton Synchrotron (S$p\bar{p}$S), at CERN [31]. Its properties have been intensively studied at the Large Electron Positron Collider, LEP, also located at CERN and the TeVatron at Fermi National Accelerator Laboratory, Fermilab, close to Chicago. The mass is found to be $80.385 \pm 0.015\,\mathrm{GeV}$ with a decay width of $\Gamma = 2.085 \pm 0.042\,\mathrm{GeV}$ [7]. The dominant production mechanism of W bosons at hadron colliders is via quark-anti-quark annihilation [32] and the corresponding Feynman diagram is shown in figure 2.4(a).

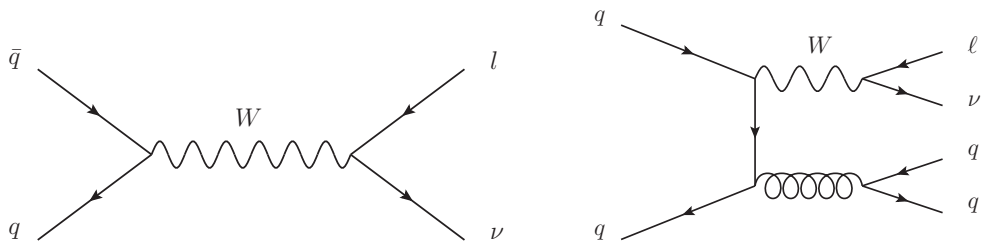

(a) Dominant W boson production at hadron colliders (b) W boson production at hadron colliders with additional partons in the final state

Figure 2.4: Feynman diagrams for W-boson production at hadron colliders via quark-anti-quark annihilation. The dominant production is without additional particles (left). More particles can be produced by additional strong vertices as shown on the right hand side plot.

This process has no additional particles in the final state at lowest order, but of course, additional partons can be radiated from the incoming quark lines via additional strong vertices, where each of those vertices reduces the probability for the process. An example of such a process is shown in figure 2.4(b).
A W bosons in association with two additional partons in the final state can also be produced via pure electroweak interaction. These processes have at least four electroweak vertices and are therefore less likely. An example of the contributing Feynman diagrams are given in figure 2.5.

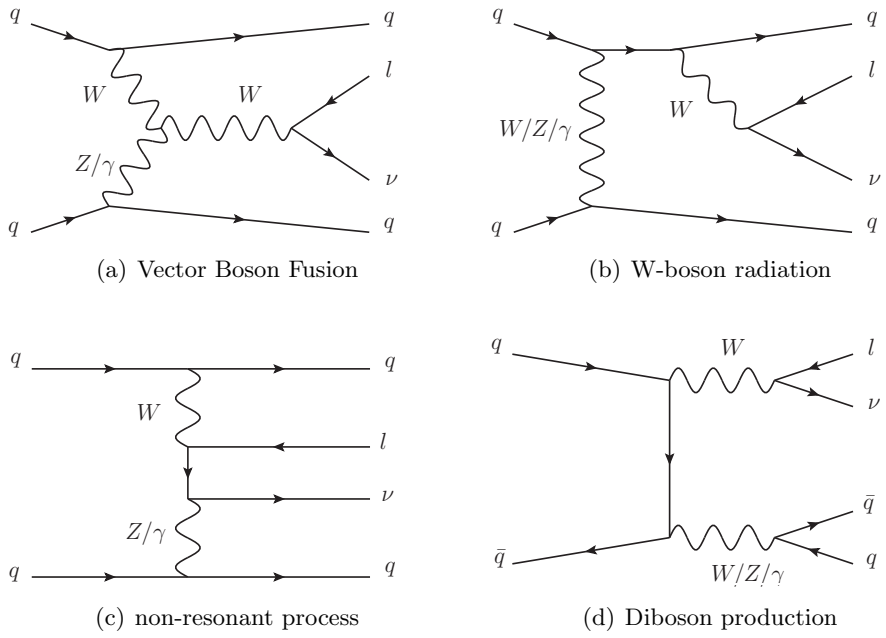

Figure 2.5: Subset of diagrams contributing to the EW W + jets production. The VBF diagram is shown in figure 2.5(a). The process where the W boson is radiated from a quark line is given in figure 2.5(b). Figure 2.5(c) shows a non-resonant production of the charged lepton and a neutrino that is also contained in the signal. Not in the signal is the diboson production which is depicted in figure 2.5(d).

The VBF process is shown in figure 2.5(a) where both of the two incoming quarks radiate a vector boson which then fuse to produce the W boson. This process has a characteristic event topology, as the two quarks are scattered with a small angle in the very forward region, while the decay products of the W boson are expected to be found central in the gap between the quarks. As there is no colour connection between the two incoming quarks no hadronic activity is expected in the gap. Due to the large angle between the outgoing partons, the invariant mass of the di-parton system is large. A colourless t-channel exchange between the incoming quarks can also be found in the process depicted in figure 2.5(b). In this case the W boson is radiated from one of the quarks. The process in figure 2.5(c) differs from the two other as this is a non-resonant production of the final

state particles, although this is also a t-channel process with no colour connection between the incoming quarks. These three graphs shown in figure 2.5(a)-2.5(c) are all t-channel processes which are further referred to as the EW signal.
Figure 2.5(d) shows a process with the same initial and final states like the other three and the same number of electroweak vertices but is a s-channel process with a colour connection between the incoming partons. This process is treated differently from the above ones and further referred to as diboson background[5].

The W boson has a finite lifetime and decays before it can be detected. Thus, only its decay products are measured. Regardless of the production mechanism, the W boson decays mainly into a quark-anti-quark pair ($\approx 68\%$) or a lepton and the corresponding neutrino. The probability for the decay into the different lepton flavour is equal and $\approx 11\%$ for each [7].

[5] In section 9.2.3 the concept of interference between two processes will be explained and under which circumstances it is allowed to treat them independently

3 — The LHC and the ATLAS Experiment

For more than 60 years scientists come together in Geneva in Switzerland at the European centre for nuclear research, Conseil Européen pour la Recherche Nucléaire (CERN) for particle physics research. The latest and most powerful accelerator located at CERN is the LHC, that is built in a tunnel with a circumference of 27 km, 100 m below the surface, to accelerate proton and lead beams and collide them at four main interaction points with a design centre-of-mass energy of $\sqrt{s} = 14\,\text{TeV}$ for proton beams and $\sqrt{s} = 2.8\,\text{TeV}$ per nucleon for lead beams. The collisions are detected by four experiments: There are two so called "multi-purpose" detectors ATLAS [33] and CMS [34], which cover the full range of physics of the SM and beyond, possible in proton-proton collisions. In addition Large Hadron Collider beauty (LHCb) [35] is designed to detect rare decays of heavy flavour hadrons and to precisely measure the parameters of CP violation. In contrast to ATLAS and CMS, LHCb is not constructed symmetric around the interaction point, since it makes use of the fact that pairs of b quarks are preferably produced in forward directions and thus is build only in one hemisphere, but still accomplishs $\approx 35\%$ acceptance for $b\bar{b}$ pairs. The fourth detector A Large Ion Collider Experiment (ALICE) [36] is adapted for heavy ion collision. It is optimised to handle the high particle multiplicities that occur in lead-lead collisions and to understand the quark-gluon plasma, an environment that is characterised by extreme energy densities and high temperatures where quarks and gluons are no longer confined [37].

3.1 Large Hadron Collider

Before injected into the actual LHC ring, protons have to run trough a full chain of pre-accelerators [38]. A schematic overview of the LHC accelerator complex is given in figure 3.1. Protons are extracted from hydrogen using an electric field and accelerated to an energy of 50 MeV in the linear accelerator (LINAC2). The protons are then injected into the Proton Synchrotron Booster (PSB) [40]. Once they reach an energy of 1.4 GeV they are handed over to the Proton Synchrotron (PS) [41], where they are accelerated up to 25 GeV before they are injected into the Super Proton Synchrotron (SPS) [42], which is the last step before entering the actual LHC ring with an energy of 450 GeV. The LHC can, in principle, accelerate protons up to an energy of 7 TeV per beam, but has been operated with 4 TeV beam energy in 2012. The LHC is a synchrotron accelerator where acceleration, bending and focussing of the beam is separated into different sections. There are eight superconducting cavities per beam for the acceleration, operating at 4.5 K and producing an accelerating field of 5 MV/ m at 400 MHz. The bending is performed by 1232 superconducting dipol magnets which are cooled down with superfluid helium to 1.9 K. These dipol magnets need to produce a field of 8.3 T for the design beam energy of 7 TeV to keep the beam on track. In addition there are 392 quadrupole magnets that

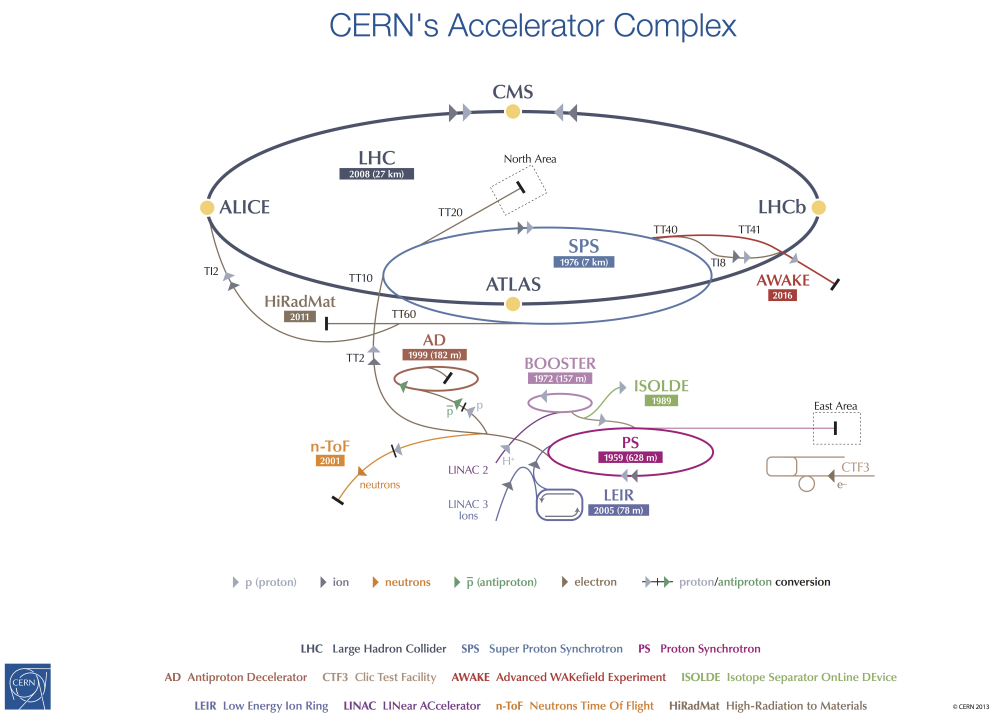

Figure 3.1: Schematic view of the CERN accelerator complex with various experiments [39].

focus the beam. Protons in the LHC are grouped into bunches, where each bunch consists of upto 115 billion particles. The LHC can store 2808 bunches in total, which leads to collisions every 25 ns. The rate of particle interactions per area is called the instantaneous luminosity $\mathcal{L}$ which is one of the most important parameters of a particle accelerator. It is defined as:

$$\mathcal{L} = \frac{N_\mathrm{b}^2 n_\mathrm{b} f_\mathrm{rev} \gamma_r}{4\pi \epsilon_n \beta^*} F \tag{3.1}$$

with N_b being the number of particles per bunch and n_b the number of bunches per beam, f_rev is the revolution frequency and γ_r is the relativistic gamma factor, ϵ_n is the normalised transverse emittance at the interaction point, β^* is the beta function at the interaction point and F is the geometrical reduction factor arising from the crossing angle. An overview of the design values and the values achieved by the LHC when operating in 2012 is given in table 3.1. To get the total amount of delivered data one integrates over

Table 3.1: Overview of the LHC performance parameters [43].

Parameter	Design value	Value in 2012
Beam energy	7 TeV	4 TeV
β^* in int. points 1, 2, 3, 4	0.55 m	0.6 m, 3.0 m, 0.6 m, 3.0 m
Bunch spacing	25 ns	50 ns
Bunches per beam	2808	1374
Particles per bunch	$1.15 \cdot 10^{11}$ p/bunch	$1.6 - 1.7 \cdot 10^{11}$ p/bunch
ϵ^* at start of fill	3.75 mm mrad	2.5 mm mrad
Peak luminosity	$10^{34}\,\mathrm{cm}^{-2}\,\mathrm{s}^{-1}$	$7.33 \cdot 10^{33}\,\mathrm{cm}^{-2}\,\mathrm{s}^{-1}$
Max. mean number of events per crossing	~ 19	~ 40
Stored beam energy	~ 362 MJ	~ 140 MJ

the instantaneous luminosity and gets the so-called integrated or cumulative luminosity $\mathcal{L}_\mathrm{int} = \int \mathcal{L} dt$.

3.2 The ATLAS Experiment

The ATLAS experiment is the largest detector at the LHC, being 44 m long with a diameter of 25 m and a weight of more than 7000 t[1]. A schematic overview is given in figure 3.2. The ATLAS experiment is arranged cylindrical around the interaction point with different types of detectors built in layers. The innermost part is the Inner

[1]The description and numbers in the following section are taken from [33] if not otherwise stated.

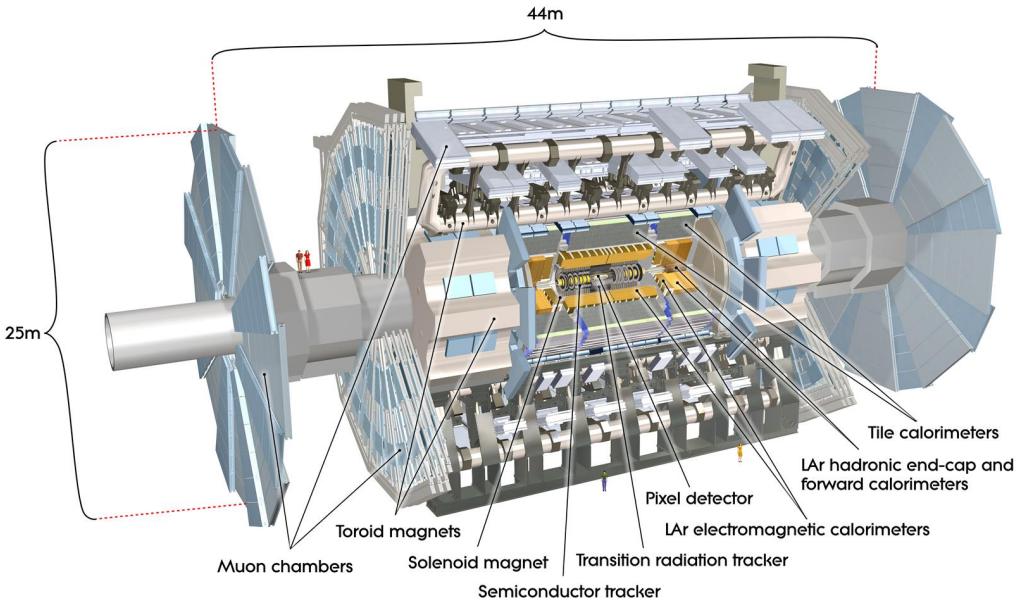

Figure 3.2: Schematic view of the ATLAS detector [44].

Detector (ID), a tracking system with three different sub-detectors, the Pixel Detector, the Semiconductor Tracker (SCT) and the Transition Radiation Tracker (TRT), where the tracks of charged particles can be measured. Since the whole ID is embedded in the field of a solenoid magnet it is possible to measure the momentum of the charged particles that leave a track in the ID. The energy of most particles can be measured in the calorimeters that are located around the ID. Photons and Electrons are stopped in the electromagnetic calorimeter, which is the inner part of the calorimeter system, while hadrons pass through it and deposit their energy in the hadronic calorimeter. There are two kind of particles that escape those inner parts of the detector without getting stopped: muons and neutrinos. While it is impossible to detect neutrinos at all, a Muon Spectrometer (MS) is build around the calorimeter system to measure the muons that escape the calorimeter system, where a toroidal magnet field allows to measure the momentum of the muons. The ATLAS experiment uses a right-handed coordinate system, with the origin adjusted to the nominal interaction point and the z-axis along the beam direction.The x-y-plane is perpendicular to the beam, where the x-axis points to the center of the LHC ring and the y-axis upwards to the surface. In addition the azimuthal angle ϕ and the polar angle θ are defined, where ϕ is measured in the x-y-plane clockwise by starting at the x-axis and θ is measured with respect to the positive z-axis. Instead of θ, particle trajectories are often described by the rapidity:

$$y = \frac{1}{2} \ln \left(\frac{E + p_z}{E - p_z} \right) \tag{3.2}$$

or the pseudorapidity

$$\eta = -\ln\tan(\frac{\theta}{2}) \tag{3.3}$$

where the latter is an approximation of the rapidity for massless particles. One advantage when using the rapidity instead of the angle θ is that the distance of two particles given in rapidity is Lorentz invariant. The angular distance of two objects is defined as:

$$\Delta R = \sqrt{\Delta\eta^2 + \Delta\phi^2} \tag{3.4}$$

As the colliding energy along the z-axis is not well defined in hadron collisions, as the energy fraction of the constituents of the hadron is unknown.Therefore it is very common to measure the momentum only in the x-y-axis as this was zero before the collision and indicates if high energetic processes have been occurred. This transverse momentum is defined as:

$$p_{\mathrm{T}} = \sqrt{p_x^2 + p_y^2} \tag{3.5}$$

Assuming momentum conservation the vector sum of the p_{T} of all reconstructed objects in the event should add up to zero. This sum is called missing transverse momentum ($\not{E}_T$) and gives access to undetected particles, like neutrinos, and mis-measurements of p_{T}. It is defined as

$$\not{E}_T = -\sum_{\text{rec. obj.}} \vec{p}_{\mathrm{T}} \tag{3.6}$$

3.2.1 Inner Detector

As already mentioned, the ID is the innermost part of the ATLAS detector system and consists of three independent subdetectors which can be seen in the schematic overview in figure 3.3.

The aim is to measure the trajectory of charged particles with high spatial, angular and momentum resolution. To deflect the charged particles, and therefore allow to measure the momentum, the whole ID is embedded in a 2T solenoid magnetic field. The ID is 6.2 m long with a diameter of 2.1 m and covers a pseudorapidity range up to $|\eta| < 2.5$. The ID contains the following components:

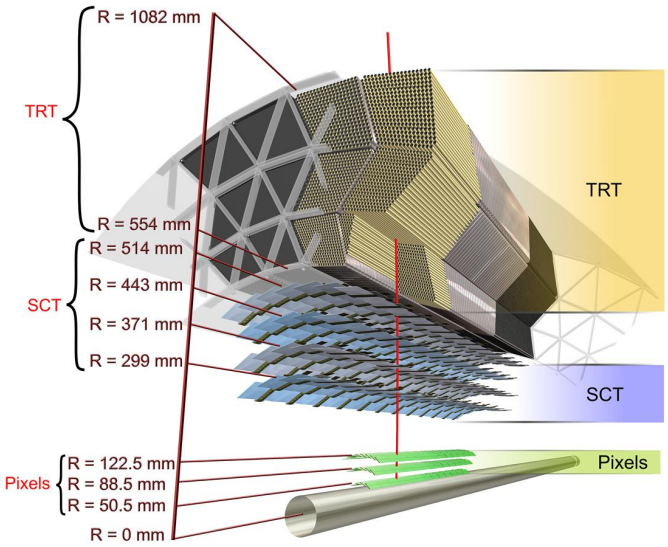

Figure 3.3: Schematic view of the Inner Detector including Pixel detector and the Silicon Strip Detector as well as the Transistion Radiation Tracker [45].

- Closest to the beam is the pixel detector located with more than 80 million sensors in total, arranged in concentric cylinders of three layers of pixel staves in the barrel, each with 1456 modules and three discs on each side in the end caps with 288 modules, so that a particle typically leaves three space points to construct a track. The pixel size of $50 \times 400\,\mu$m provides a resolution of $14\,\mu$m in the $R-\phi$ plane and $115\,\mu$m in the z-direction and therefore ensures the very high granularity needed to reconstruct particle tracks and to identify primary vertices in high occupancy environments.

- The second silicon detector is the SCT which is built around the pixel detector. It uses silicon microstrips instead of pixels, placed on 4088 modules. In the barrel region the SCT is arranged cylindrical on four two-sided layers and nine discs in the end-caps. The more than 6 million strips are placed every $80\,\mu$m in the silicon which leads to a spatial resolution of $17\,\mu$m in the $R-\phi$ plane and $580\,\mu$m in the beam direction.

- The TRT is the third subdetector and the outermost part of the ID and covers a pseudorapidity range $|\eta| < 2.0$. In contrast to the silicon detectors, this part is built of straw tubes with a diameter of 4 mm, which are filled with a Xenon-based gas mixture that is ionised by charged particles passing trough the detector. In each straw tube is a gold-plated tungsten wire with a diameter of 0.03 mm that collects the resulting electrons. The barrel consists of more than 50000 straw tubes each 144 cm long, which are arranged parallel to the beam pipe, while the straw tubes in

the end caps are arranged radially in wheels and are only 36 cm long. The whole TRT contains more than 350000 readout channels with a resolution in the $R - \phi$ of 130 μm where particles leave 36 space time points on average. The fact that different particles produce a different amount of transition radiation in the straw tubes makes is possible to distinguish the different kind of particles, like electrons and pions, in the TRT.

3.2.2 Calorimeter

The ID is surrounded by the ATLAS calorimeter system with an inner diameter of 2.8 m. It is composed of different types of sampling calorimeters, which can measure the energy of most particles. A schematic overview of the calorimeter system can be found in figure 3.4. Electrons and photons are detected in the electromagnetic (EM) calorimeters that is the

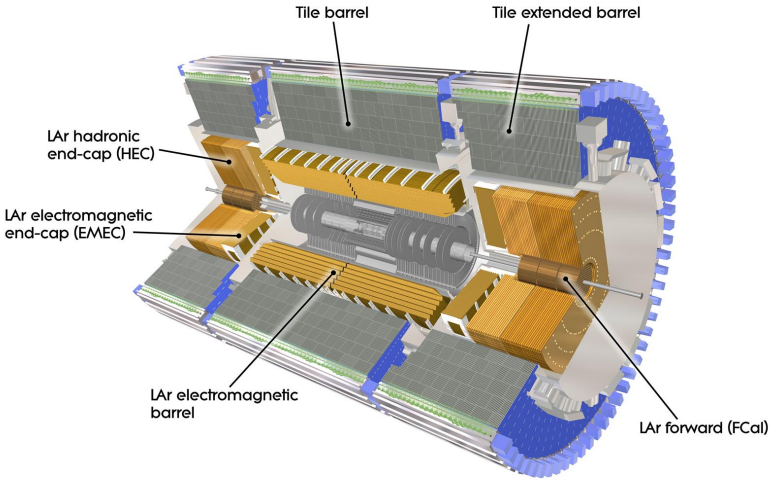

Figure 3.4: Schematic view of the electromagnetic (inner part) and the hadronic (outer part) calorimeter of the ATLAS detector [46].

innermost part of the calorimeter system. In the barrel region ($|\eta| < 1.5$) and in the end-caps ($1.5 < |\eta| < 3.2$) it uses lead as absorber and Liquid Argon (LAr) as active material. The main advantage of LAr is its intrinsic linear behaviour and its radiation hardness, and therefore it was chosen for the EM and the forward calorimeter (FCal) although this means the detector has to be cooled down to 88 K. In the barrel region the EM calorimeter is divided into three layers, where the first one is finely segmented in η to provide precision measurements of the particle position, from which especially the measurement of photons benefits since they do not leave a track in the ID. The second layer collects the largest fraction of the EM shower energy, while the third layer measures mostly the tail of the shower and therefore does not need a very fine segmentation. In all three layers the electrodes have a characteristic accordion shape ensuring a perfectly

symmetric coverage in ϕ. The whole EM calorimeter has a total thickness of at least 22 radiation lengths[2] in the barrel and 24 in the forward region. The resolution of the energy response of a calorimeter can be parameterised by three different terms that have a different dependence on the energy as shown in equation 3.7:

$$\frac{\sigma}{E} = \frac{a}{\sqrt{E}} \oplus \frac{b}{E} \oplus c \tag{3.7}$$

The first term a is called sampling or stochastic term and describes the uncertainty due to the numbers of particles in the shower. The particle multiplicity is directly proportional to the energy and therefore the relative uncertainty is a function of $1/\sqrt{E}$. The second term b describes the uncertainty due to detector and electronic noise and is independent of the deposited energy, thus the relative uncertainty is b/E. The constant term c limits the resolution due to inhomogeneities of the detector and non-uniformities in the signal response. The energy resolution of the EM calorimeter has been measured in electron test beams [47] to (after subtracting the noise term): $\frac{\sigma}{E} = \frac{10\%}{\sqrt{E}} \oplus 0.7\%$
The calorimeter measuring the hadronic interaction is placed around the EM calorimeter and consists of a LAr-based end-cap calorimeter and a central tile calorimeter. The latter one uses steel as an absorber and scintillating tiles as active material. In the barrel region $|\eta| < 1.0$ as well as in the extended barrel region, $0.8 < |\eta| < 1.7$ the calorimeter is built from three layers. Those have a thickness given in hadronic interaction lengths[3] of 1.5, 4.1 and 1.8 for the barrel and 1.5, 2.6 and 3 for the extended barrel, respectively and a energy resolution of $\frac{\sigma}{E} = \frac{52\%}{\sqrt{E}} \oplus 3\%$
Slightly overlapping with the tile is the hadronic end-cap calorimeter (HEC) in the range $1.5 < |\eta| < 3.2$. Like the EM calorimeter it uses LAr as the active material but copper for the absorber. There are two wheels on each detector side, both divided into two layers. The energy resolution is found to be $\frac{\sigma}{E} = \frac{84\%}{\sqrt{E}}$
The last part of the calorimeter system is the FCal which again uses LAr as active material. It is divided into three layers in depth, where the first is optimised to measure electromagnetic interaction and uses tungsten as the absorbing material. The last two layers mainly measure hadronic interactions and are built with copper as absorber material. It provides an energy resolution of $\frac{\sigma}{E} = \frac{29\%}{\sqrt{E}} \oplus 3.5\%$ for the first layer and $\frac{\sigma}{E} = \frac{94\%}{\sqrt{E}} \oplus 7.5\%$ for the second and third layers, respectively.

3.2.3 Muon System

Muons are the only charged particles that interact little enough to not get stopped in the calorimeter. Therefore, an additional tracking system is built around the calorimeters to identify muons with the capability of triggering events that contain high energetic muons. Since it surrounds the other parts of the detector the distance between the muon system

[2] A radiation length is a characteristic amount of material in which an initial electron reduces its energy to 1/e.
[3] The hadronic interaction length is a characteristic amount of material a particle traversed through before one hadronic interaction with the material happens.

and the interaction point is at least 5 m. A schematic view of the different types of muon chambers is given in figure 3.5. Within the pseudorapidity range of $|\eta| < 2.7$ two different

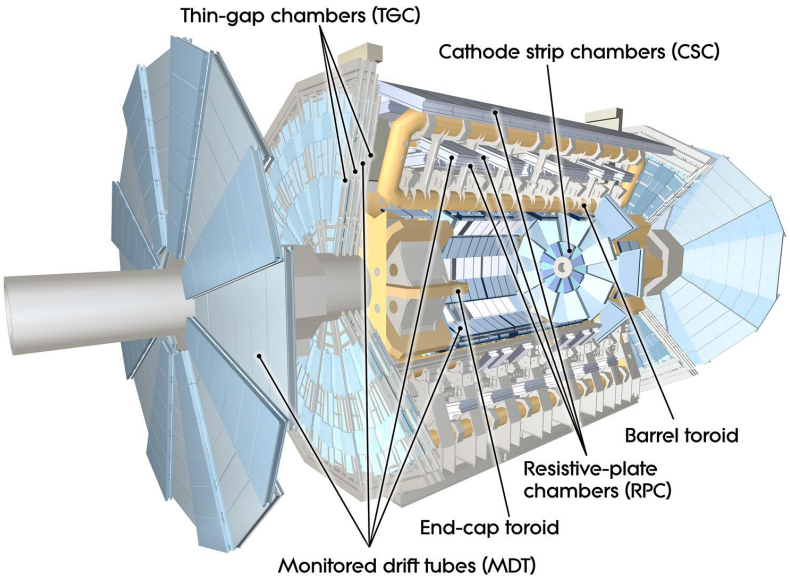

Figure 3.5: Schematic view of the muon chambers [48].

types of tracking chambers are installed. In the barrel three layers of Monitored Drift Tubes (MDTs), filled with an Argon-gas mixture, provide a spatial resolution of 80 μm and 35 μm in the beam direction. The end caps are built up from four wheels, where three of them are also MDTs. Although MDTs have the better resolution, the innermost wheel is a Cathode Strip Chamber (CSC) which provides a higher rate capability and time resolution. This is needed especially in the region $|\eta| > 2.0$ where many tracks are expected. The resolution of the CSC is 40 μm in the bending plane and 5 mm in the transverse plane. In the region $|\eta| < 2.4$ additional trigger chambers are installed which allow a faster readout. Those are Resistive Plate Chambers (RPCs) in the barrel and TGCs in the end caps. To allow for momentum measurement of the muons, the whole muon system is embedded in a toroidal magnetic field, which is produced by eight superconducting coils in the barrel ($|\eta| < 1.4$) and two smaller toroids in the end caps ($1.6 < |\eta| < 1.4$). This leads to a magnetic field that is perpendicular to the muon momentum direction of 0.5 T in the barrel and 1.0 T in the end caps.

3.2.4 Forward Detectors

In addition to the components described above, there are other detectors installed around the ATLAS experiment which mainly measure the luminosity and monitor the beam parameters.

Closest to the main detector, but still ± 17 m away from the interaction point Luminosity

measurement using Cerenkov Integrating Detector (LUCID) [49] is located. Based on the Cherenkov light that particles emit when passing through the twenty gas-filled tubes, the LUCID detector measures the instantaneous and integrated luminosity. When taking into account the LHC machine parameters the obtained precision is $20 - 30\%$.

The Large Hadron Collider forward (LHCF) detector [50] is installed $\pm 140\,\mathrm{m}$ away from the interaction point and is designed to estimate the energy of cosmic rays by measuring particles that are produced very close to the beam direction in proton-proton collisions.

To measure the absolute luminosity the Absolute Luminosity for ATLAS (ALFA) detector is installed [51]. It makes use of the elastic scattering at small angles and thus it has to be placed far away from the interaction point and as close as possible to the beam pipe. To reach an accuracy of 5% Roman pot technology has been installed 1.5 mm around the beam pipe in a distance of $\pm 240\,\mathrm{m}$ from the interaction point.

3.2.5 Trigger System

In 2012 the LHC provided proton-proton collision every 50 ns resulting in 20 MHz crossing frequency. Each event has a size of about 1.3 MBytes, which leads to a total amount of 26 TBytes of data delivered by LHC every second. Since storing of such large amount of data is obviously impossible using the current technologies the output rate has to be reduced significantly. Therefore, a three-levelled trigger system has been installed to ATLAS decreasing the data rate to manageable 200 Hz and storing only the interesting rare events. Given the high collision rate the decision between interesting and uninteresting events has to be made quickly.
The first decision is made within $\approx 2\,\mathrm{ms}$ by the hardware based Level 1 (L1) Trigger relying only on limited information from the muon chambers and the calorimeter. This first step reduces the output rate to 75 kHz and defines the Region of Interest (RoI). RoIs are regions in the $R - \phi$ plane that contain high energy particle candidates.
The RoIs are used as inputs for the software based High Level Triggers (HLT). The first one is the Level 2 (L2) trigger having access to the full event information for the RoIs, seeded by the L1. This is still only about 2% of the whole event information and it allows the L2 to make its decision within $\approx 40\,\mathrm{ms}$ and to further reduce the event rate to $< 3\,\mathrm{kHz}$.
The final step of the trigger chain is the Event Filter (EF) which uses the full event information and performs a more complex selection similar to the algorithms used for reconstruction. This procedure takes a few seconds and results in the final event rate of 200 Hz.

3.2.6 Performance of the ATLAS Experiment in 2012

In 2012 the LHC was performing proton-proton collisions at 201 days with a stable beam fraction of 36.5% and managed to provide $\mathcal{L}_{\mathrm{int}} = 22.8\,\mathrm{fb}^{-1}$ to the two large experiments

ATLAS and CMS. Figure 3.6 shows the total integrated luminosity for the year 2012 delivered by the LHC (green) and recorded by ATLAS (yellow) as well as the amount of data labelled as "good for physics" (blue).

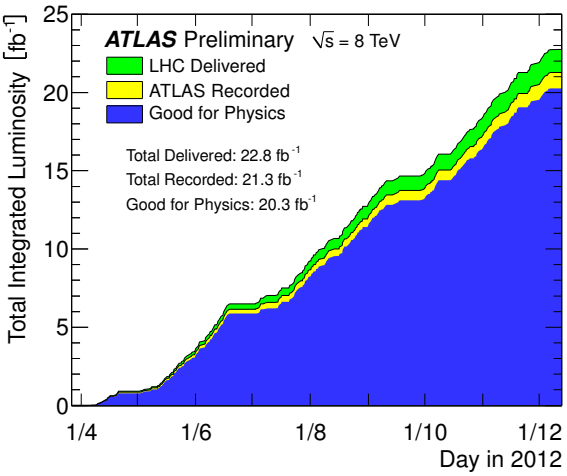

Figure 3.6: Cummulative distribution of the data delivered by the LHC (green), recorded by ATLAS (yellow) and labelled as *good for physics* (blue) in 2012 [52].

Due to inefficiencies in the data acquisition and ramping of the tracking detectors at the beginning of stable beams, ATLAS cannot trace the full amount of the collisions. Nevertheless, the overall data efficiency was 93% in 2012. The data is evaluated by quality requirements for each detector part and each reconstructed object and only if all detector parts are working well the data can be used for physics analysis. The events are labelled as *good for physics*, which was true for 95.8% of the recorded data. In addition the data is grouped into periods, where it is ensured that the beam and detector conditions are uniform. An overview of the data periods used for this thesis and the corresponding integrated Luminosity is given in table 3.2.

As it can be seen in figure 3.7 during the data taking in 2012 more than 20 proton-proton interactions on average took place in a single bunch crossing. This is a direct consequence of increasing the particles per bunch for higher instantaneous luminosity with the 50 ns bunch spacing. In general this leads to higher occupancy in the (tracking) detectors and requires tight track quality requirements to suppress fake objects in the reconstruction.

Table 3.2: Summary of the different data taking periods in 2012 with the corresponding integrated Luminosity [53].

Data period	$\mathcal{L}$ [fb^{-1}]
A	794.02
B	5094.68
C	1406.02
D	3288.39
E	2526.28
G	1274.81
H	1444.93
I	1016.26
J	2596.34
L	839.77

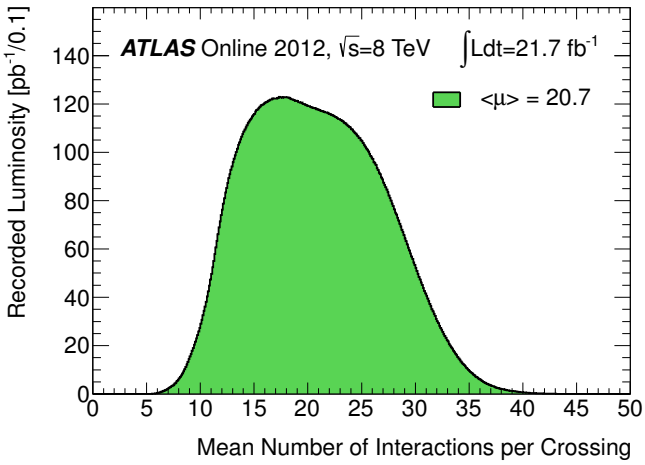

Figure 3.7: Mean number of interactions per bunch crossing for the 2012 proton-proton collisions dataset [52].

4 — Object Identification

After the description of the experiment and the data taking procedure in the last chapter, it will now be explained how the raw detector response is transferred into objects to be used in physics analysis. Several different reconstruction algorithms are implemented that turn ID signals into tracks, identify vertices and combine them with the calorimeter and/or the MS response to reconstruct electrons, muons and form so-called jets, which are clustered particles from the strong interaction.

4.1 Track and Vertex Reconstruction

The ATLAS track reconstruction is based on the measurements of all parts of the ID. The initial approach is a so-called *inside-out* strategy [54] which starts in the silicon detectors and extends it to the TRT. This approach is fragmented into three parts: *Global track seeding*, *ambiguity solving* and the TRT *track extension*.
In the first step three-dimensional space points are built from the hits in the silicon detectors. Initial track seeds are defined, based on at least three of the space points and with a minimal associated transverse momentum of 500 M*e*V. These track candidates are fed into a Kalman-fitter algorithm [55, 56] to fit the trajectory and extend the seed with additional hits close by the candidate. The seed is kept if the resulting track contains at least seven hits in the silicon detectors.
The resulting collection of track candidates contains fake tracks and tracks that overlay and share hits with other tracks. In the second step of the *inside-out* algorithm, the *ambiguity solving*, a ranking of the remaining tracks, is performed according to certain quality requirements. For example tracks with more hits are preferred as they are more likely to come from real particles. In this successive procedure the hits are also weighted, such that hits measured in the more precise detector parts, like the pixel detector, are getting higher weights while hits from the less precise parts are downgraded.
In the last step of the *inside-out* algorithm the track candidates, that are up to now only based on hits from the silicon detectors, are extended with hits from the TRT. Therefore, the fitted track seed is extended to the TRT and the hits that are close-by in the TRT (within a drift radius of 10 mm) are added to the existing track.
Although the *inside-out* algorithm is very efficient to find tracks from a primary vertex, there are a number of tracks that can hardly be found by this approach. Tracks that come from secondary decay vertices or photon conversions leave no or only very little hits in the silicon detectors. Also the *ambiguity solving* may downgrade some track seeds due to ambiguous hits which are further rejected. Therefore, an *outside-in* algorithm performs the last step of the track finding, which searches for track segments directly in the TRT, excluding the hits that have already been assigned to tracks with the *inside-out* algorithm. Those TRT segments are extrapolated back into the silicon detectors to find track seeds

that got lost in the *inside-out* algorithm and can be associated to the TRT track candidate.

After the identification of the tracks, they are clustered together to identify event vertices. Because many events happen in parallel at the LHC not all measured tracks originate from the same vertex and a good reconstruction of the different vertices is needed. This is done in two steps: The first step is the *vertex finding*, where the reconstructed tracks are associated to vertex candidates and in the second step the position of the vertex is determined with a fitting procedure. This step is referred to as the *vertex fitting* [57].
The ATLAS reconstruction chain uses the so-called *findig-through-fitting* approach as a default. This starts with a preselection of the reconstructed tracks which are measured in the beam spot[1]. After the preselection of the tracks, a single vertex candidate is defined and fitted with the vertex fitter. Those tracks, that are defined as outliers in the first fit, form a second vertex. In a second iteration the two vertices are fitted simultaneously. Thus the number of vertices grows with each iteration of the fitting procedure, while in each iteration the criteria for assigning a track to a vertex are tightened and the vertices are competing with each other to attain more tracks [57].

4.2 Electron Reconstruction and Identification

The reconstruction of electrons is based on the combination of various detector responses. An electron typically deposits its whole energy in the EM calorimeter. For a distinction of electrons and photons it is aimed to find a track in the ID that can be associated to the calorimeter measurement. This restricts the electron to be in the acceptance of the ID in a region $|\eta| < 2.5$.

The electron candidates have to pass further selection criteria to be used in physics analysis. There are three sets of criteria defined which are referred to as *loose*, *medium* and *tight* working points [58]. As the names indicate the criteria get stronger from *loose* to *tight* and therefore the efficiency decreases while the background rejection increases. Thus each analysis has to make a compromise and choose the best working point for their usage. With the medium trigger discussed above one has to choose at least the *medium* working point, otherwise the trigger requirement would be more stringent than the offline selection and can introduce a bias.
The *loose* selection starts with cuts on the shower shape in the first two layers of the EM calorimeter and the total lateral shower width. It further cuts on the energy leakage into the hadronic calorimeter. There is a total number of Silicon hits as well as a certain number of Pixel hits required for the track as well as a loose matching between the calorimeter cluster and the associated track.

The *medium* selection includes the *loose* cuts and requires explicitly a hit in the innermost layer of the Pixel detector (b-layer). Furthermore, cuts on the transverse impact parameter and on the total number of TRT hits are applied.

[1]The beam spot is the region where the collision takes place, described by a Gaussian profile with a standard deviation of 5 cm in the beam direction and 15 μm in the transverse plane

The *tight* selection includes the *medium* selection and provides the best background rejection by tighter cuts on the matching between the calorimeter cluster and the track. In addition the energy that is measured in the EM calorimeter has to match the momentum measured in the ID. At this stage all electron candidates are rejected if they can be associated to a reconstructed photon, to exclude electrons from photon conversions.
The signal selection of this analysis requires *tight* electrons, while the data-driven background estimate of the multijet background (section 8) uses *medium* electrons to enhance the background fraction.

4.3 Muon Reconstruction and Identification

Muons are not stopped in the calorimeter and thus can be identified by additional tracks in the MS, which is placed right outside the calorimeter. A reconstructed track from the MS is matched with the track from the ID that has the closest distance, and together they are forming a Combined (CB) muon candidate [59]. An additional algorithm starts with reconstructed tracks in the ID and searches for unused tracks in the MS. These two algorithms are referred to as *outside-in* and *inside-out*, respectively.
The tracks have to have at least one pixel hit and five SCT hits. At maximum two hits are allowed to be missing in the ID where they are expected. In addition, if the track transverses through the full TRT ($|\eta| < 1.9$) a minimum of 9 hits is required.

4.4 Jet Reconstruction

Particles that participate in the strong interaction cannot be observed as free particles. In fact they build bound states with other partons, which leads to bundles of particles in the hadronisation, that are referred to as jets. These jets are no fixed objects, as they rather rely on the clustering algorithm that is used for the reconstruction. The standard jet algorithm that is used by the ATLAS experiment, is the anti-k_{T} algorithm [60], which starts from topological clusters in the calorimeter. The basis for merging two objects i and j together is the distance between them, defined as:

$$d_{ij} = \min\left(\frac{1}{p_{\mathrm{T},i}^2}, \frac{1}{p_{\mathrm{T},j}^2}\right)\left(\frac{\Delta R_{ij}}{R}\right)^2$$

where ΔR_{ij} is the distance of the two objects in the $\eta - \phi$ plane, as defined in equation 3.4, while R is the radius parameter, which is chosen as $R = 0.4$ for the jet collection used in this analysis. Furthermore, $p_{\mathrm{T},i}$ and $p_{\mathrm{T},j}$ are the transverse momenta of objects i and j. In addition, the distance between an object i and the beam B is calculated, given as:

$$d_{iB} = p_{\mathrm{T},i}^{-2}$$

The cluster algorithm compares for a given object i if the distance d_{ij} to an object j is smaller than its distance to the beam line d_{iB}. If so, the two objects are clustered together and the algorithm is restarted, now with the new object, build from i and j. If not, so $d_{ij} > d_{iB}$ for all j, the object i is considered as a jet and removed from further clustering. Since the algorithm searches for the minimum of the inverted p_{T}^2 of the objects i and j, the clustering starts with the high-p_{T} objects and iteratively adds objects with smaller p_{T}.
A quality requirement of a cluster algorithm is the infrared and UV safety: Neither the number nor the shape of the jets should change by extra emission of soft gluons or collinear parton splitting. Therefore it is a big advantage of the anti-k_{T} algorithm that the two resulting collinear partons from a splitting process are immediately re-clustered to the same jet and at the end of the clustering the soft gluons from the emission are accumulated to the jet. Finally, if possible the clustered energy deposits in the calorimeter are matched to the tracks of charged particles that got reconstructed in the ID [61]. Due to the different acceptance of the ID and the calorimeter this works only for centrally produced jets.

4.5 Missing transverse Momentum

Some particles cannot be reconstructed, either because they are outside the detector acceptance or because they interact hardly with material and therefore leave no signal in the detector. Many of those particles are proposed in physics beyond the SM and thus are not important for this analysis. The one particle in the SM that can not be detected is the neutrino that occurs in every leptonical W-boson decay and therefore is an inherent part of the signal signature. The appearance of a neutrino in an event can in principle be proved by calculating the momentum balance of all initial and final state particles. Unfortunately in hadron collision the initial momentum along the beam direction of the incoming partons is unknown. Nevertheless it can be assumed that the initial partons have only momentum in z direction and no momentum in the transverse plane. Final state particles obviously have transverse momentum, otherwise they would not be detected as they would follow the beam direction. As already mentioned in equation 3.6 the transverse momenta of all final state particles are added up and the resulting transverse momentum that is not measured is referred to as $\not{E}_T$. For the reconstruction of $\not{E}_T$ the tracking information of most particles is used, only for jets the energy deposit in the calorimeter is also taken into account.

5 — Monte Carlo Event Generation

In collider experiments all different types of possible physics processes occur during the collisions and it is impossible to know what process happened in a specific event. Even if one wants to measure a certain process, referred to as *signal*, the selected data will always contain events from other processes, with either the exact same final state or a similar final state, that got mis-measured in the detector and thus looks like the signal process. Those processes are further referred to as *background*. It is crucial for a measurement to be aware of the background processes and to understand their details and the details of the signal process. Therefore a huge amount of events from the signal and all possible backgrounds are produced with MC generators, where all particles and their kinematics are generated. Those events cannot be compared to the data from the experiment directly, they have to run through a detector simulation first, where the interaction of the final state particles with the ATLAS detector is simulated. This detector response is handed over to the same reconstruction and identification algorithms as the real data including a simulation of the trigger chain. At this point the simulated events and the collision data can be compared. In the following chapter a general introduction to event generation with MC techniques is given, followed by an explanation of the MC generators used in this analysis. In addition the definition of *particle level* that is further used in the analysis to determine correction factors is given.

5.1 Principles of Monte Carlo Event Generation

The generation of single events makes use of splitting the collision process into separated phases, which can be simulated independent from each other. Figure 5.1 shows the whole collision processes with the individual phases. The inner most part is the *hard process*, where the interaction of the incoming partons is calculated on the basis of the parton-level ME. The underlying principles of the hard process have already been discussed in section 2.8. For many processes the event generation is available only at LO, but for more and more processes also the NLO becomes available, significantly improving the prediction. Once the particles with their momentum are generated by perturbative calculation of the hard process, non-perturbative higher order corrections are added by the Parton Shower (PS). Additional gluons are radiated from the initial and final state colour-charged particles, this is called QCD initial state radiation (ISR) or final state radiation (FSR). These gluons are further split into quark and anti-quark pairs, which leads to a cascade of soft gluons and quarks, being mainly collinear with the partons from the hard process. The corrections derived from the PS go down to low energy scales, at which perturbation theory is no longer applicable. After the showering the colour-charged particles have to be grouped to colour-neutral hadrons, in the so-called *hadronisation*, as they cannot occur as free coloured particles. Also the hadronisation cannot be calculated

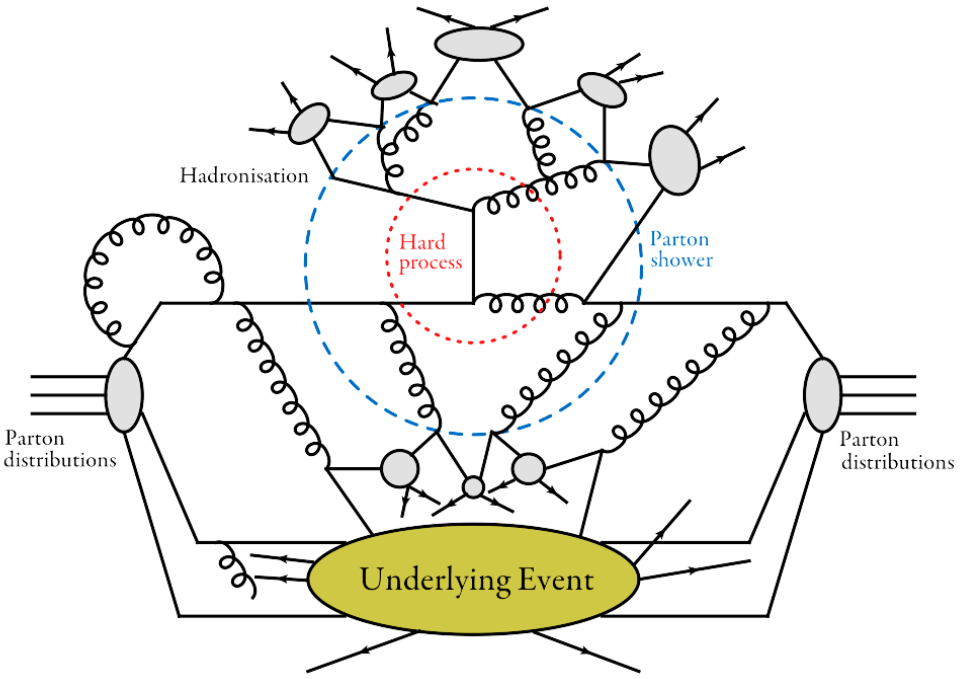

Figure 5.1: General structure of a proton-proton collision. The different processes are indicated: The hard process inside the red dotted line, the showering phase inside the blue dashed line and the underlying event in yellow. The hadronisation takes place just outside the blue dashed line which indicates the showering

with perturbation theory and is modelled by phenomenological approaches, constrained by data from previous measurements. Charged particles undergo also the QED FSR, where soft photons are radiated similar to the gluons from the QCD FSR. Further the decay of the unstable particles[1] is simulated, such that after the hadronization only stable particles remain. In addition to the calculation of the hard process the Underlying Event (UE) is generated: The remnants of the interacting hadrons are colour connected and thus additional particles appear in the event which do not originate from the hard process. Also other protons from the beam can interact with each other and produce more particles.

5.2 Monte Carlo Generators

The diversity of physical processes led to the development of many different MC generators, where most of them are specialised for certain processes including predictions at higher orders. Many of the generators only calculate the hard process and therefore, to be used in physics analysis, they have to work in connection with other tools, performing the PS and the hadronisation. Therefore, it is important to avoid double counting of the real emission from the NLO ME and the radiation from the PS due to an overlap in the phase space. There are different matching schemes available to perform the combination of ME calculation, the most common ones are: the CKKW [62] and the MLM matching [63]. As already mentioned the PS is a non-perturbative correction and is based on phenomenological models. Therefore the different shower generators give different predictions.

VBFNLO VBFNLO [64–66] is a ME generator that is specialised for the production of Higgs and vector bosons via VBF, as well as the production of double and triple boson final states. In addition various processes based on physics beyond the SM are implemented. All processes are available at LO and NLO accuracy in QCD.

Powheg/ Powheg Box The POWHEG (Positive Weight Hardest Emission Generator (POWHEG)) generator [67–69] is able to calculate heavy-quark-pair production ($c\bar{c}$, $b\bar{b}$ and $t\bar{t}$) at NLO accuracy. The whole top-quark decay is accessible including full spin correlations. In addition, with POWHEG Box it provides a tool to match external ME calculations at NLO, like for instance VBFNLO, to PS generators. In principle, this works for p_{T}-ordered as well as for angular-ordered shower algorithms, though the former is preferred due to simplicity.

Sherpa Simulation of High-Energy Reactions of PArticles (SHERPA) [70] is a multi-purpose event generator that provides ME calculations for lepton-lepton, hadron-hadron, lepton-hadron and photon interactions with up to ten partons in the final state. It covers a broad range of physics including many BSM processes, like varying the couplings of a triple gauge boson vertex. It comes along with an built-in PS and hadronisation model.

[1] Stable particles are in general defined as particles with a lifetime $> 30\,\mathrm{ps}$.

AcerMC The AcerMC event generation [71] is optimised for LHC conditions and thus provides very efficient generation. A limited amount of SM processes are implemented based on the ME calculation from MadGraph [72] at LO. The generation needs to be interfaced with external shower algorithms.

Pythia Pythia simulates MEs, hadronisation and the parton shower at LO, including initial and final state radiation using p_{T}-ordered showers. It also provides particle decays and the UE and can be used to interface ME calculations. This analysis makes use of the Fortran based version Pythia 6 [73] and the re-written C++ based version Pythia 8 [74].

Herwig Herwig [75] provides LO ME generation and shower generation, that includes hadronisation and particle decays. The main difference to Pythia is the angular-ordered shower generation. Although it includes its own UE simulation, based on high energy $p\bar{p}$ collisions from the UA5 collaboration, it can be interfaced to Jimmy [76, 77], to make use of a UE generation based on the multiple scattering model.

MC@NLO MC@NLO [78] is a ME generator that is optimised for QCD processes and provides NLO accuracy. For the evolution of the showering MC@NLO is usually interfaced with Herwig.

Photos Photos [79] is used to simulate the QED radiative corrections in particle decays and can be interfaced with all established ME generators. For many processes also NLO QED corrections are available.

Detector Simulations with Geant4 After the generation of the hard process and the PS, the interaction of the final state particles with the detector has to be simulated. Therefore, the ATLAS geometry was implemented in the Geant4 [80] package, where the path of the particles through the material of the detector is calculated and converted into digital "detector" responses. This output runs through the same reconstruction and identification algorithms as the collision data, so that afterwards the simulation can be compared to those.

5.3 Monte Carlo Truth Selection

For certain measurements it is necessary to evaluate the effect of object reconstruction and the detector acceptance. The basis for these corrections, that will be explained later in more detail, is a well defined *truth level*. This refers to a stage before the particles interact with the detector, but right after the PS and the hadronisation. The MC generators typically provide the full chain of the generation, including intermediate states

of PS, hadronisation and the decay of unstable particles and thus the objects have to be carefully chosen.

Leptons The charged leptons need to be labelled as stable, which means they have passed the QED radiation phase and no further corrections are applied before the interaction with the detector material is simulated. For all stable leptons the mother particles are checked and only those are considered that do not originate from hadrons. In the next step, the leptons are *dressed*, where the four-vector of all photons (that are also not allowed to originate from hadrons) in a cone $\Delta R < 0.1$ are added to the lepton four-vector.

Transverse Missing Momentum Since at the reconstruction level the $\not{E}_T$ occurs from neutrinos and the mis-measurement of the other reconstructed objets, it is at truth level only built from neutrinos. Therefore the four-vectors of all neutrinos are added up that do not originate from hadrons.

Jets The simulated event has already undergone the PS, and therefore it is possible to run a jet-cluster algorithm on the final state particles, where the particles that are not stopped in the calorimeter are excluded from the clustering, namely muons and neutrinos. The jet-cluster algorithm is the same anti-k_{T} algorithm as explained in section 4.4 with $R = 0.4$.

The same kinematic cuts as on reconstruction level (as will be explained section 7) can be applied on the above defined objects.

6 — Signal Signature and Background Processes

In this chapter the experimental signature of the EW $W + 2$ jets production, referred to as the signal process, and the various background processes will be described. In general it can be distinguished between reducible and irreducible backgrounds, where the latter have the exact same final state as the signal and can only be separated due to process kinematics, while the former have in principle a different final state but due to limited detector acceptance or mis-resonstruction and mis-identification they mimic the signal signature.

6.1 Signal Signature

The principles of the electroweak $W + 2$ jets production have already been discussed in section 2.9. In this analysis only the leptonic decay of the W boson is considered and therefore a charged lepton and a neutrino are expected in the final state. The analysis treats the electron and muon final state separately and combines the results from both channels in the end. Since τ leptons are decaying within the detector, they are not considered as a separate final state, but leptonically decaying τ leptons are added to the corresponding channel. The neutrino from the W boson decay cannot be measured and is only noticed as $\not{E}_T$. The two partons in the final state hadronise and are reconstructed as jets. This leads to a rather simple signal signature with a charged lepton and two jets in the final state with additional $\not{E}_T$. The main advantage is the large rapidity gap between the two high energy forward jets.
The signal process is generated with Powheg, based on a ME calculation from VBFNLO at NLO. The underlying PDF is CT10 and the showering is done with Pythia 8, that uses the AU2 tune [81] for the generation of the UE. The renormalisation and the factorisation scale are set to the W boson mass.
As a comparison, similar samples are generated with Sherpa 1.4.3, that make use of a special *min_t_channel* option. Usually the input for the event generation in Sherpa is the definition of the initial and the final state particles, as well as the number of strong and electroweak vertices. In the integration, all Feynman diagrams that fulfil these requirements are calculated. As mentioned in section 2.9 a definition like this would include also diboson processes. A new option was implemented in Sherpa 1.4.3 to explicitly require a t-channel exchange, which automatically excludes the diboson processes. Since the Sherpa calculation is performed at LO these samples are only used as a cross check. Furthermore, Sherpa allows to vary the coupling at the three boson vertex, $WWZ/WW\gamma$. Additional samples are generated using Sherpa 1.4.5 where the couplings are varied. Those samples are described in detail in section 11.1.

6.2 QCD W+ Jets Production

The largest background to the signal process is the W + jets production, where the jets are produced from QCD processes (referred to as *QCD W + jets*). The leading order W boson production has no additional jets in the final state (see Figure 2.4(a)), thus the production of a W boson with jets needs additional strong vertices, where each vertex reduces the probability of the process to occur. Figure 6.1 shows an example of the production of a W boson with two additional partons, split into the different initial and final states.

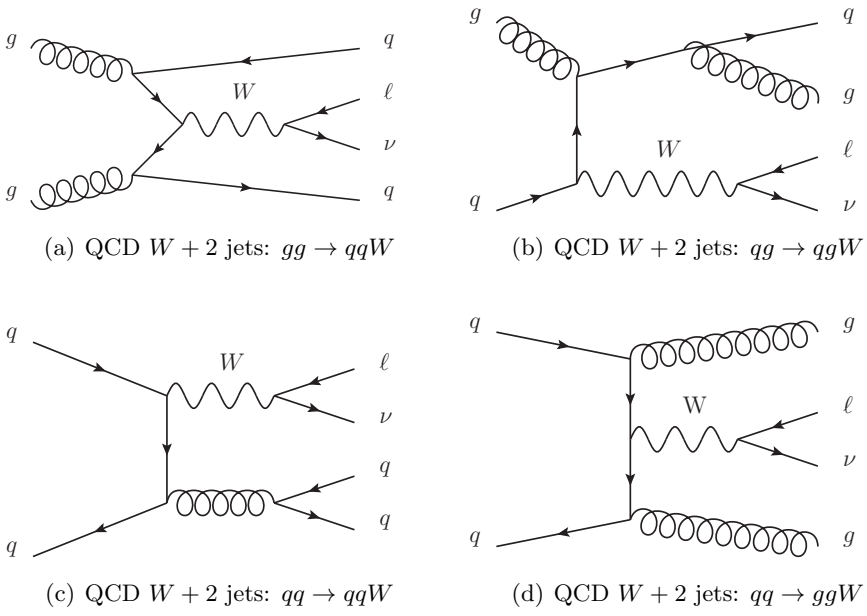

(a) QCD $W + 2$ jets: $gg \to qqW$

(b) QCD $W + 2$ jets: $qg \to qgW$

(c) QCD $W + 2$ jets: $qq \to qqW$

(d) QCD $W + 2$ jets: $qq \to ggW$

Figure 6.1: Different production modes for the QCD W + jets process.

Figure 6.1(a) shows the production of the QCD W + jets process originating from two gluons in the initial state. Each gluon from the initial state splits into a quark-anti-quark pair where two of the quarks produce the W boson while the other two hadronise and can be reconstructed as jets. The process with one quark and a gluon in the initial state is shown in figure 6.1(b). The gluon splits into a quark-anti-quark pair, where one of them fuses directly with a quark from the other proton to produce the W boson. The other quark hadronises and produces a second jet through gluon radiation. This Feynman diagram gives only an example as the additional gluon radiation can also happen from the initial state partons. Finally, figure 6.1(c) and figure 6.1(d) show a simple variation of initial state radiation from quark-anti-quark fusion. Where on the one hand the radiated gluon splits into a quark-anti-quark pair and produces two quark jets and on the other hand two gluons are radiated from the incoming partons and lead to two gluon jets.
In contrast to the signal the QCD W + jets production has only two electroweak vertices (production and decay of the W boson) and two strong vertices, which increases the

probability of the process to occur a lot. Depending on the phase space the absolute production rate is 100-1000 times higher than the signal, but as discussed above, the jets in the QCD W + jets process all come from higher order corrections. Therefore they have preferably low momentum and are often collinear, whereas the jets in the signal process come from the hard scattering and have to balance the heavy W boson in the event. The jet kinematics are the only, but very efficient way, to suppress the background.
The QCD W + jets background is generated with POWHEG at NLO [82] using the CT10 PDF and is interfaced with PYTHIA 8 for the showering using the AU2 tune. As already mentioned, most of the additional jets would be soft or collinear and thus would be removed at an early stage of a signal selection. However, a good modelling of this important background in a signal-like phase space is essential for the analysis and therefore the generation makes use of the *born suppression* [83], a method to suppress the cross section outside a relevant phase space. This allows to enhance the statistics of the background in the signal phase space, but for the cost of dealing with weighted events, rather than unweighted ones. Another advantage of the generation with POWHEG is the use of the multi-scale improved NLO (MINLO) generation [84], that improves the modelling of the W + jets production and reduces the uncertainty due to scale variations.
Additional samples for the W + jets process have also been generated with SHERPA for cross checks, using also the CT10 PDF but only at LO. These samples contain also MEs with less and more partons, as they are not optimised for this analysis. The cross section for the W + jets process (per lepton flavour) at NNLO in QCD is 12087±604 (theor.) pb [85].

6.3 Backgrounds with Top Quarks

Another source of important backgrounds is the production of top quarks, that are either produced as a pair of quark and anti-quark or as a single top quark in an electroweak production. Regardless of the production mechanism, top quarks decay with a probability of $\approx 100\%$ into a W boson and a b quark. Thus, depending on the decay of the W boson, the final state consists either of a charged lepton and $\not{E}_T$, or two light jets and in both cases an additional jet from the b hadron decay.

Top-Quark-Pair Production The dominant production mechanisms of top-quark pairs are shown in figure 6.2(a) and 6.2(b). Events with the momentum transfer needed for the production of a top quark pair are most likely produced by initial gluons. Figure 6.2(c) shows the production of a top-quark pair by a light quark-anti-quark-pair annihilation in the initial state with a s-channel momentum transfer by a gluon. The final state of the top-quark pair is categorised according to the decay of the two W bosons. Both can either decay leptonically or hadronically or one leptonically and the other hadronically (the latter is referred to as the semi-leptonic decay). The first combination has the cleanest signature but the lowest production rate, while the second has the highest production rate, but with six jets in the final state it is difficult to measure. The largest contribution for the background in this analysis has the third combination, which produces a charged lepton and the $\not{E}_T$ and four jets. This background gets especially important if the signal

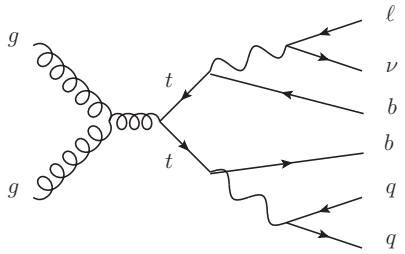

(a) Top-quark pair production via gluon fusion with a s-channel momentum transfer.

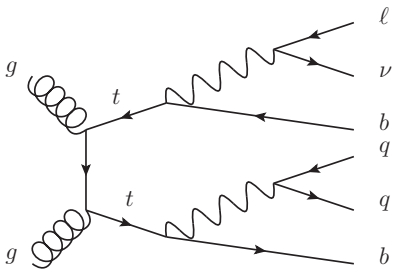

(b) Top-quark pair production via gluon fusion with a t-channel momentum transfer.

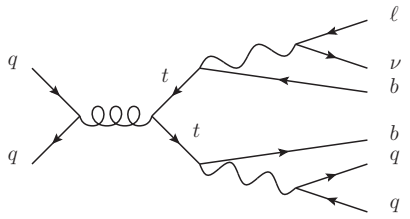

(c) Top-quark pair production via light quark fusion.

Figure 6.2: Different production processes of the top-quark-pair production at hadron colliders. Each Feynman diagram includs the semi-leptonical decay of the top-quark pair that has the highest contribution to top-quark-pair background in this analysis.

selection does not require exactly two but just a minimum of two jets in the final state, since more jets are always possible also in the signal process due to additional higher order effects.
The top quark pair background is generated with POWHEG using the CT10 PDF at NLO. The PS and the hadronisation is performed with PYTHIA 8 using the P2011C tune based on the CTEQ6L1 PDF at LO.
To check the modelling of the top-quark-pair background an additional sample is used generated by MC@NLO using the CT10 PDF at NLO and interfaced with HERWIG. The $t\bar{t}$ cross section is $\sigma_{t\bar{t}} = 253^{+15.3}_{-16.3}\,(\text{theor.})\,\text{pb}$. It has been calculated at next-to-next-to leading order (NNLO) in QCD including resummation of next-to-next-to-leading logarithmic (NNLL) soft gluon terms [86–92]. This uncertainty includes already the top-quark mass variation of $\pm 1\,\text{G}e\text{V}$.

Single-top-quark production Single top quarks can be either produced in a colourless t-channel exchange (see Figure 6.3(a)), similar to the signal process, or in a s-channel fusion of two light quarks (see Figure 6.3(b)). In addition the associated production of a top quark with a W boson is possible as shown in Figure 6.3(c). The production via the t-channel exchange starts with a b quark in the initial state and produces a top quark at the first EW vertex. This is basically the same Feynman diagram that can also be found in the signal process, and therefore processes that contain top quarks are explicitly excluded from the signal generation. Another production mechanism of single top quarks

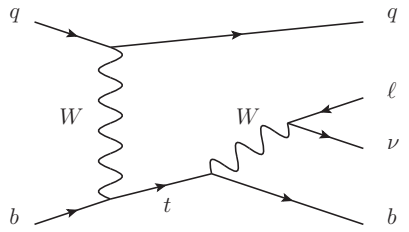

(a) Single-top-quark production via t-channel exchange.

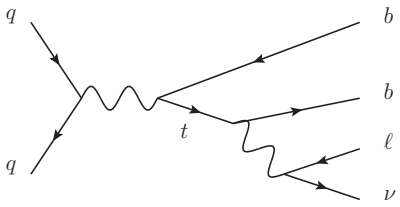

(b) Single-top-quark production via s-channel exchange.

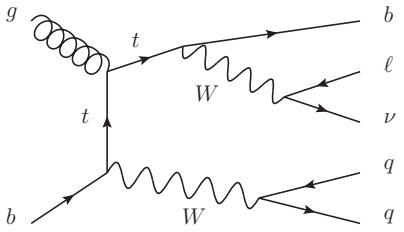

(c) Single-top-quark production in association with an additional W boson.

Figure 6.3: Different production processes for single top quarks at hadron colliders.

is due to the s-channel exchange via a W boson that decays into a top quark and a b

quark. The last production mode to mention is the associate production of a top quark with a W boson, which is similar to the diboson production shown in Figure 2.5(d). The last two processes as excluded from the diboson process due to the top quark contribution. The production of the single-top-quark background is split into three samples according to the different processes. The t-channel exchange is generated with AcerMC based on the CTEQ6L1 PDF at LO, whereas the s-channel process and the associate production are generated with MC@NLO using the CT10 PDF at NLO. The corresponding cross sections (for the leptonical decay) are calculated at NLO [93, 94] and are found to be $27.4^{+1.8}_{-1.5}$ (theor.) pb for the t-channel process, 1.7 ± 0.04 (theor.) pb for the s-channel process and 9.8 ± 0.7 (theor.) pb for the associated production with a W boson.

6.4 QCD Z + Jets Production

The production of a Z boson in association with (two) jets is identical to the production of the W boson discussed in section 6.2. Therefore, in all Feynman diagrams shown in figure 6.1 the leptonically decaying W boson can be replaced by a leptonically decaying Z boson. Instead of one charged lepton and a neutrino, two opposite charged, same flavour leptons are expected. Those events are only selected if one of the leptons is outside the detector acceptance or got lost in the reconstruction or identification. Also the $\not{E}_T$ in the event is only due to the mis-measurement of reconstructed objects.
The inclusive Z boson production is generated with Sherpa at LO using the CT10 PDF. The corresponding cross section for the QCD Z + jets process is 1122 ± 56 (theor.) pb (per lepton flavour) [85].

6.5 EW Z + Jets Production

In the Feynman diagram of the EW signal, shown in figure 2.5, the W boson can be replaced by a leptonically decaying Z boson. As explained above for the QCD Z + jets process, this process can mimic the signal signature if one of the leptons is outside the detector acceptance or gets lost in the reconstruction or identification. The cross section of the EW Z + Jets production is a factor of 10 smaller than the signal process cross section and thus the contribution is small. The samples have been generated with Sherpa using the CT10 PDF at NLO. The corresponding cross section per lepton flavour is 0.36 ± 0.04 pb. As no dedicated theory uncertainty is available for this sample and the contribution to the analysis is small, a 10% uncertainty on the cross section was assumed.

6.6 Diboson Production

As already mentioned in section 2.9 the production of a diboson process, as shown in figure 6.4(a), can have the same initial and final state as the signal with the same number of

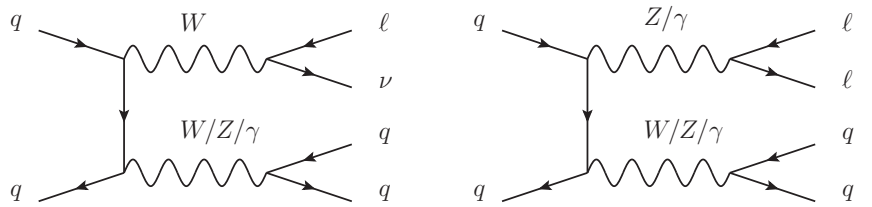

(a) Production of a W boson pair and W boson Z boson/γ pair, respectively

(b) Production of a Z boson pair and Z boson/γ W boson pair, respectively

Figure 6.4: Different types of diboson production at hadron colliders.

EW vertices, but since it is a s-channel process it can be generated on its own. Nevertheless there is a small interference with the signal process, that can be neglected in a signal enhanced region. The jets in the diboson process are coming from the decay of a vector boson (either a W boson or a Z boson) and thus their invariant mass is at the order of the corresponding boson mass, whereas the invariant mass of the two jets in the signal are much higher due to their large separation in rapidity.
The Feynman diagram in figure 6.4(b) contains no W boson at all, but a leptonically decaying Z boson, that can be mis-identified as a W boson if one of the leptons gets lost or mis-identified and therefore this is also considered as a background, although its contribution is small (see sec. 9.2.3).
All diboson backgrounds are generated with HERWIG using a CTEQ6L1 PDF at LO. The corresponding cross sections per lepton channel are $70.4 \pm 7\,(\text{theor.})$ pb for the WW process, $20.3 \pm 0.8\,(\text{theor.})$ pb for the WZ process and $7.2 \pm 0.3\,(\text{theor.})$ pb for the ZZ process [85].

6.7 Background from Multijet Processes

The majority of events at a hadron collider are final states with several jets, referred to as *multijet* events. An example of such a process is given in figure 6.5. Although most of

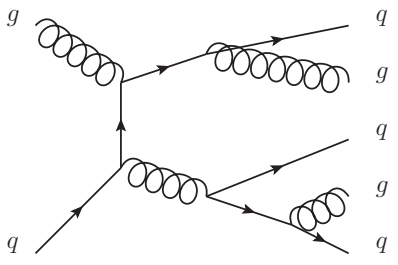

Figure 6.5: Example of an event with mutliple jets in the final state. These processes are the majority of the events at hadron colliders.

the jets are very soft, it is just the multitude of events that causes this processes to be an important background to this analysis. Each jet has a probability to be mis-reconstructed as a lepton and some of those jets will even survive the tight identification requirements for leptons, or charged leptons are produced inside a jet in a hadron decay. To model the background in a stringent signal phase space a large amount of MC events is needed. Thus, a technique was developed to describe the multijet background from collision data (see section 8).

7 — Selection

The objects reconstructed with the algorithms explained in section 4, namely electrons, muons, jets and $\not{E}_T$ are now selected with criteria derived from the signal event topology. The description of the selection is divided into the selection of the objects themselves and the selection of the events, based on combinations of several objects.

7.1 Electron Selection

In this analysis a combination of two EF triggers is used for the electron selection, which have been the lowest unprescaled triggers in the data taking period in 2012. This means that each event that got triggered is recorded, while for a prescaled trigger only a certain number of events, e.g. only every tenth event, that passes the trigger is saved to storage. The first trigger that is used is the `EF_e24vhi_medium1` [95]. The name already explains the special trigger requirements: `EF_e24` denotes it is an EF trigger for electrons with an uncalibrated p_{T} of at least 24 GeV. While `v` expresses that the p_{T} threshold varies as a function of η with lower values in regions where the measurement of the detector is less precise. In addition electrons are vetoed if they have an energy deposit of more than 1 GeV in the hadronic calorimeter. This is known as hadronic leakage and denoted by `h` in the trigger name. As implied by the `i` in the trigger name, this trigger only looks for isolated electrons. A cone around the electron is defined with $\Delta R < 0.2$. Within this cone the scalar sum of p_{T} of the additional tracks is compared to the p_{T} of the electron, this variable is referred to as $p_{\mathrm{T}}^{\mathrm{cone20}}/p_{\mathrm{T}}$. The trigger requires that the sum of the additional p_{T} has to be smaller than 10% of the electron p_{T}: $p_{\mathrm{T}}^{\mathrm{cone20}}/p_{\mathrm{T}} < 0.1$. Furthermore, the `medium1` denotes that the electron candidate has to fulfil a set of additional requirements that should ensure the quality of the electron. The requirements are similar to the ones in the offline reconstruction, which have been explained in section 4.2.
The second trigger is called `EF_e60_medium1` [95] and searches for electrons with an uncalibrated $p_{\mathrm{T}} > 60$ GeV. This trigger has no additional isolation or hadronic leakage requirements and increases the efficiency of high-p_{T} electrons, which may get rejected due to the hadronic leackage cut of the low-p_{T} trigger.

Electrons from the signal process are expected to be central with a large transverse momentum and to be isolated, i.e. to be well separated from other objects. The same track-based isolation $p_{\mathrm{T}}^{\mathrm{cone20}}/p_{\mathrm{T}}$ is defined for the electron selection as it was already used for the trigger, but now using the calibrated p_{T}. The cut in the signal selection has to be at least as hard as the trigger cut to not bias the distributions. It was decided to cut even harder at $p_{\mathrm{T}}^{\mathrm{cone20}}/p_{\mathrm{T}} = 0.05$, such that the remaining window between the signal selection $p_{\mathrm{T}}^{\mathrm{cone20}}/p_{\mathrm{T}} < 0.05$ and the trigger threshold of $p_{\mathrm{T}}^{\mathrm{cone20}}/p_{\mathrm{T}} < 0.1$ can be later on used for the definition of the template for the data-driven multijet background (see section 8.2).

The efficiency for electrons to also pass the isolation cut, when they have already passed all other quality cuts is shown in figure 7.1 as a function of electron p_{T}. The efficiency is found to be flat and $> 95\%$ in the whole range up to $p_{\mathrm{T}} = 1\,\mathrm{T}e\mathrm{V}$.

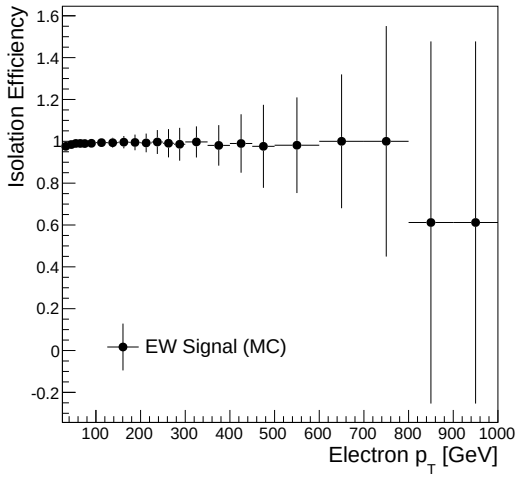

Figure 7.1: Efficiency of the isolation cut at $p_{\mathrm{T}}^{\mathrm{cone20}}/p_{\mathrm{T}} = 0.05$ as a function of electron p_{T} for the EW signal. The electrons have already passed all other selection criteria.

In addition it is required that the electron originates from the primary vertex. This is checked with the longitudinal and the radial impact parameter. Both refer to the closest approach between the track and the primary vertex. The radial impact parameter d_0 refers to the transverse plane of the track and it is required that the significance of d_0, defined as $|\frac{d_0}{\sigma_{d_0}}|$, is not larger than 3, where σ_{d_0} is the uncertainty of d_0. The longitudinal impact parameter is the z coordinate of the closest approach and its projection onto the beam axis, given by $|z_0 \sin(\theta_{track})|$, must not be larger than 0.5 mm, where θ is the angle between the beam axis and the electron track.

A detailed list of all applied selection cuts for electrons is given below:

- `EF_e24vhi_medium1` OR `EF_e60_medium1`
- *tight* identification criteria (see sec. 4.2)
- $p_{\mathrm{T}} > 25$ GeV
- $|\eta| < 2.47$
- exclude electrons in the transition region between the barrel and the end-cap calorimeter $1.37 < |\eta| < 1.52$
- Radial impact parameter: $|\frac{d_0}{\sigma_{d_0}}| < 3$
- Longitudinal impact parameter: $|z_0 \sin(\theta_{track})| < 0.5\,\mathrm{mm}$

- Track-based isolation: $p_{\mathrm{T}}^{\mathrm{cone20}}/p_{\mathrm{T}} < 0.05$

7.2 Muon Selection

As in the electron channel, a combination of a low-p_{T} trigger that requires isolated muons and a high-p_{T} trigger is used in the muon channel, namely `EF_mu24i_tight` and `EF_mu36_tight` [96]. In the muon channel the same isolation variable as in the electron channel $p_{\mathrm{T}}^{\mathrm{cone20}}/p_{\mathrm{T}}$ is used for the trigger as well as for the signal selection. The combined muon candidates that are considered by the trigger are built in a similar way as that described in section 4.3 by matching the MS with tracks from the ID. The selection starts in the MS considering the full event information. The muon candidates pass the low-p_{T} trigger if their $p_{\mathrm{T}} > 24$ GeV and $p_{\mathrm{T}}^{\mathrm{cone20}}/p_{\mathrm{T}} < 0.12$. The high-$p_{\mathrm{T}}$ trigger `EF_mu36_tight` requires a p_{T} cut of $p_{\mathrm{T}} > 36$ GeV with no additional isolation requirement. Like electrons, muons are also expected to be isolated and to have high transverse momentum, such that the basic kinematic cuts are similar between the two lepton channels. The same radial and longitudinal impact parameter cuts as for electrons are applied. The cut on the isolation variable $p_{\mathrm{T}}^{\mathrm{cone20}}/p_{\mathrm{T}}$ was again tightened compared to the cut of the low-p_{T} trigger. As in the electron channel $p_{\mathrm{T}}^{\mathrm{cone20}}/p_{\mathrm{T}} = 0.05$ was chosen, such that the remaining window can be used for the multijet template. Figure 7.2 shows the efficiency of the isolation cut as a function of muon p_{T} for muons that have already passed all other selection criteria. Also

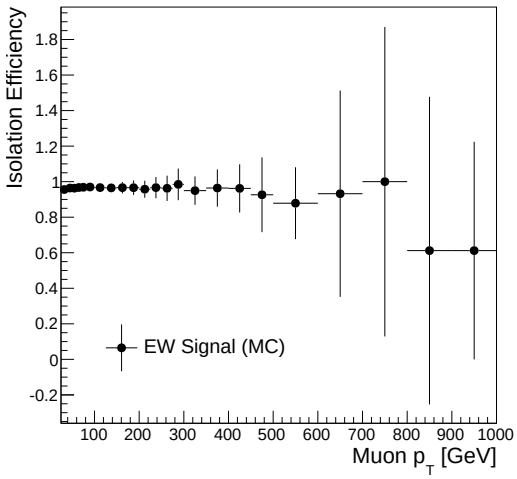

Figure 7.2: Efficiency of the isolation cut at $p_{\mathrm{T}}^{\mathrm{cone20}}/p_{\mathrm{T}} = 0.05$ as a function of muon p_{T} for the EW signal. The muons have already passed all other selection criteria.

here the efficiency is flat as a function of muon p_{T} and always $> 95\%$. The following list gives all applied selection cuts for the signal muon selection:

- `EF_mu24i_tight` OR `EF_mu36_tight`

- Identification:
  - At least one b-layer hit, if expected
  - at least 1 Pixel hit
  - ≥ 5 SCT hits
  - ≤ 2 Pixel and SCT holes
  - ≥ 5 TRT hits
- $p_{\mathrm{T}} > 25$ GeV
- $|\eta| < 2.4$
- Radial impact parameter: $|\frac{d_0}{\sigma_{d_0}}| < 3$
- Longitudinal impact parameter: $|z_0 \sin(\theta_{track})| < 0.5\,\mathrm{mm}$
- Track-based isolation: $p_{\mathrm{T}}^{\mathrm{cone20}}/p_{\mathrm{T}} < 0.05$

7.3 Jet Selection

This analysis considers only jets that have a minimal transverse momentum of $p_{\mathrm{T}} > 30$ GeV in a detector region $|\eta| < 4.4$. Jets are further removed if they are close to a charged lepton by a cut on the distance in the $\eta - \phi$ region: $\Delta R(jet, l) < 0.3$. To distinguish between jets from the hard process and jets from pile-up a discriminant is introduced, called the Jet Vertex Fraction (JVF), which is a measure for the probability of a jet to originate from a particular vertex [97]. The JVF is defined as:

$$\mathrm{JVF}(\mathrm{jet}_i, \mathrm{PV}_j) = \frac{\Sigma_k\, p_{\mathrm{T}}(\mathrm{track}_k^{\mathrm{jet}_i}, \mathrm{PV}_j)}{\Sigma_n \Sigma_l\, p_{\mathrm{T}}(\mathrm{track}_l^{\mathrm{jet}_i}, \mathrm{PV}_n)} \tag{7.1}$$

For jet i the p_{T} of all tracks that are associated to vertex j are summed in the numerator, while in the denominator the p_{T} of all tracks from the jet associated to vertex j and to all other vertices is summed. This definition is based on tracks and can therefore only be used for central jets in the ID acceptance ($|\eta| < 2.4$). In addition pile-up jets are typically low-p_{T} jets and thus the cut on the JVF is only applied on jets with $p_{\mathrm{T}} < 50$ GeV. It is required that for those jets at least 50% of the tracks originate from the primary vertex (PV): $|\mathrm{JVF}| \geq 0.5$.

7.4 Basic W + Jets selection

After the description of the object selection in the previous sections, the event selection for the EW W + jet signal will now be presented. The events are selected by requiring exactly one charged lepton, either a muon or an electron that passes the above mentioned object selection. In addition a cut on $\not{E}_T > 25$ GeV and on the transverse W boson mass, m_T, is applied at $m_T > 40$ GeV. Due to the neutrino the W boson mass cannot be reconstructed and the following definition is used that is based on objects in the transverse plane:

$$m_T = \sqrt{2p_T^{lep} \cdot \not{E}_T[1 - \cos(\Delta\phi(\text{lep}, \not{E}_T))]} \tag{7.2}$$

To suppress the background from Z boson production, there is an additional veto on events with a second, same flavour, lepton, with loosened selection criteria. For events in the electron channel, no second electron is allowed that passes at least the *medium* criteria and has $p_T > 20$ GeV. In the muon channel the events are rejected if there is a second muon that passes all muon cuts except the isolation and the impact parameter cuts. The cut on the transverse momentum is again $p_T > 20$ GeV. Figure 7.3 shows the number of jets (normalised to unit area) at reconstruction level for the EW signal in red and in blue for the QCD W + jets background. The ME of the signal process contains two partons at LO, which ideally will be reconstructed as two jets. The clustering of the jets and the kinematic cuts explained above lead to a loss of jets, such that also for the signal, events with none or only one jet get measured. The majority of background events has no jets or

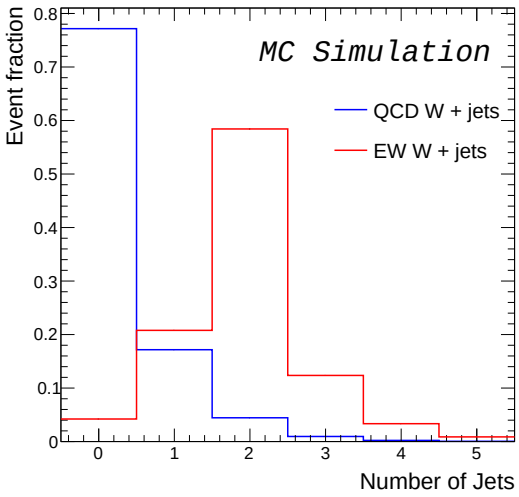

Figure 7.3: Number of jets at reconstruction level: The EW signal is shown in red and the QCD W + jets background in blue. The distributions are normalized to unit area.

only one jet. Therefore, requiring at least two jets removes > 80% of that background and

only about 20% of the signal. For events with more than two jets it has to be defined which two are the so-called *taggingn jets*. The jets from the signal process are expected to be in the forward region with high p_T and therefore the two jets with the highest p_T (leading and subleading jet) are defined as the tagging jets. Figure 7.4 shows the (normalised) p_T distribution for the leading (Fig. 7.4(a)) and the subleading (Fig. 7.4(b)) jet for the EW signal and the QCD W + jets process after the reconstruction. The p_T spectra for the two jets are found to be harder for the signal process than for the QCD W + jets background, such that additional p_T cuts are introduced to further reduce the background. Those cuts

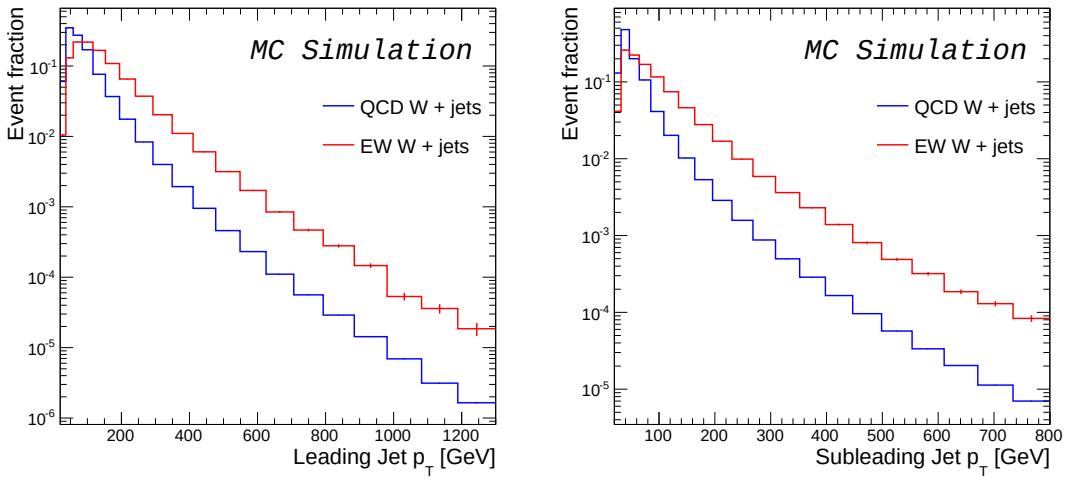

(a) Leading Jet p_T

(b) Subleading Jet p_T

Figure 7.4: Comparison of the normalised p_T distributions for EW signal (red) and QCD W + jets background (blue), for the leading (7.4(a)) and the subleading (7.4(b)) jet at reconstruction level.

are optimised based on the product of efficiency and purity of the signal. The efficiency is defined as:

$$\text{efficiency} = \frac{\text{signal events after a certain cut}}{\text{all signal events}} \tag{7.3}$$

The distribution of the efficiency as a function of the leading (subleading) jet p_T cut is shown as the blue curve in figure 7.5(a) (7.5(b)), respectively. In the lowest bin no cut on the jet p_T has been applied and the efficiency is one. With an increasing p_T cut the efficiency decreases and so does the signal statistic. The purity is defined as:

$$\text{purity} = \frac{\text{signal events after a certain cut}}{\text{signal and background events after a certain cut}} \tag{7.4}$$

The red curve in figure 7.5(a) (7.5(b)) shows the signal purity as a function of the leading (subleading) jet p_T. A tighter p_T cut reduces the background and raises the signal purity.

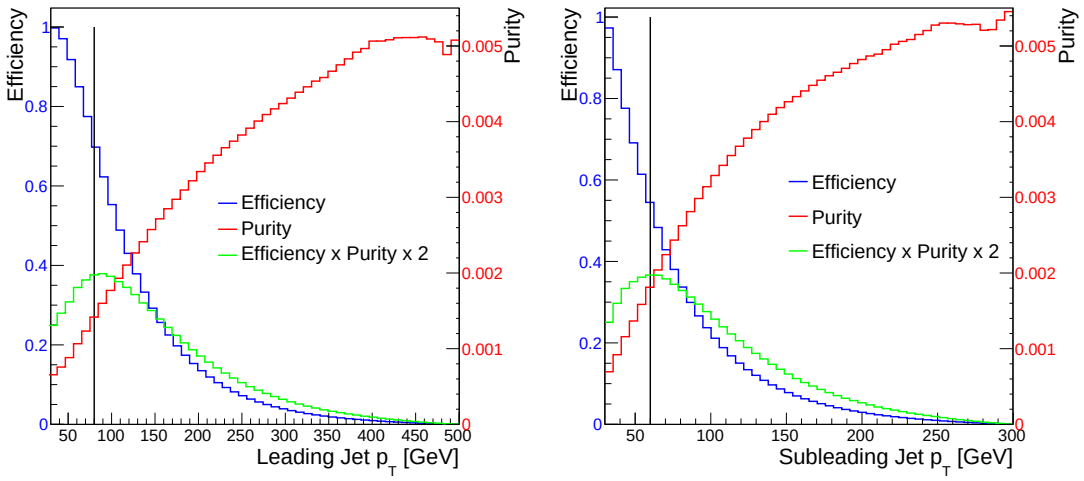

(a) Leading Jet p_{T}

(b) Subleading Jet p_{T}

Figure 7.5: Efficiency (blue) and purity (red) as well as the product efficiency × purity (green) for the EW signal as a function of the leading (7.5(a)) and the subleading (7.5(b)) jet p_{T}. The y-axis on the left hand side corresponds to the efficiency, while the y-axis on the right hand side corresponds to the purity. The product efficiency × purity is scaled by a factor of 2 to be visible on the plot and also corresponds to the right hand side y-axis. The black line indicates the cut value, that was chosen with respect to the maximum of the efficiency × purity distribution.

A high signal purity is favoured for the analysis, but this can only be achieved by loosing events, so that one has to compromise between those two opposing effects. The best cut is defined where the product of efficiency and purity, shown as the green curve in figure 7.5, is maximised. The resulting cuts are $p_{\mathrm{T}} > 80$ GeV ($p_{\mathrm{T}} > 60$ GeV) for the leading (subleading) jet, which are indicated as a black line in the plots. This selection is further referred to as the *inclusive W + jets* selection.

7.4.1 Reconstruction Level Plots in the inclusive Phase Space

After the basic selection of a W boson with at least two high p_{T} jets, the prediction from the theory is compared to collision data in various distributions. The backgrounds and the EW signal (described in section 6) are normalised to the measured integrated luminosity and stacked in one histogram that should match the corresponding data histogram. The estimation of the multijet background, as the only data-driven background will be discussed in detail in section 8, but of course is needed to compare the signal and background predictions to data. All distributions are shown separately for the two lepton channels to spot possible mis-modelling, which could be different in the two channels and potentially cancel in a combined plot. Figure 7.6 shows the lepton p_{T} and the $\not\!\!E_T$ distribution on the left hand side for the electron channel and on the right hand side for the muon channel. The MC is grouped into four different categories: the EW signal shown in red, which contains in addition to the EW $W \to e\nu/\mu\nu$ prediction taken from POWHEG, the contribution of EW $W \to \tau\nu$ events generated with SHERPA. In this phase space the fraction of signal events is small and hardly visible on the plots. The QCD W + jets prediction is shown in white and has the largest contribution in this phase space ($\approx 60\%$). The contributions from top-quark-pair production and single-top-quark production are summed and shown in green, denoted as *Top*. The remaining processes that have only a small contribution, like diboson production and QCD and EW Z boson production are combined and referred to as *Other*. Those are shown in dark blue. On the bottom of the stack plot, shown in light blue is the multijet background, that will be explained in detail in section 8. The data are shown as black points with error bars corresponding to the statistical uncertainties. The statistical uncertainty due to the MC prediction is shown as a grey shaded band on top of the stack. The panel below the stacked plot shows the ratio between data and the stacked signal and background prediction. This allows to check the size of any deviation in the comparison. The errors bars on the data points are again due to the statistical uncertainty, while the statistical uncertainty on the stack is shown as the yellow band in the background. It can be seen in figure 7.6 that the signal and background expectation agrees within 10% with the data up to $p_{\mathrm{T}} = 1\,\mathrm{T}e\mathrm{V}$. The $\not\!\!E_T$ distribution shows a larger mis-modelling, especially in the muon channel, which is not covered by the statistical uncertainty. Unfortunately, not all uncertainties that have to be taken into account in the measurement are available for the $\not\!\!E_T$ distribution and thus is can not be stated if the detected deviations will be covered by them. What can further be mentioned is the difference in the shape of the multijet background in the electron and the muon channel. This arises most probably from the different sources of events contributing to the background and will be discussed in chapter 8.

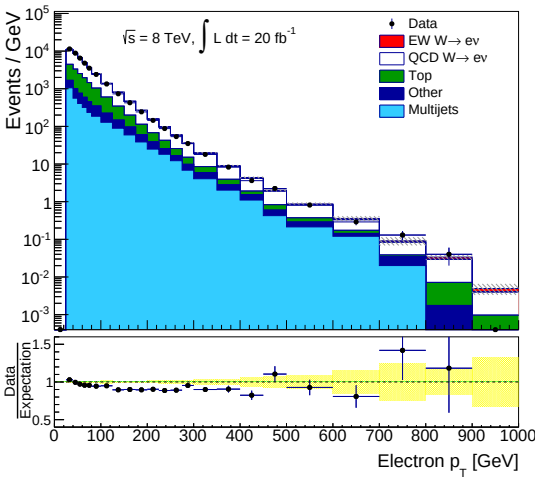

(a) electron channel

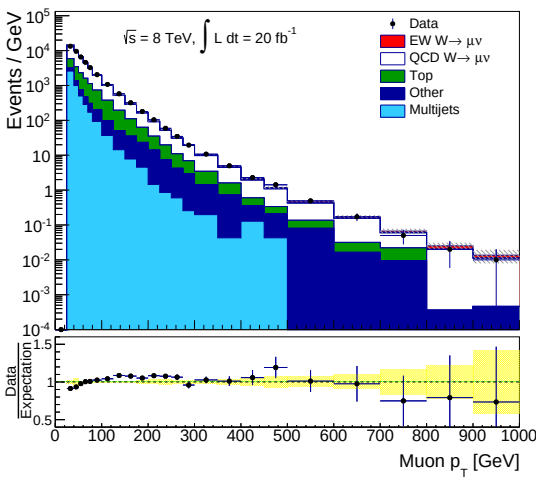

(b) muon channel

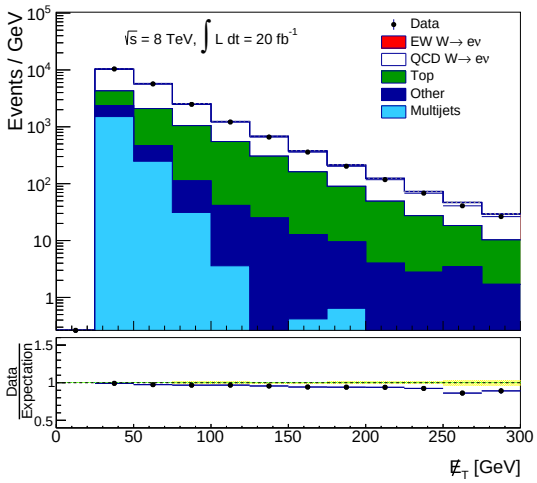

(c) electron channel

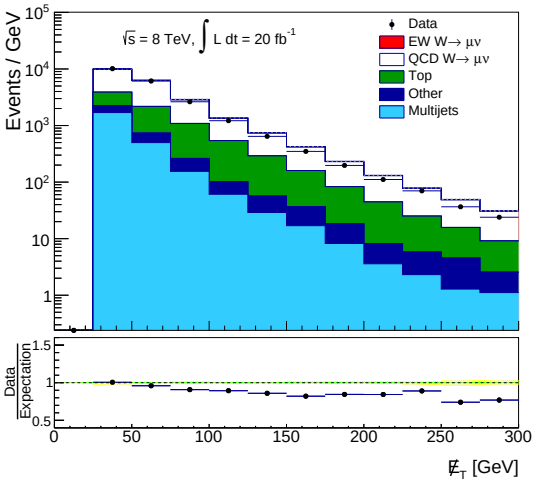

(d) muon channel

Figure 7.6: Lepton p_{T} and $\not{E}_T$ distribution in the inclusive W + jets phase space for the electron and muon channel. The data are shown as black points with error bars corresponding to the statistical uncertainty. The lower plot panel shows the comparison of the stacked signal and background components with the data. The grey shaded band in the upper panel and the yellow band in the lower panel indicate the statistical uncertainty on the sum of predicted signal and background.

Figure 7.7 shows the p_{T} distribution for the leading (fig. 7.7(a) and fig. 7.7(b)) and the subleading jet (fig. 7.7(c) and fig. 7.7(d)). As already explained, the jet kinematics are essential for the separation of the EW signal from the QCD W + jets background. In both channels a good modelling of the tagging jets up to $p_{\mathrm{T}} = 1\,\mathrm{TeV}$ is found. Besides the p_{T} distributions of the jets, other variables that combine the two tagging jets are important for the analysis and are used to define a phase space that enhances the signal, these will be explained in the next sections. Detailed event numbers for the different processes are given in table 7.1 and table 7.2 for the electron and muon channel, respectively.

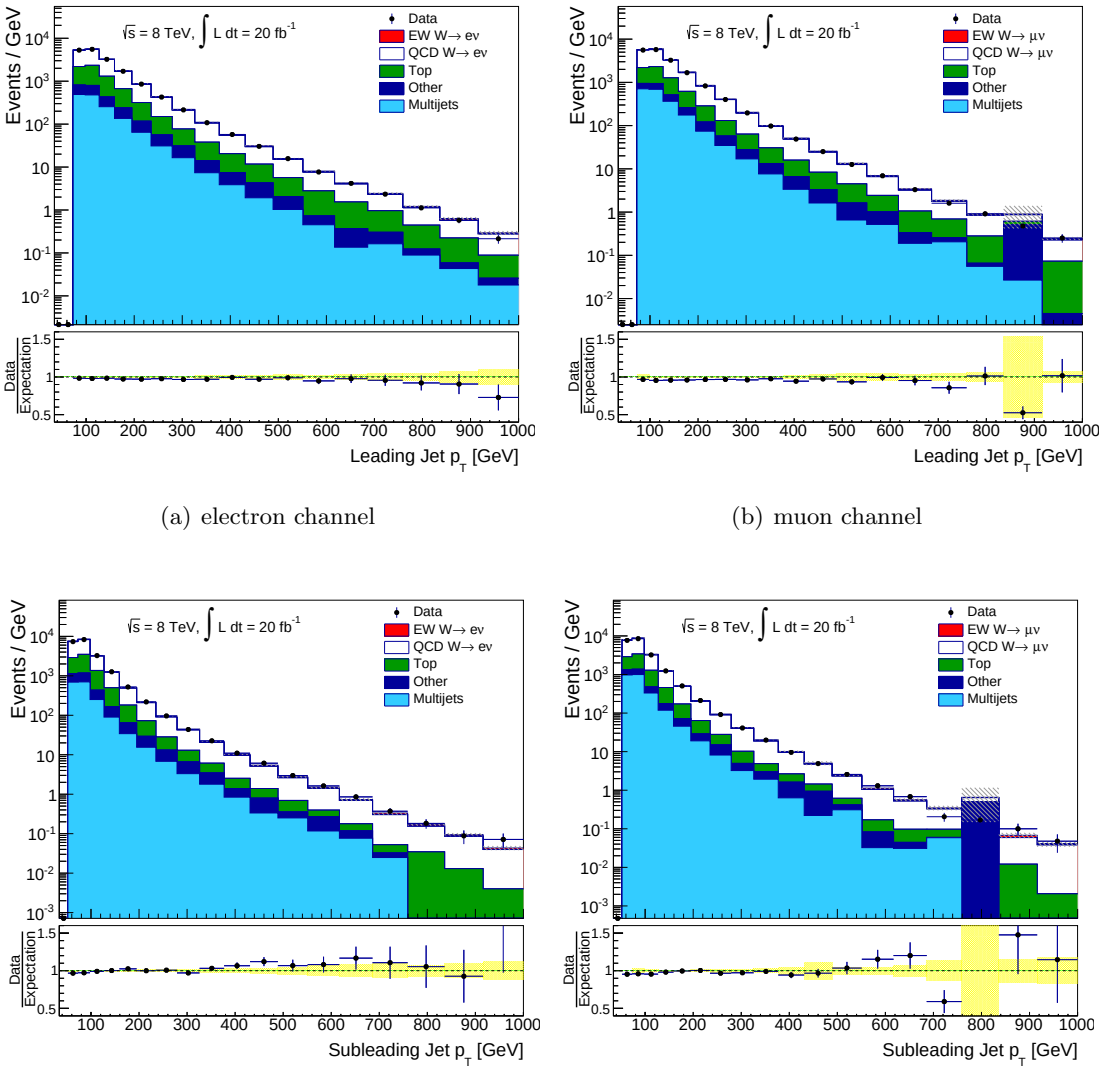

(a) electron channel

(b) muon channel

(c) electron channel

(d) muon channel

Figure 7.7: Leading and subleading jet p_{T} distribution in the inclusive W + jets phase space for the electron and muon channel. The data are shown as black points with error bars corresponding to the statistical uncertainty. The lower plot panel shows the comparison of the stacked signal and background predictions with the data. The grey shaded band in the upper panel and the yellow band in the lower panel indicate the statistical uncertainty on the sum of predicted signal and background.

7.5 Additional Selection Criteria sensitive to Vector Boson Fusion

After the selection of the W boson in association with (at least) two high-p_{T} jets has been introduced, the signal purity should be further increased by additional cuts, mainly based on the kinematics of the tagging jets. The reconstruction level distributions in the following sections refer to the inclusive W + jets phase space unless otherwise stated, and thus can be compared to the plots from the previous sections.

7.5.1 Invariant Mass of the Dijet System

The large angle between the tagging jets in the signal process leads to a large invariant dijet mass (M_{jj}) of the dijet system. Before optimising a cut on this variable the modelling in the inclusive W + jets phase space is shown in figure 7.8 for the electron (fig 7.8(a)) and the muon channel (fig 7.8(b)). The M_{jj} distribution is later used for extracting the

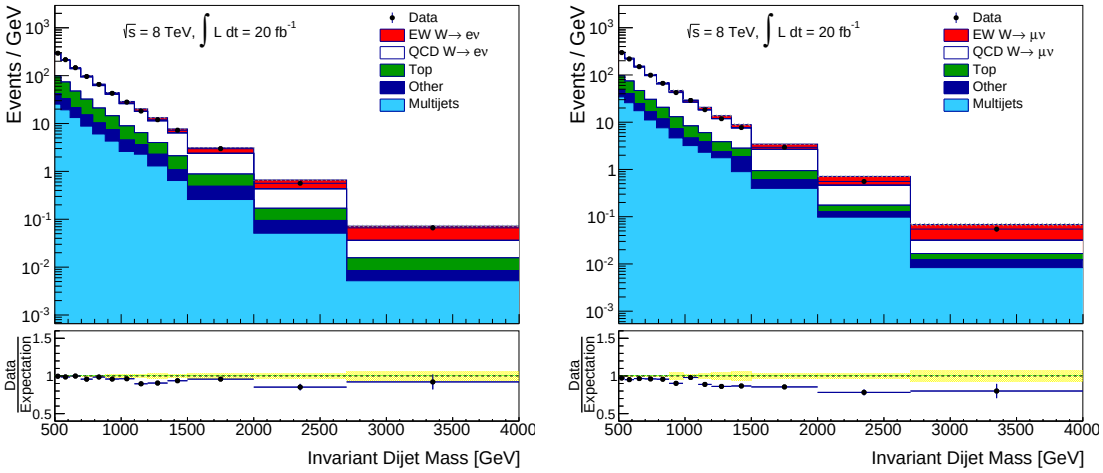

(a) electron channel

(b) muon channel

Figure 7.8: Invariant dijet mass distribution in the inclusive W + jets phase space for the electron and muon channel. The data are shown as black points with error bars corresponding to the statistical uncertainty. The lower plot panel shows the comparison of the stacked signal and background components with the data. The grey shaded band in the upper panel and the yellow band in the lower panel indicate the statistical uncertainty on the sum of predicted signal and background.

signal strength and tested up to $\mathrm{M}_{jj} = 4\,\mathrm{TeV}$. Also here the deviations between the data and the sum of expected signal and background are mostly within 20% and mainly

covered by the statistical uncertainty (again, the full set of uncertainties are not available for the comparison). Other uncertainties as theoretical uncertainties on the signal and the backgrounds have not yet been taken into account. Figure 7.9(a) shows the normalised M_{jj} distribution for the signal (red) and the QCD W + jets background (blue). Also

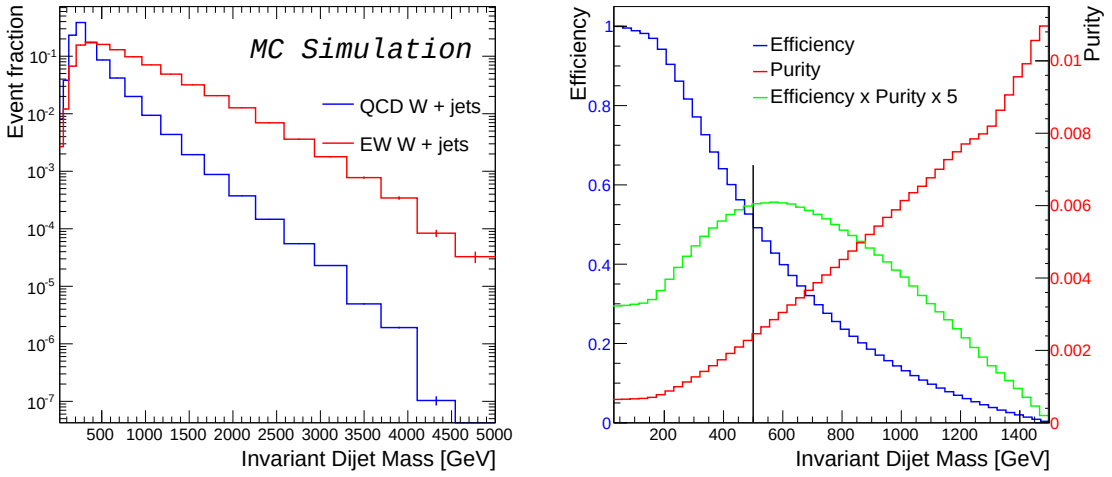

(a) Normalised M_{jj} distributions

(b) Efficiency and purity distributions

Figure 7.9: Figure 7.9(a) shows the comparison of the normalised M_{jj} distributions for EW signal and QCD W + jets background at reconstruction level. Figure 7.9(b) shows the efficiency and purity as well as the product efficiency × purity for the EW signal as a function of M_{jj}. The y-axis on the left hand side belongs to the efficiency, while the y-axis on the right hand side belongs to the purity. The product efficiency × purity is scaled by a factor of 5 to be visible on the plot and belongs also to the right hand side y-axis. The black line indicates the cut value, that was chosen with respect to the maximum of the efficiency × purity distribution.

here in the signal prediction a much harder spectrum is found than in the background prediction. The latter peaks at low values (< 300 GeV) and drops steeply, while the signal peaks at higher values with a long tail to high M_{jj} values. An additional cut is introduced based on the product of efficiency and purity. As can be seen in figure 7.9(b) the optimal cut is around $M_{jj} > 500$ GeV.

7.5.2 Rapidity Gap between the Tagging Jets

To further suppress the QCD W + jets background the rapidity gap between the tagging jets, defined as $\Delta y_{j_1,j_2} = y_1 - y_2$ is used. The distributions at reconstruction level in the inclusive W + jets phase space can be seen in figure 7.10. The rapidity gap is highly correlated with the M_{jj} of the tagging jets and thus the same good modelling is found.

For this plot the $M_{jj} > 500$ GeV cut has not been applied. The background peaks at $\Delta y_{j_1,j_2} = 0$, because the two jets are often produced in a gluon splitting or via gluon radiation and therefore a small angle between them is expected, whereas the signal peaks at values $|\Delta y_{j_1,j_2}| > 2$ (but hardly visible on the plot).

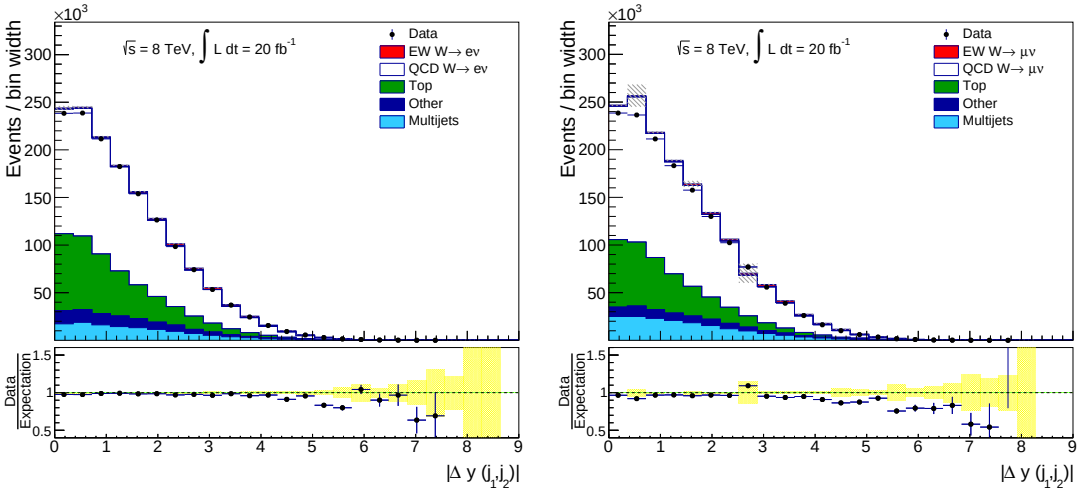

(a) electron channel

(b) muon channel

Figure 7.10: $|\Delta y_{jj}|$ distribution in the inclusive W + jets phase space for the electron and muon channel. The data are shown as black points with error bars corresponding to the statistical uncertainty. The lower plot panel shows the comparison of the stacked signal and background components with the data. The grey shaded band in the upper panel and the yellow band in the lower panel indicate the statistical uncertainty on the sum of predicted signal and background.

In figure 7.11(a) the shape of the $\Delta y_{j_1,j_2}$ distribution is shown for the EW signal in red and the QCD W + jets background in blue. As these distributions are used to find the optimal cut on $|\Delta y_{j_1,j_2}|$ the $M_{jj} > 500$ GeV cut is already applied and changes the shape of the background significantly. A high M_{jj} cut removes most events with a small angle between the tagging jets and thus the QCD W + jets background looks more like the signal and does no longer peak at $|\Delta y_{j_1,j_2}| = 0$. Nevertheless there are still differences that can be used to further reduce the QCD W + jets background. To find the optimal cut the product of efficiency and purity is used. The product as well as the distributions of efficiency and purity as a function of the absolute value of the rapidity gap are shown in figure 7.11(b). The optimal cut in terms of the product of efficiency and purity is found around $|\Delta y_{jj}| = 2$.

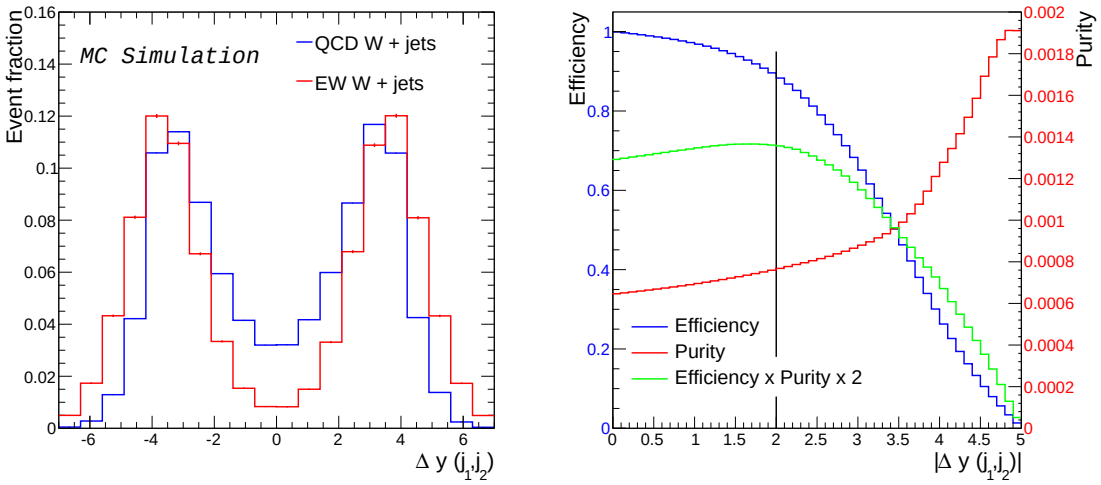

(a) Normalised Δy_{jj} distributions

(b) Efficiency and purity distributions

Figure 7.11: Figure 7.11(a) shows the comparison of the normalised Δy_{jj} distributions for EW signal and QCD W + jets background. Figure 7.11(b) shows the efficiency and purity as well as the product efficiency $\times$ purity for the EW signal as a function of $|\Delta y_{jj}|$. The y-axis on the left hand side belongs to the efficiency, while the y-axis on the right hand side belongs to the purity. The product efficiency $\times$ purity is scaled by a factor of 2 to be visible on the plot and belongs also to the right hand side y-axis. The black line indicates the cut value, that was chosen with respect to the maximum of the efficiency $\times$ purity distribution.

7.5.3 Lepton Centrality

In the EW signal process the W boson is preferably emitted in the gap between the two tagging jets and thus its decay products are also expected central in the detector acceptance. The QCD W + jets background has no such clear event topology and the lepton is more or less randomly distributed with respect to the jets. This feature can be used to further distinguish between the EW signal and the main background process. An *outside-lepton-veto*, that vetoes events where the lepton is not found inside the rapidity gap, can be used. Instead of a binary decision if the lepton is inside or outside the rapidity gap, a variable, referred to as (lepton) Centrality, has been developed which describes continuously where the lepton is found:

$$C_\ell = \frac{\eta_\ell - \frac{\eta_{j1}+\eta_{j2}}{2}}{\eta_{j1} - \eta_{j2}} \tag{7.5}$$

It can easily be seen that $C_\ell = 0.5$ ($C_\ell = -0.5$) if the lepton matches the leading (subleading) jet in rapidity. In the middle of the rapidity gap the Centrality becomes minimal ($C_\ell = 0$). This implies that for a lepton outside the rapidity gap the (absolute value of the) Centrality is always larger 0.5. Therefore, C_ℓ is expected to peak at 0 for the EW signal process, whereas no sharp peak is anticipated for the background. This can be seen in figure 7.12(a), where the lepton Centrality distribution for the EW signal in red and in blue for the QCD W + jets background are shown after the M_{jj} and the $|\Delta y_{jj}|$ cut. Especially for the background a slight asymmetry in the distribution is found which points to another feature of the Centrality definition. In the case where the lepton has $C_\ell > 0$ the distance between the lepton and the leading jet (in rapidity) is smaller than the distance between the lepton and the subleading jet, whereas in the region $C_\ell < 0$, the lepton is closer to the subleading jet. The dominant production mechanisms for the QCD W + jets background are shown in figure 6.1: In figure 6.1(a) the p_T of the two quarks has to balance the W boson production. All additional energy from the initial gluons will result in a boost of the W boson in the same direction as the high energy jet. The same argument is true for figure 6.1(d). No such clear effect will be seen from the Feynman diagrams in figure 6.1(b) and 6.1(c). The modelling of the lepton Centrality variable is tested in the inclusive W + jets phase space at reconstruction level in figure 7.13. A good agreement between the prediction of the EW signal and the backgrounds with the data is found. In the muon channel around $|C_\ell| = 0.2$ a dip in the distribution is found with a large statistical uncertainty on the bin, which comes most probably from a missing event with a high event weight. But the sum of predicted signal and background events in this bin still agrees with the data within the (large) statistical uncertainty. The optimal cut on the lepton Centrality variable is determined again by the product of efficiency and purity as shown in figure 7.12(b). The maximum is found as $0.3 < C_\ell < 0.4$, and thus the looser cut at $C_\ell < 0.4$ was chosen.

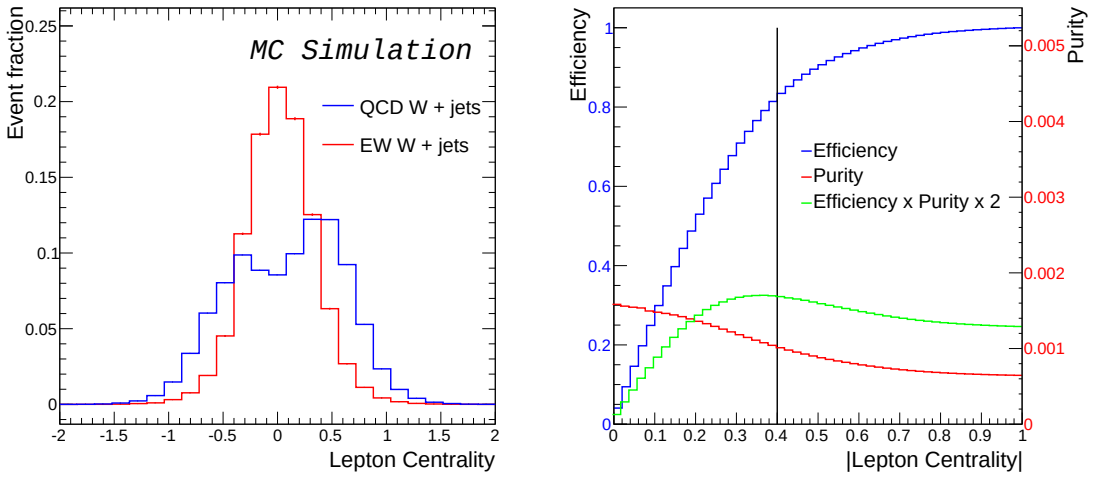

(a) Normalised lepton Centrality distributions

(b) Efficiency and purity distributions

Figure 7.12: Figure 7.12(a) shows the comparison of the normalised lepton Centrality distributions for EW signal and QCD W + jets background after the M_{jj} and the $|\Delta y_{jj}|$ cut. Figure 7.12(b) shows the efficiency and purity as well as the product efficiency × purity for the EW signal as a function of the lepton Centrality. The y-axis on the left hand side corresponds to the efficiency, while the y-axis on the right hand side corresponds to the purity. The product efficiency × purity is scaled by a factor of 2 to be visible on the plot and it also corresponds to the right hand side y-axis. The black line indicates the cut value that was chosen with respect to the maximum of the efficiency × purity distribution.

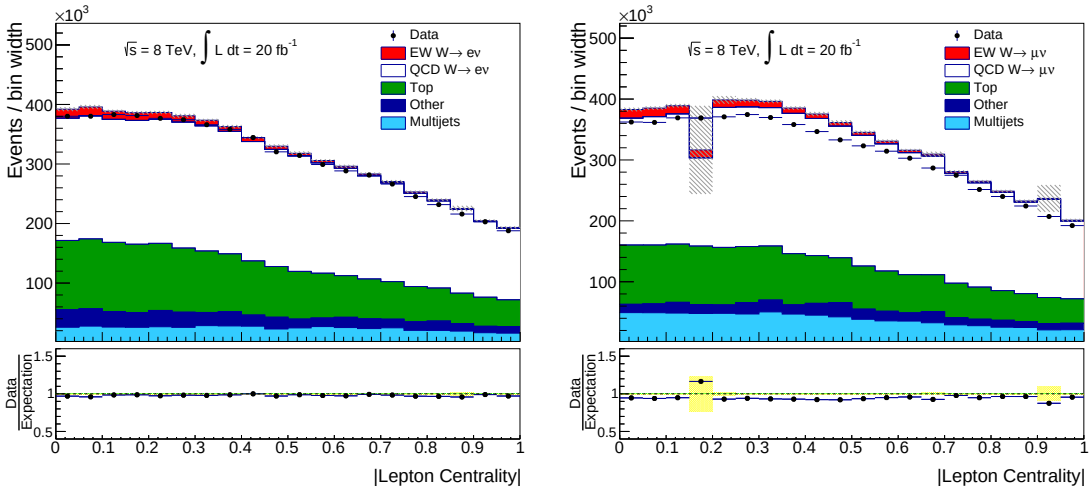

(a) electron channel

(b) muon channel

Figure 7.13: Lepton Centrality distribution (absolute value) in the inclusive W + jets phase space for the electron and muon channel. The data are shown as black points with error bars corresponding to the statistical uncertainty. The lower plot panel shows the comparison of the stacked signal and background components with the data. The grey shaded band in the upper panel and the yellow band in the lower panel indicate the statistical uncertainty on the sum of predicted signal and background.

7.5.4 Jet Centrality

The signal process has only a colourless t-channel exchange of particles and therefore no additional hadronic interaction is expected in the rapidity gap between the tagging jets. The same Centrality variable as above for the lepton is defined for each additional jet (third jet and above) and referred to as jet Centrality:

$$C_{\text{jet}} = \frac{\eta_{\text{jet}} - \frac{\eta_{j1}+\eta_{j2}}{2}}{\eta_{j1} - \eta_{j2}} \tag{7.6}$$

Figure 7.14(a) shows the normalised jet Centrality distributions for all additional jets in the event after all cuts defined in the previous sections, for the EW signal in red and the QCD W + jets background in blue.

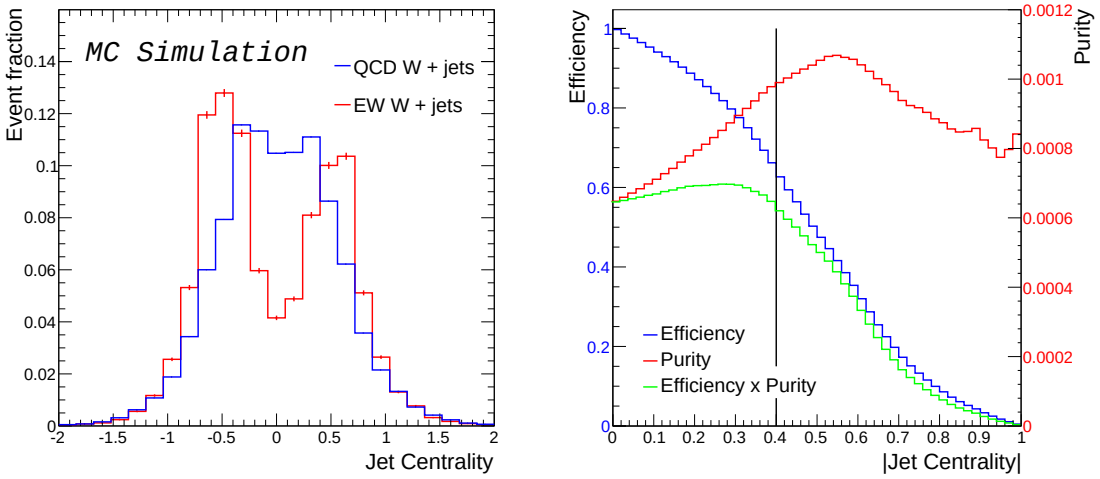

(a) Normalised jet Centrality distributions

(b) Efficiency and purity distributions

Figure 7.14: Figure 7.14(a) shows the comparison of the normalised jet Centrality distributions for EW signal and QCD W + jets background after all introduced cuts. Figure 7.14(b) shows the efficiency and purity as well as the product efficiency × purity for the EW signal as a function of the jet Centrality. The y-axis on the left hand side corresponds to the efficiency, while the y-axis on the right hand side corresponds to the purity and the product efficiency × purity. The black line indicates the cut value.

Again an asymmetry is found for the signal and the background process, but with an opposite effect than for the lepton Centrality. The additional jets appear to have a smaller distance (in rapidity) to the subleading jet than to the leading jet. Especially in the signal, where the effect seems to be much clearer, it is easy to understand. At leading order there are only two jets, and thus additional jets are produced via QCD radiation. This leads

to the initial jet loosing energy, and producing a new jet, that is close to the initial one. The behaviour of the Centrality variable, that was found for the lepton, remains of course unchanged, such that $C_{\text{jet}} = 0.5$ ($C_{\text{jet}} = -0.5$) if the additional jet matches one of the tagging jets. In contrast to the lepton Centrality distribution the jet Centrality peaks around $C_{\text{jet}} = \pm 0.5$ for the signal, which effectively means the additional jets are mostly in the forward region and close to the tagging jet, whereas the background distribution shows no sharp peak, but rather a wide maximum at around 0. The product of efficiency and purity in figure 7.14(b) would indicate a cut around $|C_{\text{jet}}| > 0.3$, unfortunately the cut value was chosen a little tighter in the past at $|C_{\text{jet}}| > 0.4$. Many of the theoretical uncertainties were evaluated with the higher jet Centrality cut and therefore it was decided to continue using this cut value. The loss of signal efficiency, as indicated by the blue curve in figure 7.14(b), is about 10%. Again a good agreement of the jet centrality was found in the inclusive W + jets phase space for the electron and the muon channel as can be seen in figure 7.15.

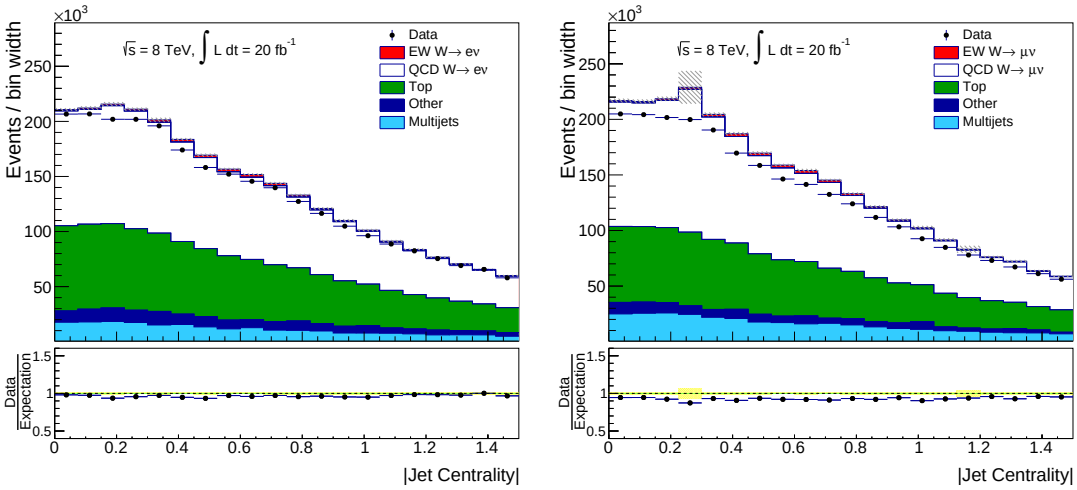

(a) electron channel

(b) muon channel

Figure 7.15: Jet Centrality distribution (absolute value) in the inclusive W + jets phase space for the electron and muon channel. The data are shown as black points with error bars corresponding to the statistical uncertainty. The lower plot panel shows the comparison of the stacked signal and background components with the data. The grey shaded band in the upper panel and the yellow band in the lower panel indicate the statistical uncertainty on the sum of predicted signal and background.

7.5.5 Modelling in the VBF Region

The application of all the selection cuts previously explained is further referred to as *VBF selection* and defines the phase space where the cross section measurement of the EW signal is performed. The efficiency of the selection cuts for the EW signal is $> 30\%$, which increases the signal fraction from $< 2\%$ in the inclusive phase space to $\approx 16\%$ in the VBF phase space. The efficiency for the QCD W + jets background is only $\approx 3\%$. Because of the change of the other backgrounds, the fraction of the QCD W + jets background is found to be stable at $\approx 60\%$ in both phase spaces. In addition a significant reduction from $\approx 26\%$ to $\approx 11\%$ of the top background, consisting of the single-top-quark production and the top-quark-pair production, is also achieved. Essential for the cross section measurement in chapter 10 is the M_{jj} distribution in the VBF phase space, which can be seen in figure 7.16, on the left hand side for the electron channel and on the right hand side for the muon channel. A good modelling up to $M_{jj} = 4\,\mathrm{T}e\mathrm{V}$ is found, with

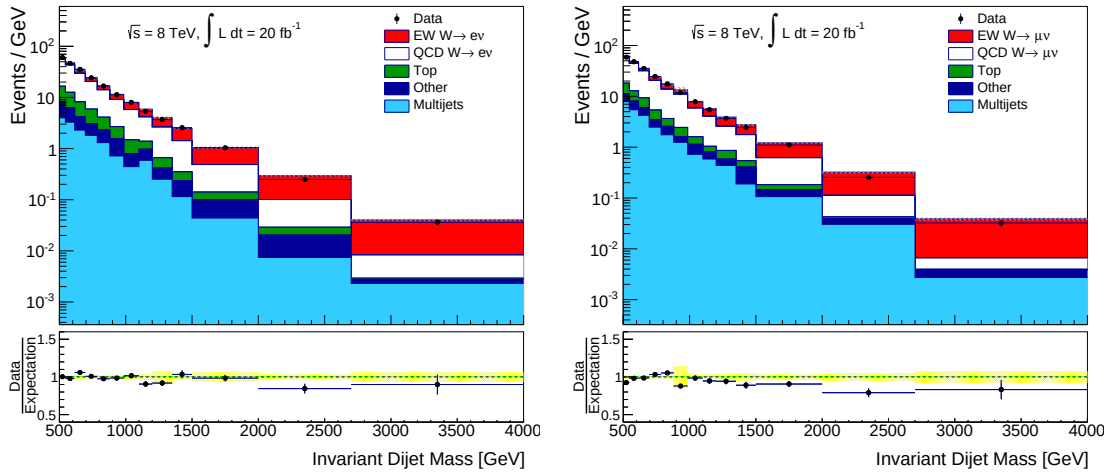

(a) electron channel

(b) muon channel

Figure 7.16: Invariant dijet mass distribution in the VBF phase space for the electron and muon channel. The data are shown as black points with error bars corresponding to the statistical uncertainty. The lower plot panel shows the comparison of the stacked signal and background components with the data. The grey shaded band in the upper panel and the yellow band in the lower panel indicate the statistical uncertainty on the sum of predicted signal and background.

the signal contribution being now clearly visible on the plot. Additional distributions at reconstruction level in the VBF phase space can be found in appendix A. Detailed event yields for the different processes are given in table 7.1 and table 7.2[1] for the electron and

[1]The additional phase spaces given in the tables will be explained in the following section.

muon channel, respectively.

Table 7.1: Event yields for the different phase spaces in the electron channel

	Inclusive	VBF	Control	High Mass
EW $W \to e\nu$	7,727	2,731	614	1,170
EW $W \to \tau\nu$	168	49	24	24
QCD $W \to e\nu$	317,541	10,090	10,243	1,389
QCD $W \to \tau\nu$	7,967	167	142	15
$t\bar{t}$	121,485	1,023	728	89
single top	18,521	862	434	102
Multijets	44,702	1,152	1,686	194
QCD $Z \to ee$	19,114	647	461	96
QCD $Z \to \tau\tau$	1,078	25	32	6
WW	2,161	96	40	15
ZZ	59	2	1	0
WZ	723	30	12	6
EW $Z \to ee$	184	35	12	13
Total expected	541,430	16,909	14,429	3,119
Data	530,531	16,853	14,200	2,977
Data / Expectation	0.98	1.00	0.98	0.95

Table 7.2: Event yields for the different phase spaces in the muon channel

Cut Name	Inclusive	VBF	Control	High Mass
EW $W \to \mu\nu$	8,059	2,722	742	1,169
EW $W \to \tau\nu$	174	31	19	22
QCD $W \to \mu\nu$	343,469	10,675	12,268	1,449
QCD $W \to \tau\nu$	8,590	201	386	31
$t\bar{t}$	104,701	739	668	61
stop	17,149	696	456	89
Multijets	61,865	1,906	2274	301
QCD $Z \to \mu\mu$	11,914	420	556	73
QCD $Z \to \tau\tau$	1,175	32	44	5
WW	2,422	108	49	18
ZZ	36	1	1	0
WZ	736	35	12	5
EW $Z \to \mu\mu$	154	40	15	15
Total expected	560,444	17,606	17,490	3,238
Data	538,339	17,040	16,324	2,980
Data / Expectation	0.96	0.97	0.93	0.92

7.6 Control Region Definition

The modelling of the QCD W + jets background, especially in the M_{jj} distribution, is essential for the fit that is performed for the cross section measurement. Therefore, a control region (CR) is defined that enhances the QCD W + jets background, while suppressing the other backgrounds and the EW signal. This CR has to have similar kinematics as the VBF region and in addition it needs enough statistics to not be dominated by the statistical uncertainties. Inverting the lepton centrality cut, and therefore requiring the lepton not to be central between the two tagging jets, while keeping all other cuts as in the definition of the VBF region, is found to be a good choice for the CR. It was also tested to invert the $|\Delta y_{jj}|$ or the jet Centrality cut. Inverting the $|\Delta y_{jj}|$ cut results in too low statistics due to the high correlation between Δy_{jj} and M_{jj}. With an inverted jet Centrality cut, which means that a third jet has to be within the tagging jets, the modelling of the two jet events can be tested. However, those events are the major contribution to the signal phase space. In the W + jets control region with the inverted lepton Centrality cut, the fraction of the QCD W + jets background is increased up to $\approx 72\%$ in both channels, while the signal fraction is decreased down to $< 5\%$. Figure 7.17 shows the M_{jj} distribution for the electron and muon channel in the CR. In both channels the ratio of data and the stacked signal and background prediction is flat and any deviations are covered by the statistical uncertainty. The QCD W + jets background is taken from Powheg which contains the QCD prediction at NLO. The detailed event numbers for the W + jets control region are given in table 7.1 and table 7.2 in the previous section for the electron and muon channel, respectively.

For the cross section measurement and for testing the triple gauge boson vertex, an additional prediction for the QCD W + jets background is used, which is taken from Sherpa at LO in QCD. The M_{jj} distribution in the W + jets control region using the prediction from Sherpa is shown in figure 7.18. A clear mis-modelling of the MC prediction is found in both lepton channels, which indicates that the MC predicts too many events in the high M_{jj} tail. It is expected that the Sherpa background does not model the M_{jj} distribution very well, as this was already seen in a previous analysis [98]. A direct comparison of the M_{jj} distribution between the Sherpa and the Powheg prediction is shown in figure 7.19 at reconstruction level in the VBF phase space. This illustrates how large the difference between these two predictions is where the tagging jets in the Powheg prediction have, on average, a much smaller invariant mass. This ratio reflects the differences in the ME calculation and also in the PS simulation. Using the prediction from Sherpa to account for an uncertainty in the measurement results in a large $> 20\%$ uncertainty (will be discussed in section 10.2). Taking into account the known mis-modelling seems to overestimate the uncertainty on the QCD W + jets modelling. A reweighting of the Sherpa QCD W + jets shape is performed with a reweighting function obtained from the direct comparison to data. Therefore, the signal and all other backgrounds, apart from the QCD W + jets background were subtracted from the data in the M_{jj} distribution in the W + jets control region. The resulting data shape contains only the QCD W + jets component and can directly be compared to the prediction from Sherpa at reconstruction level. The ratio between the data and the Sherpa prediction, combined for the two lepton channels, is

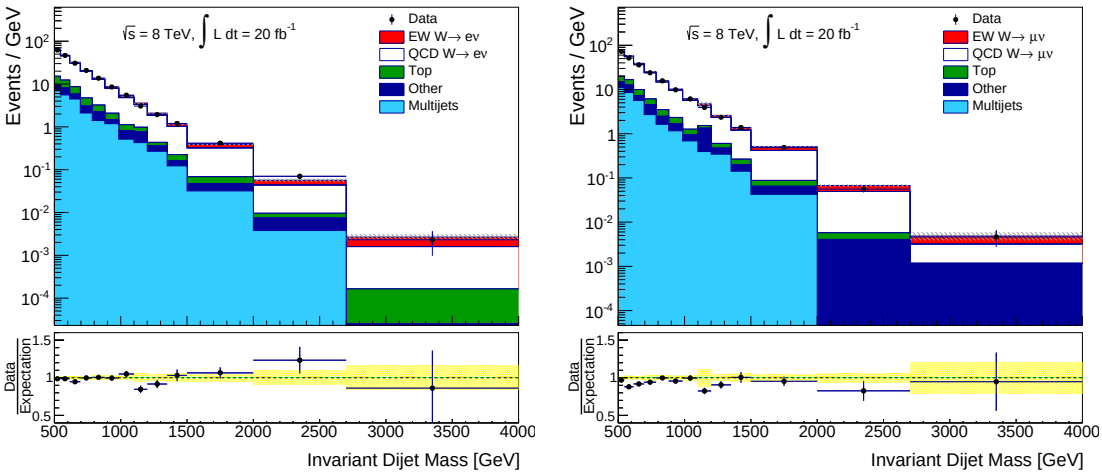

(a) electron channel

(b) muon channel

Figure 7.17: Invariant dijet mass distribution in the W + jets control region for the electron and muon channel, with the QCD W + jets background taken from POWHEG. The data are shown as black points with error bars corresponding to the statistical uncertainty. The lower plot panel shows the comparison of the stacked signal and background components with the data. The grey shaded band in the upper panel and the yellow band in the lower panel indicate the statistical uncertainty on the sum of predicted signal and background.

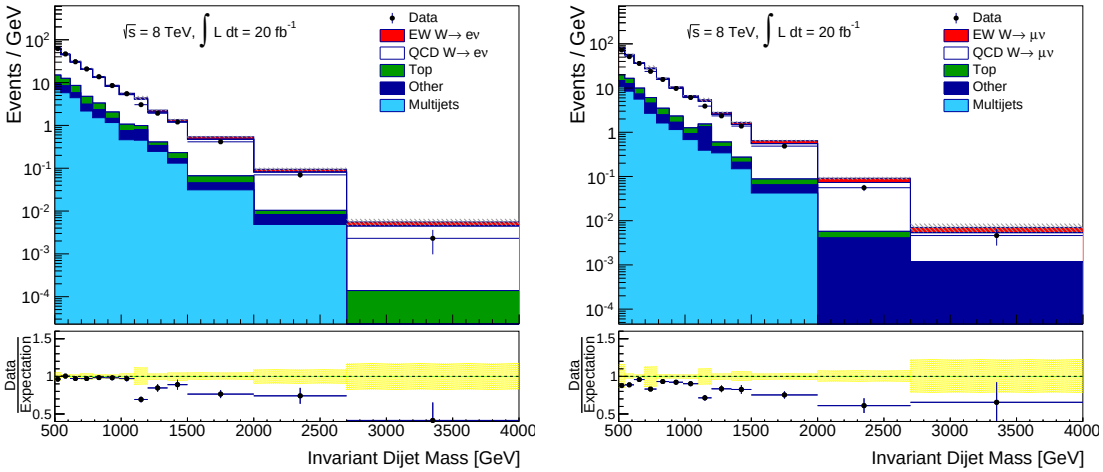

(a) electron channel (b) muon channel

Figure 7.18: Invariant dijet mass distribution in the W + jets control region for the electron and muon channel, with the QCD W + jets background taken from SHERPA. The data are shown as black points with error bars corresponding to the statistical uncertainty. The lower plot panel shows the comparison of the stacked signal and background components with the data. The grey shaded band in the upper panel and the yellow band in the lower panel indicate the statistical uncertainty on the sum of predicted signal and background.

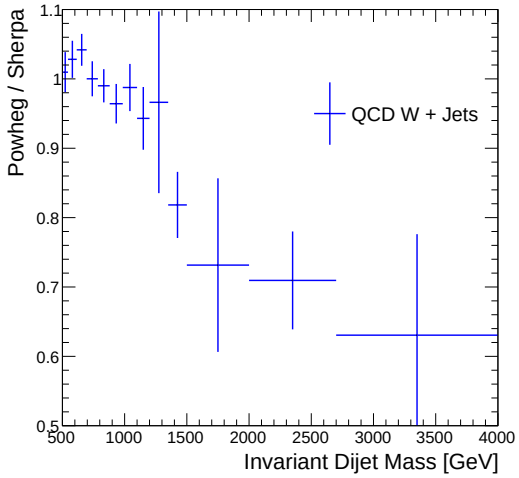

Figure 7.19: Ratio of the QCD W + jets background predicted by POWHEG at NLO and SHERPA at LO as a function of the M_{jj} distribution at reconstruction level. The error bars reflect the statistical uncertainties of the two predictions.

shown in figure 7.20, where the error bars correspond to the statistical uncertainty. The ratio is fitted with a linear function, that is further used to reweight the SHERPA sample at reconstruction level.

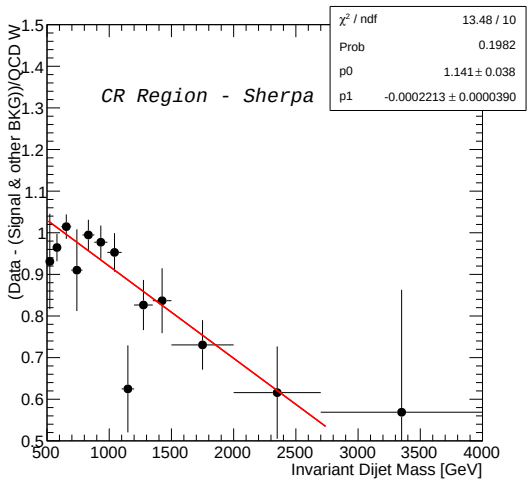

Figure 7.20: After subtracting the signal and the other (non-QCD W + jets) backgrounds from data, the ratio of the remaining data events and the QCD W + jets background is shown. The ratio is fitted with a linear function.

Figure 7.21 shows the M_{jj} distribution at reconstruction level using the reweighted SHERPA prediction for the QCD W + jets background. A significant improvement in the comparison to data could be achieved. As already mentioned the QCD W + jets prediction from SHERPA is used in the cross section measurement and the limit setting to test the modelling of the QCD W + jets background. Therefore, not only the nominal reweighting is tested, but also variations of the reweighting function within the uncertainties of the parameters, as given in figure 7.20. This will be further explained in chapter 9.

7.7 Definition of High M_{jj} Phase Space

To probe the coupling at the $WWZ/WW\gamma$ vertex, a new phase space is defined where the signal purity can be increased. This is done in two steps. First of all the M_{jj} cut is increased to 1 TeV, and the resulting phase space is referred to as the *high mass* phase space. The fraction of signal events could be raised to $\approx 40\%$, while the fraction of the QCD W + jets background is decreased to $< 50\%$. The fraction of events due to top-quark-pair and single-top-quark production and from multijet processes is $< 10\%$. The remaining event numbers for the high mass phase space can be found in table 7.1 and table 7.2 for electron and muon channel, respectively. This phase space is not directly used for the limit setting but is the starting point for the second step: Because the three boson vertex is sensitive to the momentum transfer in the hard interaction, which is directly connected

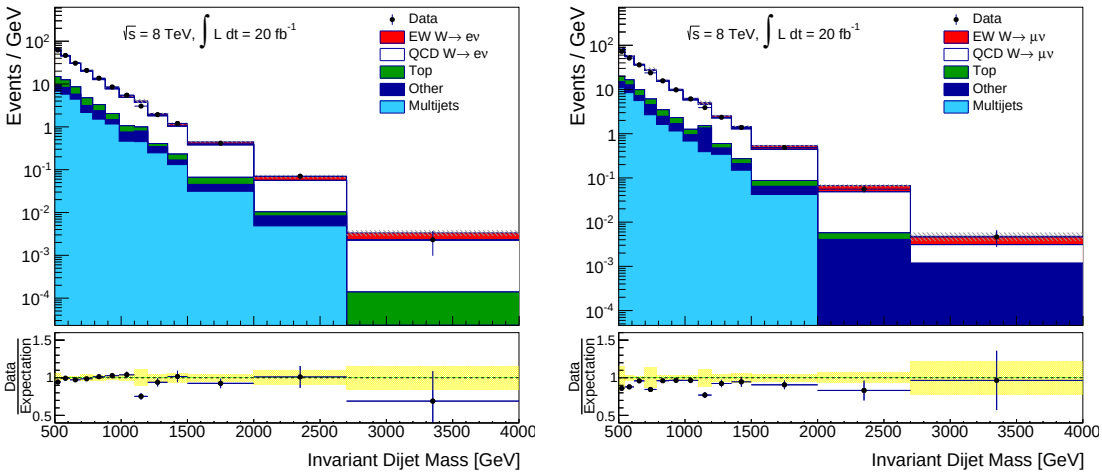

(a) electron channel

(b) muon channel

Figure 7.21: Invariant dijet mass distribution in the W + jets control region for the electron and muon channel, with the QCD W + jets background taken from the reweighted SHERPA sample. The data are shown as black points with error bars corresponding to the statistical uncertainty. The lower plot panel shows the comparison of the stacked signal and background components with the data. The grey shaded band in the upper panel and the yellow band in the lower panel indicate the statistical uncertainty on the sum of predicted signal and background events.

to leading jet p_{T}, an additional cut is introduced on this distribution. The optimisation of the cut value will be described in section 11.4.
A summary of the cuts of all defined phase spaces that are relevant for the analysis is given in table 7.3.

Table 7.3: Definition of the various phase spaces used in this analysis.

	Inclusive	VBF	Control	High Mass
N_{Jets}	≥ 2			
Jet p_{T}	$\mathrm{Jet}_1 > 80$ GeV, $\mathrm{Jet}_2 > 60\,\mathrm{GeV}$			
M_{jj}	-	> 500 GeV		> 1 TeV
$\lvert\Delta y(j_1, j_2)\rvert$	-	> 2		
$\lvert C_j \rvert$	-	> 0.4		
$\lvert C_\ell \rvert$	-	< 0.4	> 0.4	< 0.4

8 — Data-driven Multijet Background

The background due to multijet processes, as shown in figure 6.5, where a jet is mis-identified as a lepton, is difficult to be predicted by MC. The cross section of these processes is high, but in the generation most of the jets are soft or collinear and do not pass the event selection. This results in a low-statistics MC sample with accordingly high uncertainties in the measurement. To extract a reliable shape and to determine the normalisation of the background in the relevant phase space, a data-driven technique is developed that selects a template from collision data by relaxing or inverting the lepton quality criteria. The normalisation of the template (further referred to as *multijet template*) is estimated by a fit to data in a variable that is sensitive to the shape of the multijet background. This is done in a kinematic region that is similar to the signal phase space. For each lepton channel an independent template is selected and a separate fit is performed. In section 8.1 the overall strategy, which is common for both channels, is explained, while in section 8.2 and 8.3 the details for the electron and muon channel are discussed separately. The results of both channels are summarised in section 8.4.

8.1 General Procedure

When constructing a data-driven multijet template by loosening the lepton criteria, the overall assumption is that the shape of these selected events reflects the shape of the background in all relevant distributions. Therefore, the kinematics of the selected events have to be similar to the kinematics of the events that pass the signal selection.

Template Selection It can be distinguished between different classes of events that contribute to the multijet background: One class are events with jets that are mis-identified as a lepton in the calorimeter. These events are suppressed by isolation requirements, either track based or calorimeter based. In addition there are events with real leptons stemming from a secondary vertex of a heavy flavour decay. These leptons are also not isolated and can further be reduced by stringent impact parameter requirements. Inverting or loosening the impact parameter or isolation cut can therefore be used to construct a data-driven multijet template, that is orthogonal to the signal selection, while still all kinematic cuts can be applied. For the electron channel, there is a third source of events that include electrons originating from photon conversions in the calorimeter. These events can be enhanced in the multijet template by relaxing the electron identification requirements.

Contamination with Real Leptons Although the multijet template is enriched with events from fake leptons and heavy flavour decays, there are still events from the signal and other background processes, which are taken from MC, that survive the multijet

selection. To remove these events from the multijet template, all signal and background MC samples are run through the multijet selection and the remaining events are subtracted from the template. This is done by a bin-by-bin subtraction of the histograms in all distributions, where bins with resulting negative content are set to 0.

Fit Variable The inclusive W + jets phase space, the VBF phase space and the W + jets control region have such different kinematics, that the fit for extracting the normalisation of the multijet background is performed separately for each phase space. Therefore, for each kinematic region a corresponding multijet phase space is defined with the same kinematic cuts, but without the $\not\!\!E_T$ and the m_T cut, to enhance the fraction of multijet background events. The $\not\!\!E_T$ for backgrounds from multijet processes is due to a loss of particles or mis-measured energy in the calorimeter. Therefore, the background is expected to peak at low values, whereas the signal and the main backgrounds have large $\not\!\!E_T$. The $\not\!\!E_T$ distribution is used as the default variable for the multijet fit, where the fit range was chosen as $10 < \not\!\!E_T < 250\,\mathrm{GeV}$. This includes the low $\not\!\!E_T$ region where the multijet background peaks as well as the tail where only the MC backgrounds and the signal are left. This is important as the QCD W + jets background is also allowed to float.

Extraction of the Multijet Normalisation In the fit for extracting the normalisation three different templates are considered: the multijet template, a template from the QCD W + jets background and a third template that includes all other backgrounds and the signal. The normalisation of the last template is fixed in the fit whereas the normalisation of the multijet template as well as the normalisation of the QCD W + jets background are allowed to float. The results of the multijet fit are given as a scale factor (SF) for each template. A SF is defined as the number of events obtained from the fit divided by the initial number of the events. For the QCD W + jets background (and all other MC processes) the initial number of events is the SM prediction, while for the multijet background it is the number of events selected by the multijet selection. The extracted SF for the multijet background has no direct physical meaning, it basically reflects the statistics of the template. A SF close to one implies that the multijet template contains roughly as many events as expected for the multijet background. Thus a multijet template with a resulting SF not much larger than 1 is preferred. With a fraction of $\approx 60\%$ the QCD W + jets process is the largest background with a non-negligible theoretical uncertainty. Its SF is expected to be close to 1, as this would reflect the SM prediction, but even a $\pm 15\%$ difference would still be covered by the uncertainties. However, the final normalisation of the QCD W + jets background is determined when extracting the signal strength in the cross section measurement (chapter 10). Therefore, the QCD W + jets SF from the multijet fit is only extracted as a cross check and further neglected in the analysis. The goodness of the fit is tested by calculating the χ^2 within the fit range. This should not be much larger than the number of degrees of freedom (NDF), which is the number of bins (40) with the fit parameters (2, number of floating components) subtracted.

8.2 Electron Channel

The dominant source of the multijet background in the electron channel is due to jets that are mis-identified in the calorimeter, besides smaller contributions from heavy flavour decays and photon conversion. For the multijet template, events are selected with an electron that fulfils the *medium* identification requirement, instead of the *tight* requirement. In addition, the isolation on the electron is loosened. As described in section 4.2 the lowest unprescaled single electron trigger for the 2012 dataset already requires $p_{\mathrm{T}}^{\mathrm{cone20}}/p_{\mathrm{T}} < 0.1$. Therefore, the isolation cut for the signal selection was tightened to $p_{\mathrm{T}}^{\mathrm{cone20}}/p_{\mathrm{T}} < 0.05$, which removes less than 5% of the EW signal, if all other selection cuts on the electron have already been applied. The remaining isolation window between the signal selection cut and the trigger cut is used to define the multijet template. The upper cut on $p_{\mathrm{T}}^{\mathrm{cone20}}/p_{\mathrm{T}}$ was chosen to be even tighter at $p_{\mathrm{T}}^{\mathrm{cone20}}/p_{\mathrm{T}} < 0.09$ to be far below the trigger threshold.

A clear mis-modelling of the electron p_{T} distribution is detected when using both triggers from the signal selection, which can be seen in figure 8.1(a) in the inclusive W + jets phase space.

As a consequence of the second trigger in the electron channel, too many events are selected in the high-p_{T} tail. This trigger was originally introduced to enhance the fraction of high-p_{T} electrons that fail the low-p_{T} trigger due to the hadronic leakage cut. While for low-p_{T} electrons a high handronic leackage is a hint for the electron being a fake, high-p_{T} electrons which traverse through the EM calorimeter and leak into the hadronic calorimeter, produce significant hadronic leakage. These electrons should not be removed from the selection, and therefore the second trigger is introduced to enhance the efficiency for those high-p_{T} electrons. In the nominal electron selection most events in the region above $p_{\mathrm{T}} > 60$ GeV are selected by both triggers. In the inclusive W + jets and the VBF selection, only 2% of all events fail the low-p_{T} trigger cut while passing the high-p_{T} trigger cut. It was found that this fraction is very different for the multijet template. In the VBF multijet (inclusive W + jets) selection the fraction is found to be $\approx 19\%$ ($\approx 18\%$). This can be explained by the difference in the shape of the isolation variable for events triggered by at least the low-p_{T} trigger (or both triggers) and the events that got selected by only the high-p_{T} trigger. Figure 8.2 shows the normalised distributions of the $p_{\mathrm{T}}^{\mathrm{cone20}}/p_{\mathrm{T}}$ variable in the inclusive W + jets phase space. The blue curve shows the events that are selected with only the high-p_{T} trigger, while the red curve refers to events selected by (at least) the low-p_{T} trigger. The isolation of the low-p_{T} trigger drops steeply, while the isolation for the high-p_{T} trigger events is more flat, and thus the fraction of the events as a function of the isolation is not stable and leads to an over estimate of events in the high-p_{T} tail of the electron. To improve the modelling of the lepton p_{T} distribution the high-p_{T} trigger is removed for the multijet template selection[1]. In figure 8.1(b) it can

[1] It will be explained later (sec. 9.1) that SFs are applied to the MC prediction to account for inefficiencies in the trigger selection. Those SFs, which are applied event-by-event, are usually close to 1 and thus the resulting effect on the analysis is small (compared to the relatively large uncertainties e.g. due to the jet energy scale). Unfortunately those corrections are only available for the combination of the two triggers and thus cannot be applied to a selection with only one trigger. This affects only the real lepton components taken from MC which will be subtracted from the multijet template. Taken into account

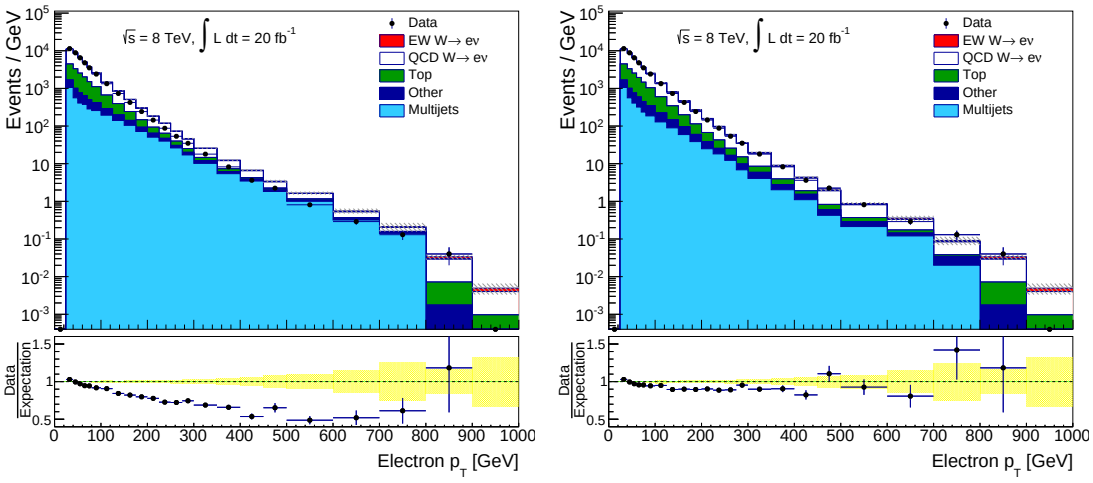

(a) Both triggers

(b) Only low-p_{T} trigger

Figure 8.1: The plots show the electron p_{T} distribution at reconstruction level after the inclusive W + jets selection. On the left hand side plot the multijet template is selected with both triggers, whereas on the right hand side plot the multijet template is selected using only the low-p_{T} trigger. The signal and the MC background processes are normalised to their SM prediction. The data are shown as the black points with error bars due to the statistical uncertainty. The lower panel shows the ratio between the data and the stacked prediction. The grey shaded band in the upper panel and the yellow band in the lower panel show the statistical uncertainty on the sum of the signal and the backgrounds.

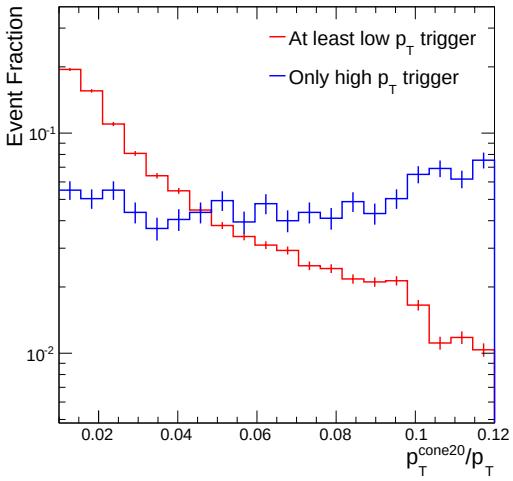

Figure 8.2: Normalised distribution of the $p_{\mathrm{T}}^{\mathrm{cone20}}/p_{\mathrm{T}}$ variable for events selected by only the high-p_{T} trigger (blue) and for events that are selected with the low-p_{T} trigger. Events are taken from data in the inclusive W + jets phase space.

be seen that the modelling of the electron p_{T} is significantly improved with the modified template. Figure 8.3 shows the ratio of the two templates as a function of the electron p_{T} (figure 8.3(a)) and the invariant dijet mass (figure 8.3(b)).

A clear slope can be detected in the electron p_{T} distribution above $p_{\mathrm{T}} > 60$ GeV, which is responsible for the mis-modelling of the lepton p_{T} distribution shown in figure 8.1(a). In the region below the trigger threshold of the high-p_{T} trigger the ratio is always at 1, which is expected as the same events are selected. In the tail of the electron p_{T} distribution up to 80% of the events stem from the high-p_{T} trigger. Figure 8.3(b) shows the ratio of the two templats in the M_{jj} distribution, which is found to be flat, but has a $10 - 15\%$ normalisation difference.

Table 8.1 summarises the differences between the signal selection and the selection for the nominal multijet template.

Table 8.1: Summary of the differences between the signal selection and the selection of the multijet template.

	Trigger	Electron ID	Isolation
Signal	EF_e24vhi_med. OR EF_e60_med.	tight	$p_{\mathrm{T}}^{\mathrm{cone20}}/p_{\mathrm{T}} < 0.05$
Multijet	EF_e24vhi_medium	medium	$0.05 < p_{\mathrm{T}}^{\mathrm{cone20}}/p_{\mathrm{T}} < 0.09$

that the effect due to the SFs in general is small and no further uncertainties are evaluated on the real lepton component, as their effect on the multijet background is expected to be small, it was decided that the trigger SFs on the real lepton component are a sub-dominant component on the multijet template and can be neglected.

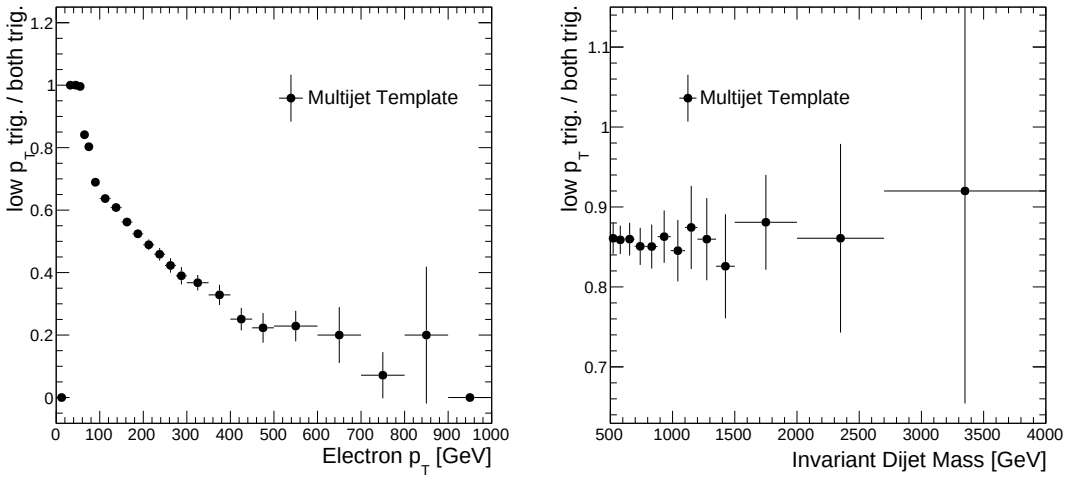

(a) Electron p_{T}

(b) Invariant dijet mass

Figure 8.3: The ratio of the two multijet templates, one selected with both triggers and the other with only the low-p_{T} trigger, as a function of the electron p_{T} and the invariant dijet mass.

As already described, the number of real electrons that survive the multijet selection have to be subtracted from the multijet template and therefore all backgrounds and the signal, taken from MC are passed through the multijet selection. The subtraction is done before the fit is performed. The contamination of the multijet template with real electrons as a function of $\not{E}_T$ is shown for the VBF multijet selection in figure 8.4(a) and for the VBF selection in figure 8.4(b).

The contamination is found to be $\approx 24\%$ in the VBF phase space and $\approx 7\%$ in the VBF multijet phase space, respectively. The contamination with signal events is quoted separately and is found to be $\approx 2.4\%$ in the VBF phase space and $\approx 0.6\%$ in the VBF multijet phase space. For the inclusive W + jets and inclusive W + jets multijet selection a comparable contamination with real leptons of $\approx 25\%$ and $\approx 7\%$ is found. The contamination with signal events is in both cases $< 0.5\%$.

After subtracting the real electrons, the normalisation of the template is fitted. As already explained the fit is performed in the inclusive W + jets multijet phase space and the VBF multijet phase space as well as in the multijet phase space that is defined for the W + jets control region. The results are shown in figure 8.5, where the SFs for the multijet template and the QCD W + jets background are printed directly on the plot. The third component, that contains the remaining backgrounds and the signal is not allowed to float, therefore its SF is held constant at 1. The data are shown as the blue points, with error bars corresponding to the statistical uncertainty. The fit range used is indicated with the two red vertical lines on the plots. The lower panel in the plots shows the comparison of the sum of signal and background to the data. In all three phase space, where the fit was

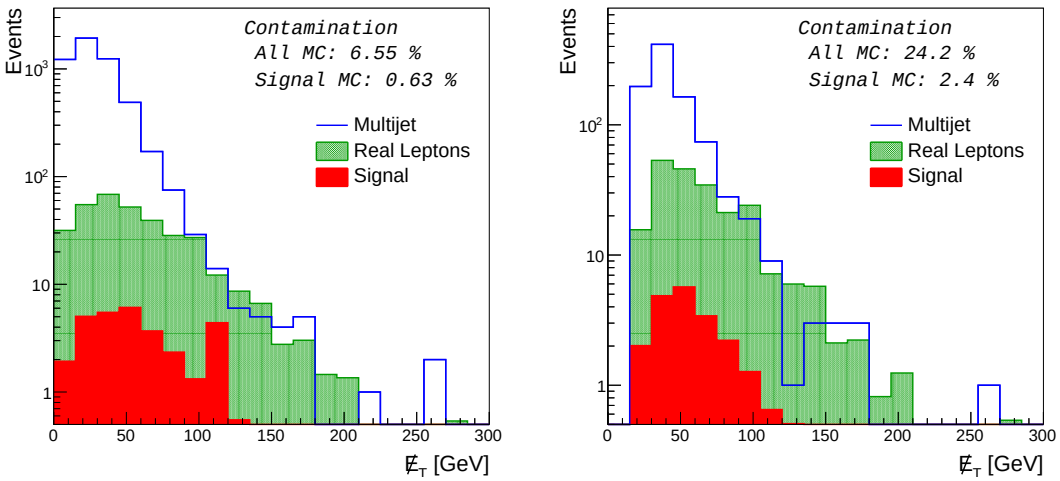

(a) VBF multijet selection

(b) VBF selection

Figure 8.4: Contamination of the multijet template with real electrons as a function of $\not\!\!E_T$ for the VBF and the VBF multijet phase space. The blue curves shows the multijet template shape and the green shape shows the real electron prediction from MC normalised to SM prediction. The amount of signal events from MC is made visible by the red curve. The predicted events with real leptons are subtracted bin-by-bin from the multijet template, where resulting negative bins are set to zero.

performed, a good agreement with the data was found up to $\not{E}_T = 300\,\mathrm{G}e\mathrm{V}$, this is also verified by a good χ^2/NDF ratio. The SF for the multijet background is found to be in the range between 1.65 and 2.12, which confirms that the selected multijet template contains enough statistics, especially in the stringent VBF region. The SF for the QCD W + jets background is found to be in a $\pm 10\%$ window around its SM prediction, which is covered by the expected range of uncertainty for this background. Between the different phase spaces the SF for the QCD W + jets background agrees roughly within the statistical uncertainty of the fit. Based on the fit results the fraction of multijet events is found to be 8% in the inclusive W + jets phase space, 12% in the W + jets control region and 7% in the VBF phase space. All results for the multijet background in the electron and the muon channel are also summarized in table 8.2 at the end of this chapter.

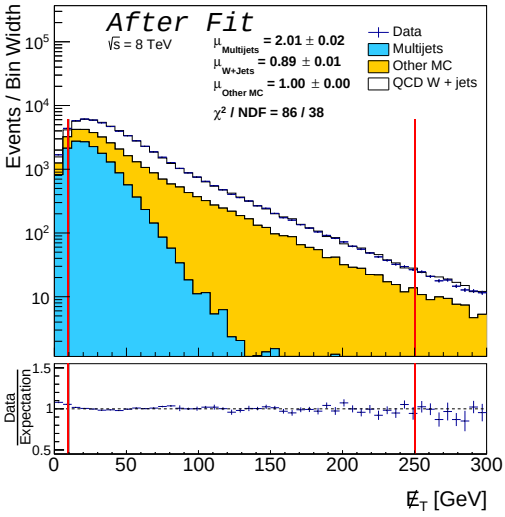

(a) inclusive W + jets multijet

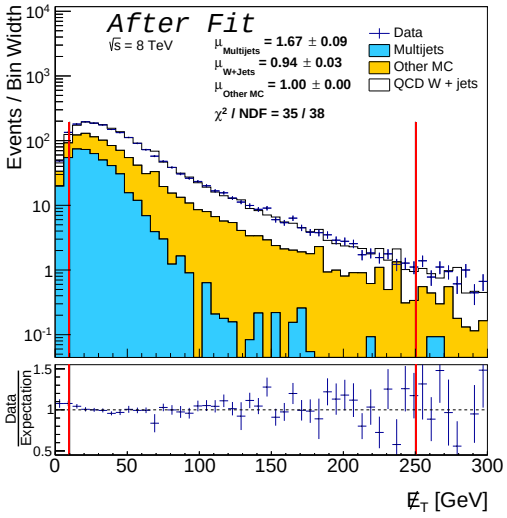

(b) VBF multijet selection

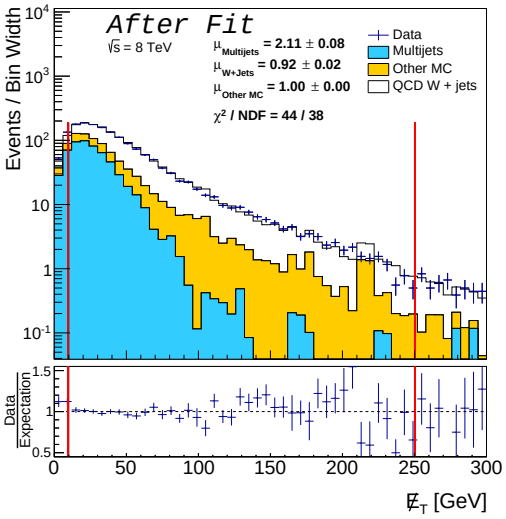

(c) QCD W + jets control region

Figure 8.5: $\not{E}_T$ distribution in the inclusive W + jets multijet and VBF multijet phase space, as well as in the multijet phase space for the W + jets control region for the electron channel. The multijet component (blue) and the QCD W + jets component (yellow) are scaled with the SF obtained from the fit, which are given on the plot. The data are shown as blue points with error bars corresponding to the statistical uncertainty. The fit range used is indicated by the red lines in the plots. The lower panel in the plot shows the comparison of the stacked signal and background components with the data. The signal is included in the *other MC* component, which is held constant in the fit.

8.3 Muon Channel

In the muon channel the dominant source of the multijet background are muons that originate from heavy flavour decays. As in the electron channel, a cut on the isolation variable $p_{\mathrm{T}}^{\mathrm{cone20}}/p_{\mathrm{T}}$ is applied by the low-p_{T} trigger and used in the signal selection. Therefore, the $p_{\mathrm{T}}^{\mathrm{cone20}}/p_{\mathrm{T}}$ variable is also used to define a template which models the multijet background. As discussed in section 7.2 the isolation cut for the signal was set to $p_{\mathrm{T}}^{\mathrm{cone20}}/p_{\mathrm{T}} = 0.05$, which has an efficiency of more than 95% for muons that have passed all other signal selection cuts. The remaining window $0.05 < p_{\mathrm{T}}^{\mathrm{cone20}}/p_{\mathrm{T}} < 0.12$ is used to select events for the multijet template. The trigger requirements and the quality cuts for the muon selection remain unchanged between the signal selection and the selection of the multijet template. The contamination of the template with real muons is shown in figure 8.6 for the VBF multijet selection (fig. 8.6(a)) and the VBF selection (fig. 8.6(b)). The contamination is found to be $\approx 25\%$ with a signal contamination of $\approx 2.5\%$ for the VBF selection and $\approx 8\%$ with a signal contamination of $< 1\%$ for the VBF multijet selection. The contamination in the inclusive W + jets and inclusive W + jets multijet selection are $\approx 37\%$ and $\approx 13\%$, respectively. In both cases the contamination with signal events is $< 0.5\%$. The normalisation of the multijet template is again determined with a fit in

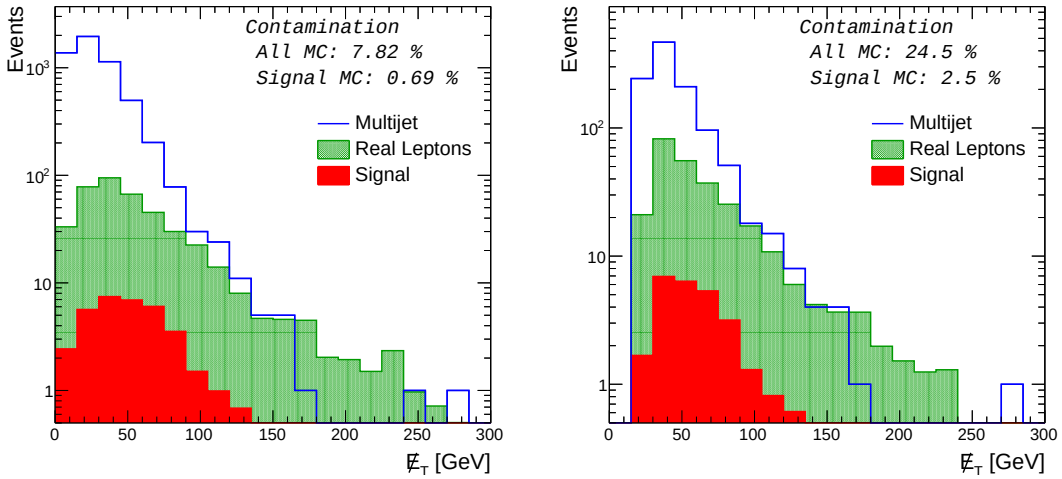

(a) VBF multijet selection

(b) VBF selection

Figure 8.6: Contamination of the multijet template with real muons as a function of $\not\!\!E_T$ for the VBF and the VBF multijet phase space. The blue curve shows the multijet template shape and the green curve the real muon prediction from MC normalised to the SM prediction. The amount of signal events from MC is made visible by the red curve. The predicted events containing real leptons are subtracted bin-by-bin from the multijet template, where resulting negative bins are set to zero.

each phase space. The results can be found in figure 8.7, where the extracted SFs for the multijet template and the QCD W + jets background can be found on the plots. The third component, containing the remaining backgrounds and the signal is held constant. The data are shown as the blue points, with error bars corresponding to the statistical uncertainty. The fit range used is indicated with the two red vertical lines on the plots.

The comparison of the sum of signal and background with the data (lower plot panel) shows good agreement in the VBF multijet phase space and the W + jets control region with a χ^2/NDF ratio close to 1. In the inclusive W + jets multijet phase space the high tail of the $\not\!\!E_T$ distribution shows a slight mis-modelling resulting in a high χ^2/NDF ratio ($\approx$ 10). Also the contamination with real leptons is higher in this phase space compared with the VBF multijet selection in the muon channel and the inclusive W + jets multijet selection in the electron channel. So probably the choice of the template is not optimal and can be improved with additional variations of the quality requirements of the muon selection. Nevertheless, a good modelling in the VBF phase space as well as in all other important distributions in the inclusive W + jets phase space is found as shown in chapter 7. Thus, it is decided to use the current template. Even though a large uncertainty of more than 30% is found on the normalisation of the multijet template (see sec. 9.5) the effect on the final cross section measurement is small. The SF for the QCD W + jets background is found to be in a $\pm$12% window around its SM prediction, which is covered by the expected range of uncertainty for this background. Based on the fit results the fraction of multijet events is found to be 11% in the inclusive W + jets phase space, 13% in the W + jets control region and 11% in the VBF phase space.

8.4 Discussion

After the detailed description of the multijet estimate in the two lepton channels, those results can be compared. Therefore the resulting SFs for the multijet template and the QCD W + jets background as well as the resulting multijet fraction in the different phase spaces are summarised in table 8.2. In both channels a similar approach is used, by using the window of the isolation variable $p_{\mathrm{T}}^{\mathrm{cone20}}/p_{\mathrm{T}}$ between the signal selection and the trigger cut to select events for the multijet template. This was initially studied in the electron channel and adopted to the muon channel, where it leads to sufficient results. Nevertheless, it was already mentioned that an improvement of the muon channel estimate can maybe be achieved by studying the effect of the muon quality requirements, as it was done in electron channel. The predicted multijet fraction in the muon channel is found to be larger than in the electron channel, but still agrees between them within their normalisation uncertainties, which are found to be 30% in both channels (see chapter 9 for details). The QCD W + jets SF are found to be < 1 and comparable between the lepton channels and the phase spaces. The shape of the multijet background as a function of $\not\!\!E_T$ and lepton p_{T} is found to differ between the two channels, as it can be seen in figure 7.6. In the muon channel more events at high $\not\!\!E_T$ and lower lepton p_{T} are selected. It was already mentioned that the dominant sources of the multijet background in both

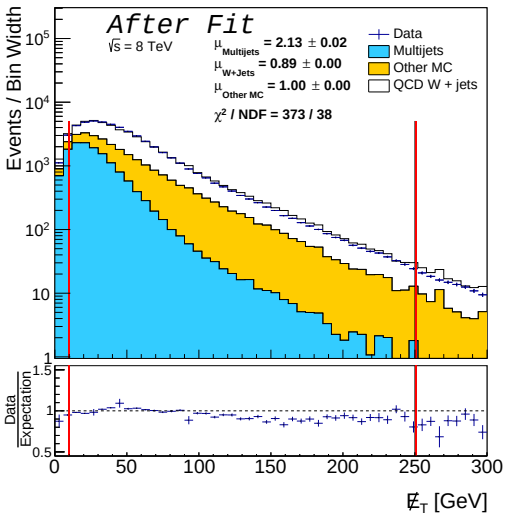

(a) inclusive W + jets multijet

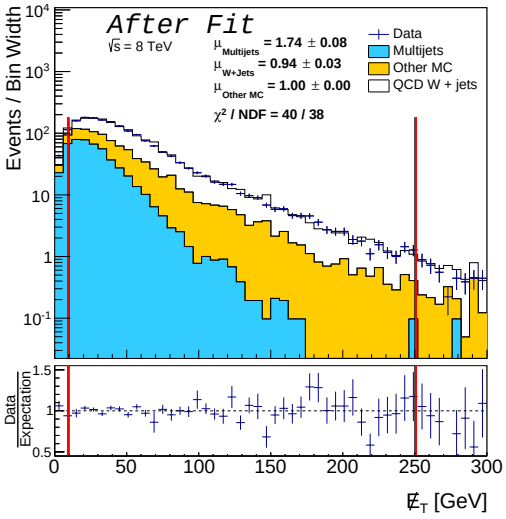

(b) VBF multijet selection

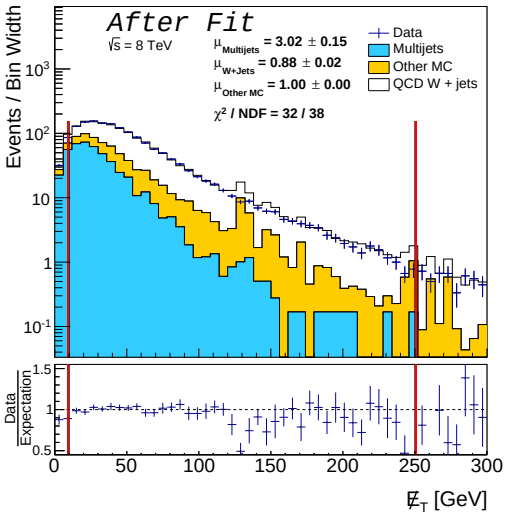

(c) QCD W + jets control region

Figure 8.7: $\not{E}_T$ distribution in the inclusive W + jets multijet and VBF multijet phase space, as well as in the multijet phase space for the W + jets control region for the muon channel. The multijet component (blue) and the QCD W + jets component (yellow) are scaled with the SF obtained in the fit and denoted on the plot. The data are shown as blue points with error bars corresponding to the statistical uncertainty. The fit range used is indicated by the red lines in the plots. The lower panel in the plot shows the comparison of the stacked signal and background components with the data. The signal is included in the *other MC* component, which is held constant in the fit.

Table 8.2: Summary of the results for the multijet estimate in the electron and muon channel. Given are the obtained SFs for the multijet template and the QCD W + jets backgrond from the fit in the inclusive W + jets multijet and VBF multijet phase space as well as in the multijet phase space for the W + jets control region. The quoted uncertainties reflect the statistical errors from the fit. In addition, the multijet fraction is given as the fraction of multijet events compared to the total signal and background prediction prediction.

	Electron Channel		
	Multijet SF	QCD W + jets SF	Multijet Fraction [%]
inclusive W + jets region	2.01 ± 0.02	0.89 ± 0.01	8.3
VBF region	1.67 ± 0.09	0.94 ± 0.03	6.8
W + jets control region	2.11 ± 0.08	0.92 ± 0.02	11.7
	Muon Channel		
	Multijet SF	QCD W + jets SF	Multijet Fraction [%]
inclusive W + jets region	2.13 ± 0.02	0.89 ± 0.00	11.0
VBF region	1.74 ± 0.08	0.94 ± 0.03	10.8
W + jets control region	3.02 ± 0.15	0.88 ± 0.02	13.0

channels are different, which can result in the given shape differences. However, the jet p_{T} and the M_{jj} distributions are similar in both channels as can be seen in figure 7.7 and figure 7.8. Those are the important distributions for the measurements and thus the effect from the shape difference in the multijet template between the electron and the muon channel are expected to be sub-dominant and covered by the shape uncertainties that are anyway evaluated separately in the two channels (see chapter 9 for details).

9 — Uncertainties

For the given analysis the uncertainties are categorised according to their sources. First to mention is the limited statistic in the simulated MC samples that are used for the signal and most of the backgrounds. Other sources of uncertainties, that are also related to the MC prediction, are referred to as *theoretical uncertainties*. This includes uncertainties corresponding to the renormalisation and the factorisation scale as well as the PDFs, the PS and the interference between the EW signal and the QCD W + jets background. These uncertainties are explained in detail in section 9.2. Further uncertainties are due to the measurements of the objects in the detector. These are explained in section 9.1 and are referred to as *experimental uncertainties*. Additional uncertainties that are taken into account are due to the data-driven multijet background (section 9.5) and the luminosity (section 9.4).

9.1 Experimental Uncertainties

The limited ability of the detector to measure the properties of the objects used in this analysis results in various uncertainties that are explained below.

9.1.1 Electron

The energy of the electron candidates measured in the EM calorimeter has to be corrected to match the initial electron energy. There is a certain energy loss due to the material upstream of the calorimeter as well as due to the finite length of the calorimeter and missed energy that is deposit in the cells neighbouring the cluster in η and ϕ. This calibration is obtained from a high statistics $Z \to ee$ MC sample and binned in η and p_{T} to optimise the correction for known detector variations and significant changes in the energy response. Each of the bins is optimised separately. Furthermore it was found that the energy resolution in data is worse than in the simulation, which requires an additional correction for the MC events to match their resolution with the one found in data. Also here various bins in η and p_{T} are considered independently. Different sources of uncertainties on the calibration and the resolution correction, as for example due to the passive material, have been taken into account and are combined into over all uncertainties, dependent on η and p_{T}, for the calibration and the resolution, respectively [99]. The effect of those uncertainties on the analysis are evaluated by scaling the p_{T} of the electron corresponding to the one standard deviation uncertainty of the energy scale or by smearing the energy by a random number taken from a Gaussian with a width of one standard deviation of the energy resolution. The second source of corrections and therefore an additional source of uncertainties for the analysis are the correction factors for MC according to reconstruction, identification and

the triggers efficiencies. They are determined by the *tag-and-probe* method using $Z \to ee$ events from collision data, where one electron has to fulfil stringent selection criteria and is defined as the *tag* electron. A second electron, that builds an invariant mass with the first electron close to the Z boson mass, is labelled as the *probe* electron and used for the measurement of the various efficiencies. The extracted scale factors are applied to the simulated events. Uncertainties on the SF are evaluated by e.g. varying the selection criteria of the *tag* electron, where the mean of all variations is taken as the nominal value and the root mean square (RMS) as the uncertainty [100]. The SFs are again determined in bins of η and p_{T}. The effect on the analysis is evaluated by varying the MC according to the 1σ shift of the SF.

9.1.2 Muon

Similarly to the electron channel, efficiency corrections for the MC simulated events are needed for the muon channel. The MC prediction is corrected with a SF that compared the measured efficiency for data with the one from MC. Both efficiencies, for trigger and for the reconstruction, are obtained with a tag-and-probe method similar to the one described for the electrons. The big advantage is, that there are two independent detectors available for the muon reconstruction (the MS and the ID). Therefore, the efficiency is measured as a conditional probability that a probe muon, that was already measured in the MS, is measured in the ID and vice versa. This is done using $Z \to \mu\mu$ events from data and from MC. The uncertainties on this efficiency arise e.g. from the data-driven background estimate that is used in the measurement. For the reconstruction efficiency no dependence of the SF on p_{T} was found and thus a binning of the SF is only taken into account in the $\eta - \phi$ region.

Scale and resolution corrections are applied to MC prediction to improve the data-MC comparison. They are again obtained from $Z \to \mu\mu$ events, as well as from $J/\Psi \to \mu\mu$ and $\Upsilon \to \mu\mu$ events in data, which where compared to high statistics samples from MC. Independent variations for the resolution of the ID and the MS are derived, while the scale variation is equal for both detector parts. These corrections are again binned in η and p_{T}. The uncertainties on the final measurement are evaluated in the the same manner as in the electron channel [59].

9.1.3 Jets

As for leptons, the measured energy of jets has to be corrected for detector effects, like dead material upstream of the hadronic calorimeter, or the limited radial length of the calorimeter, where very high energy jets reach already the edge of the calorimeter before they can deposit their whole energy. Furthermore, the effect of additional particles due to pile-up events has to be corrected. The calibration of the jet energy is done in two steps [101, 102]. The first correction is taken purely from MC where the reconstructed jet energy is matched to the energy of the jet at truth level. The same clustering algorithm as on reconstruction level forms jets at truth level, taking into account stable particles

from the simulation. In the second step smaller corrections are further derived from a data-driven method, so-called *in situ* method, where the p_{T} balance of a jet to either a hard object, like a Z boson, or an additional other jet is used. The in situ method further allows to constrain the uncertainties on the Jet Energy Scale (JES). All uncertainties of the JES calibration have been studied carefully and 65 different sources of (uncorrelated) uncertainties have been found. To not propagate them through the analysis individually all uncertainties that depend only on the p_{T} of the jets (57 in total) are combined into one large variation. These uncertainties include mainly systematic and statistical uncertainties on the in situ method itself and is further referred to as `JES`. All other uncertainties are treated separately. They are assumed to be uncorrelated, i.e. are added in quadrature. For all uncertainties related to JES, the effect on the final measurement is evaluated by shifting the energy of the jet by one standard deviation of the uncertainty before any cuts are applied. Uncertainties that depend on more parameters than just the p_{T} are treated separately and listed below.

JES - η Intercalibration The jet energy measurement in the forward region ($|\eta| > 0.8$) is validated separately, using the in situ method with dijet and Z + jet events as well as MC based methods. This introduces an additional uncertainty due to the modelling of the p_{T} balance in MC, referred to as η `intercalibration modelling`. This component is found to be the dominant uncertainty due to JES. Another uncertainty, further referred to as η `intercalibration stats and method`, summarizes all additional uncertainties that have to be considered from the method itself, as well as a component due to the limited statistics in the MC samples and highly pre-scaled trigger used for probing jets in the forward region.

JES - Pile-up The reconstructed jets have to be corrected for pile-up effects, which introduce additional uncertainties. There are two components, sensitive to the pile-up conditions in the data, taking into account the average number of proton-proton interactions per bunch crossing, μ, and the number of primary vertices, number of primary vertices (NPV). These corrections are named `NPV offset` and μ `offset`. For the dataset recorded in 2012 an improved pile-up subtraction, based on the pile-up energy density, ρ, was introduced [103]. Hereby, ρ is a measure of the pile-up activity in the event, which is further multiplied by the area of the jet. This gives a more precise estimate of the amount of pile-up in the jet cone and allows an improved correction of the four-momentum of the jet. This method has two additional uncertainties, named `pile-up` p_{T} and `pile-up` ρ `topology`, which are treated separately from the two other pile-up components mentioned above.

JES - Flavour-based The in situ method to derive corrections for the JES uses samples with a particular fraction of events initiated by quarks and gluons. It was found that the response for jets originating from quarks or gluons is different. In most analysis the fraction of those jets is unknown, and therefore an uncertainty is introduced, known as `flavour composition`. Another uncertainty takes into account the difference in the

response between PYTHIA and HERWIG PS for gluon jets. This is further referred to as `flavour response`.

Jet Energy Resolution As for the calibration of the jet energy, the resolution is determined using a MC based technique and an in situ technique from data using the p_{T}-balance method, as described above. In the MC based technique the resolution is directly calculated by comparing the reconstruction level jet to the matched truth level jet. In the in situ method the reconstruction level p_{T} and the truth level p_{T} are divided by the p_{T} of the reference (balance) jet and then subtracted in quadrature from each other. This corrects for the inherent non-zero resolution at truth level. The derived Jet Energy Resolution (JER) is used to smear the jet energy in MC to match the one found in data. The different sources of the uncertainties on the JER are added to one over all uncertainty, simply referred to as `JER`, that is propagated through the analysis. An important role plays again the modelling of the jet p_{T} in the MC simulation, which is tested by using different MC predictions. Other sources of uncertainties are similar to the ones considered for the JES. The effect of the JER on the final measurement is evaluated by smearing the jet energy by a random number taken from a Gaussian with a width of one standard deviation of the JER.

Jet Vertex Fraction The JVF cut, that is used to reject jets originating from pile-up, as discussed in section 7.3, introduces an additional uncertainty. The cut value for the JVF cut is varied according to its efficiency changing by $\pm 1\sigma$. The variations are derived from an in situ method based on Z + jets events and are binned in p_{T} and η as the efficiency is found to change with p_{T} and η.

9.1.4 Missing Transverse Momentum

The $\not{E}_T$ is calculated from all objects in the events and therefore the uncertainty on $\not{E}_T$ is due to the uncertainties of the other objects. Most of these uncertainties are already taken care of in the above mentioned uncertainties, such that in the dedicated $\not{E}_T$ uncertainty only objects that are not treated separately in the analysis are taken into account. Those objects are referred to as *soft terms* and their uncertainty on the momentum scale and the resolution is derived in a similar way as for the hard objects, from Z boson and W boson events. Those uncertainties are propagated into the $\not{E}_T$ calculation and result in two uncertainty components, namely `MET_ResoSoftTerms` and `MET_ScaleSoftTerms`.

9.2 Theoretical Uncertainties

The uncertainties explained in this section are mainly due to limited ability to describe a proton-proton interaction including the production and decay of particles. This includes the PDFs as the basis of the interaction, as well as the renormalisation and factorisation

scale as additional assumptions on the hard process. Further uncertainties that are described are due to different models of the parton shower and the interference between the EW signal and the QCD W + jets background. The detailed evaluation of the theoretical uncertainties is only done for the EW signal and the QCD W + jets background. For all other backgrounds, predicted by MC, the effects due to those variations on the analysis are expected to be small, especially from shape variations in the tail of the M_{jj} distribution. Therefore, for all other MC backgrounds, apart from the top pair background, only an overall normalization uncertainty on each background is considered, which have already been given in chapter 6 as the uncertainty on the cross section.

9.2.1 Renormalisation and Factorisation Scale

The choice of the renormalisation scale, μ_R, and the factorisation scale μ_F is more or less arbitrary. For the EW signal and the QCD W + jets background sample they are chosen as the W boson mass. To evaluate the uncertainty, both scales are varied by a factor of 2 and 0.5 alone and also together at the same time. As the change of the scales affects only the truth level of the generated events, there is no need to fully reconstruct all samples with the varied scales. The reconstructed events of the signal and QCD W + jets background samples are reweighted according to their truth M_{jj}, with the reweighting function obtained by a linear fit from the ratio of the nominal sample and the varied ones. The reweighted events are further passed through the cross section measurement to evaluate the effect of the scale variation, where the largest shift in the fit of all variations is symmetrised and used as the uncertainty. Figure 9.1 shows the ratio of the different varied samples and the nominal sample for the EW signal and the QCD W + jets background at truth level.

For the EW signal, fig. 9.1(a), the change due to the variation of the renormalisation and the factorisation scale is small and even in the high M_{jj} tail not larger than 10% whereas for the QCD W + jets background, fig. 9.1(b), a large change up to $\approx 40\%$ is found. The error bars on the plots are due to statistics of the MC samples. As the variations are only derived by a reweighting of the nominal prediction, the samples are not statistically independent.

9.2.2 Parton Shower

The default PS for the EW signal and the QCD W + jets background is simulated with Pythia 8. The same events have been showered with Herwig to account for effects of the different shower simulations. As these events are only available at truth level, a reweighting has to be performed to derive an uncertainty at reconstruction level. The ratio between the events showered with Pythia and with Herwig at truth level can be seen in figure 9.2. The error bars are due to the statistical uncertainty of the MC prediction and are found to be rather large in the high M_{jj} tail. For the QCD W + jets background as well as for the EW signal the effect from the different shower simulations is found to be

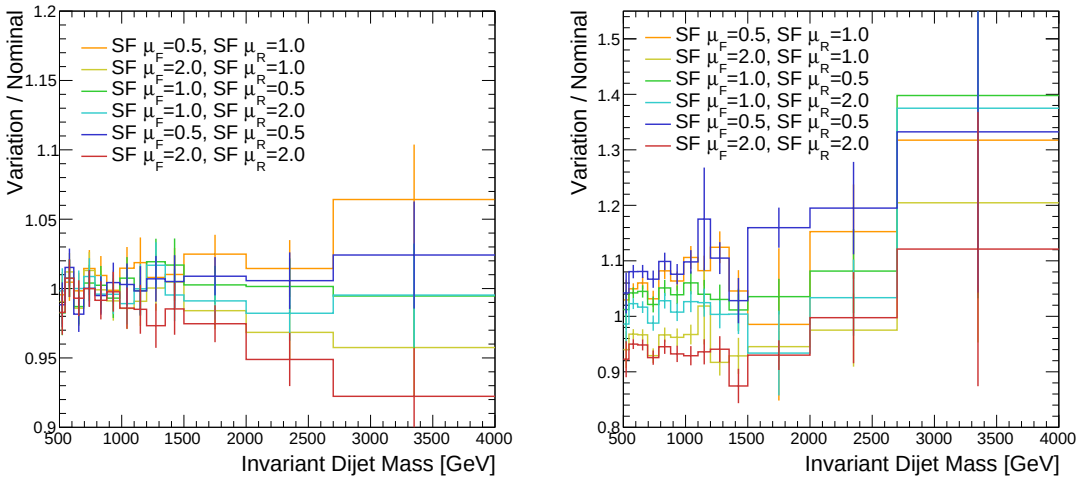

(a) EW Signal

(b) QCD W + jets Background

Figure 9.1: Ratio of different scale varied samples and the nominal sample for the EW signal (left) and the QCD W + jets background (right) as a funtion of M_{jj} at truth level. The error bars are due to the statistical uncertainty of the MC prediction. The variations are derived from a reweighting of the nominal sample and thus the samples are not to statistically independent.

small. However, the ratio is fitted with a linear function, which is further used to reweight the events from the showering with Pythia.

9.2.3 Interference

It is stated in section 2.8 that, in order to derive the ME for the cross section calculation all Feynman diagrams that contribute to a given process are added up. As the ME is squared, mixed terms occur that contain contributions from several Feynman diagrams and therefore the cross section is not proportional to the sum of the "squared" Feynman diagrams but to the square of the sum. Those mixed terms are referred to as interference and can increase or decrease the cross section of a process. Depending on the increase of the cross section, the interference is called positive or negative. Interference effects occur between all Feynman diagrams that have the same initial and final state. As already mentioned the electroweak t-channel signal and the diboson background have the same initial and final state with the same number of electroweak vertices (see figure 2.5) and therefore they interfer. The size of the interference can be tested by comparing the sum of the EW t-channel and s-channel processes to a combined generation that includes the interference. This study has been performed [104] and a negligible interference was found between those processes, when the mass of the dijet system is required to be well above the mass of the W and Z boson. The two jets in the final state of the s-channel process are

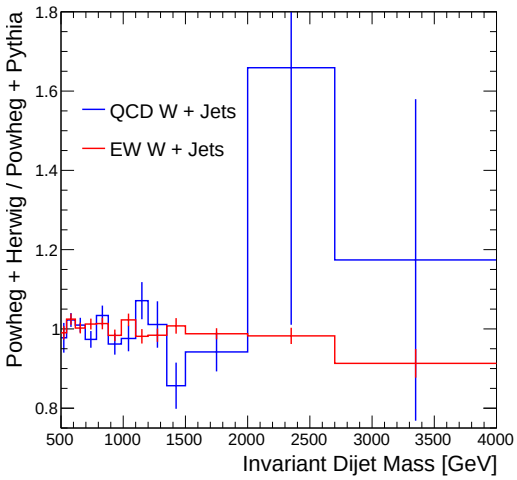

Figure 9.2: Ratio of events showered with HERWIG and with PYTHIA for the EW signal and the QCD W + jets background at truth level. The error bars are due to the statistical uncertainty of the MC prediction.

coming from a boson (see figure 2.5(d)), thus their invariant mass is close to the boson mass and therefore small compared to the dijet mass of the VBF process. By requiring large M_{jj} the s-channel component is suppressed and it is possible to treat the two processes independently.

Besides the diboson background, also the QCD W + jets background can have the same particles in the inital and the final state as the EW signal and thus interference effects have to be considered as well. This is again done by comparing the sum of the individual generated processes to the combined simulation which includes the interference. For technical reasons this sample includes the diboson component, which is found to be $\approx 1\%$. For the study of the interference the diboson component is included in the EW signal, thus the signal sample is not the same as the one used for the analysis. Figure 9.3 shows the comparison of the (independently generated) EW signal (including the diboson component) and the combined production where the QCD W + jets background was manually subtracted using an independently generated sample. The error bars reflect the statistical uncertainty of the generated samples. It can be seen that the interference is larger in the low M_{jj} region, which is expected as the QCD W + jets background has a lower M_{jj} on average. The interference is about $5 - 10\%$ of the signal and leads to an increase of the cross section. The size of the interference reveals that this component can not be neglected in the analysis. Per definition the interference is part of the signal and the background at the same time. As in this comparison the diboson component can not be separated from the signal, it was decided to account for the interference effect as a correction to the QCD W + jets background. The same comparison as above for the interference and the EW signal is made for the interference and the QCD W + jets background. Therefore, the EW component was subtracted from the interference sample, such that is consists only of the

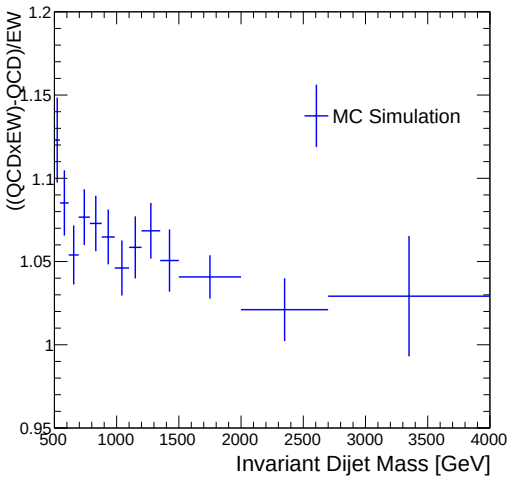

Figure 9.3: Ratio between the (independently generated) EW signal (including the diboson component) and the EW signal that contains also the interference of the signal with the QCD W + jets background at truth level. For the latter both processes have been generated together such that the generation includes the interference and the (standalone) QCD W + jets background is subtracted.

QCD W + jets background and the interference contribution. Those are compared to the QCD W + jets background without interference. The ratio as a function of M_{jj} is shown in figure 9.4. The error bars again refer to the statistical uncertainty of the two samples. Figure 9.4 shows again the increase of the cross section due to the interference component. Because the QCD W + jets background drops faster in M_{jj}, compared to the EW signal, less events are left in the high-M_{jj} tail and thus the interference has a larger fraction in the sum of the QCD W + jets background and the interference. A linear fit to the ratio is performed and used as a reweighting function for the QCD W + jets background at reconstruction level. The reweighting is performed event-by-event corresponding to the truth M_{jj} of the event. The reweighted sample is passed through the analysis to extract the effect of the interference on the cross section measurement.

9.2.4 PDF

The PDF used in this analysis for the EW signal and the QCD W + jets background generated with Powheg is the CT10 PDF. To determine an uncertainty on the choice of the PDF 26 sets of eigenvectors are provided, each with an up and down variation that reflect the uncertainty at 90 % confidence level. These variations are provided as a shift in the event weight for the reconstructed events. Therefore 52 different reweightings are performed and passed through the analysis. The shifts in the extracted signal strength according to the 26 PDF sets are combined into one overall up and one down variation, where all shifts in the positive direction are added up in quadrature and so also all shifts

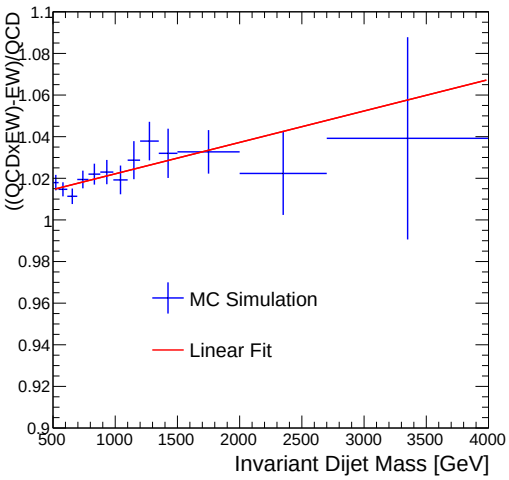

Figure 9.4: Ratio between the (independently generated) QCD W + jets background and the QCD W + jets background that contains also the interference of the QCD W + jets background with the EW signal at truth level. For the latter both processes have been generated together such that the generation includes the interference and the (standalone) EW signal (including the diboson component) is subtracted.

in negative direction. If both variations of one eigenvector set result in a shift in the same direction, only the larger shift is added in quadrature. In addition to the 26 eigenvectors the CT10 PDF group provides also uncertainties due to the value of the strong coupling constant $\alpha_s = 0.118$. Therefore the signal extraction is re-done with $\alpha_s = 0.117$ and $\alpha_s = 0.119$. This does not correspond to the 1σ error of $\alpha_s = 0.118$, which is ± 0.0012 [7]. The final shift due to the α_s variation is modified by the factor $\frac{1}{0.82389}$ to reflect the $1\,\sigma$ error.

9.3 Signal Modelling

The cross section measurement of the EW signal is performed by a fit to the M_{jj} distribution. This fit is sensitive to the modelling of the signal shape and thus an alternative prediction of the signal is tested to account for an uncertainty on the signal shape. An additional signal sample is generated with Sherpa at LO (see section 6.1) and is tested in the analysis. Figure 9.5 shows ratio of the two MC predictions as a function of the M_{jj} distribution at reconstruction level. The LO generation from Sherpa predicts on average a lower M_{jj} of the two tagging jets. As the M_{jj} distribution is mainly driven by the angle between the jets, this means the jets in Sherpa are more often closer to each other. This implies that the jets have a higher p_{T} on average, as a higher momentum leads to the jets being more central and therefore closer to each other. The difference in

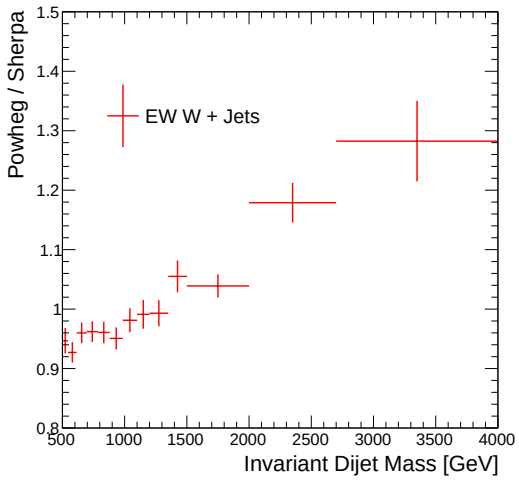

Figure 9.5: Ratio of the EW signal prediction from POWHEG at NLO and SHERPA at LO as a function of the M_{jj} distribution at reconstruction level. The error bars reflect the statistical uncertainties of the two predictions.

the leading jet p_T distribution between POWHEG and SHERPA will be discussed in more detail in section 11.1, when the limit setting for the anomalous couplings is explained. Nevertheless, for the cross section measurement the MC prediction is used to account for differences in the modelling of the M_{jj} distribution.

9.4 Luminosity Uncertainty

The integrated luminosity is determined with the LUCID detector and the so-called "van der Meer" scans with ATLAS, that are described in detail in [105]. The overall concept is to scan the profile of one beam with the other one on the two axis in the transverse plane to use this information for the luminosity calculation. The final uncertainty on the luminosity calculation is 1.9% [106].

9.5 Uncertainties on Multijet Background

In the following, an estimate on the uncertainty on the data-driven multijet background is described. All possible sources of uncertainties in the data-driven technique, like the fit range and fit variable that are used, are probed and result in an overall normalisation uncertainty on the multijet background, that will be propagated to the cross section measurement. Furthermore, additional templates that are defined in each channel to test the template choice, are considered separately in the final measurement as a shape uncertainty. In section 9.5.1 the different sources of uncertainties, that are further taken into account,

are described before the effect on the electron and muon channel and a final summary will be shown in section 9.5.2

9.5.1 General Procedure

The estimate of the multijet background is done consistently between the two lepton channels where it was possible. Therefore, the same fit range and fit variable was chosen and the variations for determining the uncertainties are made common. There are only small differences in the nominal template choice due to different triggers in the two channels, but also here the variations are done as similar as possible. For all variations described below the change in the multijet fraction in the VBF phase space is used to estimate an uncertainty.

Fit Range and Fit Variable The nominal fit for the determination of the multijet SF is performed in the $\not{E}_T$ distribution in the range between $10 - 250$ GeV. This fit range was varied in two different ways ($0 - 150$ GeV and $20 - 300$ GeV) and the fit was re-done to evaluate the change in the multijet fraction in the VBF phase space. Furthermore the m_T variable is chosen as an alternative fit variable, using the range $5 - 150$ GeV. These two variations result in two separate uncertainties on the multijet normalisation. The alternative fit variable is taken as one uncertainty, while the largest shift due to the fit range variation is taken as the other uncertainty. Both are symmetrised and treated as uncorrelated.

Template Choice The choice of the standard template for the multijet estimate is in both lepton channels constrained by the lowest unprescaled trigger for the given dataset. This does not allow to vary the isolation window much by keeping enough statistics in the template. Nevertheless, small changes in the isolation window have been performed to study the effect on the multijet fraction. In the electron channel the isolation window was varied from $0.05 < p_T^{\text{cone20}}/p_T < 0.09$ to $0.04 < p_T^{\text{cone20}}/p_T < 0.07$ and to $0.06 < p_T^{\text{cone20}}/p_T < 0.1$. The window can not be extended above $p_T^{\text{cone20}}/p_T = 0.1$ because of the trigger cut. As it can be seen in the red curve in figure 8.2, there are still some events left above $p_T^{\text{cone20}}/p_T = 0.1$ as the trigger isolation uses the uncalibrated p_T of the lepton, while the isolation variable in the analysis uses the corrected one. Nevertheless, events with $p_T^{\text{cone20}}/p_T > 0.1$ should not be used as they introduce a bias e.g. in the ϕ distribution of the electron. In the muon channel a similar variation of the isolation window was performed. It was changed from $0.05 < p_T^{\text{cone20}}/p_T < 0.12$ to $0.05 < p_T^{\text{cone20}}/p_T < 0.1$ and to $0.7 < p_T^{\text{cone20}}/p_T < 0.12$. Also here the window is restricted due to the trigger cut at $p_T^{\text{cone20}}/p_T = 0.12$. To perform a more conservative estimate on the uncertainty of the multijet background a completely different approach for the template definition is used on both channels by inverting the $|\frac{d_0}{\sigma_{d_0}}|$ cut ($|\frac{d_0}{\sigma_{d_0}}| > 3$). In this case the isolation cut is kept the same as for the signal selection ($p_T^{\text{cone20}}/p_T < 0.05$ in both lepton channels). The variation that gives the largest shift, either in positive or negative direction is symmetrised and taken as the uncertainty due to the template choice.

Experimental Uncertainties In addition to the effect due to the properties of the fit itself, like the fit range and the fit variable, the impact from the experimental uncertainties on the multijet fraction is also considered. Therefore, all MC backgrounds and the signal are shifted at the same time corresponding to (one of) the experimental uncertainties, as described in section 9.1. The multijet fit is performed for each of the variations and again the change in the multijet fraction in the VBF phase space is taken as the uncertainty. The resulting uncertainty on the multijet normalisation is determined by adding the components in quadrature. All shifts predicting less multijet fraction in the VBF phase space are added in quadrature and so also all shifts that predict more multijet fraction. As for the PDF eigenvectors, only the larger variation is considered, if both shifts of one uncertainty go in the same direction. The larger of the two sums is symmetrised and taken as the final overall experimental uncertainty.

Background Modelling The multijet fit is sensitive to the modelling of the QCD W + jets background, as it is the largest background and it is allowed to float in the fit. Therefore, an additional uncertainty is introduced that should cover the effect of the modelling of the QCD W + jets background by using an alternative background prediction. As for the rest of the analysis this is done using the additional Sherpa sample. This change in the multijet fraction in the VBF phase space is again symmetrised and taken as an uncertainty on the normalisation.

9.5.2 Results

The variations of the multijet fraction due to the experimental uncertainties are given in table 9.1 for the electron channel and in table 9.2 for the muon channel, respectively.

In both cases the larger shift is found for the upward fluctuation and thus the final experimental uncertainty is $\pm 6.4\%$. The uncertainties due to variations of the fit range, the fit variable and the template choice as well as the background modelling are given in table 9.3 and table 9.4 for the electron and muon channel, respectively. In the electron channel the largest effect on the multijet fraction was found from the variation of the fit variable (-21.6%) and the fit range variation (-14.4%), while in the muon channel the shift of the isolation window gave the largest uncertainty (-25.2%), followed by the alternative fit variable (-12.4%). The final uncertainty on the normalisation of the multijet estimate is determined by adding the largest shift from the fit range variation and the template choice in quadrature with the background modelling, the fit variable variation and the symmetrised experimental uncertainty. The remaining numbers are shown in table 9.5. For both channels the total uncertainty is $\approx 30\%$.

Table 9.1: Fractional uncertainties on the multijet background due to experimental systematics in the electron channel for the VBF phase space. The multijet fit in the VBF multijet phase space is repeated for each systematic uncertainty and the change in the multijet fraction in the VBF phase space is taken as the uncertainty. The up (down) components are added in quadrature to one overall up (down) variation.

Systematic	Deviation (%)	
JER	+6.0	
	down	up
JES	-2.4	1.8
JES η intercalib. model.	0.0	0.0
JES η intercalib. stat. and method	0.6	0.6
JES μ offset	0.0	0.0
JES NPV offset	0.0	0.0
JES pile-up p_{T}	0.0	-0.6
JES pile-up ρ	-0.6	0.6
JES flavor composition	-1.2	0.6
JES flavor response	0.6	-1.2
JVF	0.0	0.0
$\not{E}_T$ resolution soft terms	0.0	0.0
$\not{E}_T$ scale soft terms	0.0	0.0
Ele energy smearing	0.0	0.0
Ele energy scaling	0.0	0.0
Ele trigger SF	0.0	0.0
Ele tight SF	-0.6	0.6
Ele reco SF	0.0	0.0
Uncertainty on multijet fraction	−3.1%	+6.4%

Table 9.2: Fractional uncertainties on the multijet background due to experimental systematics in the muon channel for the VBF phase space. The multijet fit in the VBF multijet phase space is repeated for each systematic uncertainty and the change in the multijet fraction in the VBF phase space is taken as the uncertainty. The up (down) components are added in quadrature to one overall up (down) variation.

Systematic	Deviation (%)	
JER	+5.6	
	down	up
JES	-2.3	0.6
JES η intercalib. model.	0.0	2.8
JES η intercalib. stat. and method	-0.6	-0.6
JES μ offset	-1.1	-0.6
JES NPV offset	-0.6	0.6
JES pile-up p_{T}	-0.6	-1.1
JES pile-up ρ	-0.6	-0.6
JES flavor composition	-1.1	-1.1
JES flavor response	-1.1	0.6
JVF	-0.6	-0.6
$\not{E}_T$ resolution soft terms	-0.6	-0.6
$\not{E}_T$ scale soft terms	0.0	-0.6
Muon trigger	0.6	-1.1
Muon efficiency	0.0	-0.6
Muon momentum scale	-0.6	-0.6
Muon momentum res ID	-0.6	-0.6
Muon momentum res MS	-0.6	-0.6
Uncertainty on multijet fraction	-3.8%	$+6.4\%$

Table 9.3: Results of fits for the multijet fraction in the electron channel. The considered uncertainties are due to the fit range, the fit variable and additional template, as well as for an alternative QCD W + jets background sample. The uncertainties for the SFs correspond to the statistical uncertainty from the fit.

Configuration	Multijets SF	QCD W SF	multijet frac. (%)	Deviation (%)
Nominal	1.67 ± 0.09	0.94 ± 0.03	6.8	-
$\not\!\!E_T$ $0 - 150$ GeV	1.77 ± 0.08	0.92 ± 0.03	7.2	+6.0
$\not\!\!E_T$ $20 - 300$ GeV	1.43 ± 0.13	0.99 ± 0.03	5.8	−14.4
m_T $5 - 150$ GeV	1.31 ± 0.06	1.05 ± 0.02	5.4	−21.6
d_0 template	2.42 ± 0.13	0.86 ± 0.03	6.2	−8.5
iso window down	2.29 ± 0.12	0.94 ± 0.03	6.5	−4.5
iso window up	1.78 ± 0.09	0.93 ± 0.03	7.1	+3.9
QCD W model.	1.49 ± 0.09	0.97 ± 0.03	6.1	−10.8

Table 9.4: Results of fits for the multijet fraction in the muon channel. The considered uncertainties are due to the fit range, the fit variable and additional template, as well as for an alternative QCD W + jets background sample. The uncertainties for the SFs correspond to the statistical uncertainty from the fit.

Configuration	Multijets SF	QCD W SF	multijet frac. (%)	Deviation (%)
Nominal	1.74 ± 0.08	0.94 ± 0.03	10.9	-
$\not\!\!E_T$ $0 - 150$ GeV	1.71 ± 0.07	0.94 ± 0.03	10.7	−1.1
$\not\!\!E_T$ $20 - 300$ GeV	1.68 ± 0.13	0.95 ± 0.03	10.4	−4.0
m_T $5 - 150$ GeV	1.55 ± 0.05	0.99 ± 0.02	9.5	−12.4
d_0 template	1.67 ± 0.08	0.87 ± 0.03	10.5	−3.6
iso window up	2.39 ± 0.17	0.95 ± 0.03	9.9	−8.6
iso window down	2.80 ± 0.13	0.95 ± 0.02	8.1	−25.2
QCD W model.	1.62 ± 0.09	0.96 ± 0.03	9.9	−8.5

Table 9.5: Total uncertainty on multijet background for both lepton channels

	electron	muon
Fit range	14.4%	4.0%
Fit variable	21.6%	12.4%
Template choice	8.5%	25.2%
Experimental	6.4%	6.4%
Bkg modelling	10.8%	8.5%
Total	30.1%	30.3%

10 — Cross Section Measurement

In this chapter the extraction of the signal strength is described, which is used to determine the cross section of the EW W + jets process. The basic principles of the performed fit are described in section 10.1, followed by an explanation of the handling of the uncertainties in section 10.2, while the results of the measurement are presented in section 10.3.

10.1 Procedure

The strength of the signal is extracted by a fit to the M_{jj} distribution in the VBF phase space, as this provides a good separation of the signal and the backgrounds in general but especially for the QCD W + jets background. The probability to measure n events when a certain number of events, λ, is expected, is given by the Poisson distribution:

$$f(n, \lambda) = \frac{\lambda^n}{n!} e^{-\lambda} \tag{10.1}$$

In the measurement n is the number of selected collision data in each bin of the M_{jj} distribution and λ is the sum of predicted signal and background events per bin. The prediction is divided into three components, one is the EW signal, one is the QCD W + jets background and the last component is the sum of all the remaining backgrounds. In the fit the normalisation of the EW signal and the QCD W + jets background is allowed to float, while the other backgrounds are fixed to their SM values. The number of signal and QCD W + jets background events, N_{ew} and N_{qcd}, is optimised in a way that the probability for the observed data n is maximal. This is tested for all bins at the same time by building the likelihood function, which is a product of the Poisson distributions of all bins i:

$$L(N_{ew}, N_{qcd}) = \prod_{i=1}^{\text{bins}} \frac{N_i^{n_i}}{n_i!} e^{-N_i} \tag{10.2}$$

where $N_i = N_{ew,i} + N_{qcd,i} + N_{\text{other bkg},i}$. As it is more convenient to deal with a sum rather than a product, the natural logarithm of the likelihood, $\ln(L)$, is used instead of the likelihood itself, which transfers the product to a sum. The maximum of the likelihood L is found at the same position as the maximum of $\ln(L)$ as the natural logarithm is a monotonous function. For practical reasons not $\ln(L)$ is maximised, but $-\ln(L)$ is minimised.
The SFs as the final result for the EW signal and the QCD W + jets background, are defined as the ratio of the obtained values and the SM values predicted by MC:

$$\mu_{ew} = \frac{N_{ew,\,\text{fit}}}{N_{ew,\,\text{SM}}} \qquad \text{and} \qquad \mu_{qcd} = \frac{N_{qcd,\,\text{fit}}}{N_{qcd,\,\text{SM}}} \tag{10.3}$$

The fit is performed simultaneously in the electron and muon channel, where μ_{ew} and μ_{qcd} have to be equal in both fits. Unless otherwise stated, in the following the fits are always for the combination of both channels.

10.2 Handling of Uncertainties in the Fit

Before the final results are obtained, the handling of the uncertainties in the fits will be explained in detail. The different sources of experimental and theoretical uncertainties have already been discussed in chapter 9. All uncertainties are handled in a similar way in the fits by making use of pseudo data templates. These templates are build by adding up the EW signal, the QCD W + jets background and the other backgrounds, which are shifted according to the uncertainty that is tested. This pseudo data template replaces the data template in the fit and is further fitted with the nominal (i.e. unshifted) templates for the EW signal, the QCD W + jets background and the other backgrounds. This allows to account for shape as well as for normalisation differences for the uncertainty.

Experimental and theoretical Uncertainties For the experimental uncertainties the signal and all MC backgrounds are varied at the same time and added up for the pseudo data template. The fit is performed by fitting the nominal templates for signal and background to the pseudo data template. For the theory uncertainties the procedure is the same, the shift according to the PDFs, the scale choices and the PS are assumed to be correlated for the EW signal and the QCD W + jets background and therefore the shifts for both are tested at the same time.
As already mentioned, for most of the other MC backgrounds only a theoretical uncertainty on the normalisation is taken into account. Each of those are tested with a separate pseudo data template. Only for the top pair background an additional sample is used to derive a shape uncertainty.

Multijet Background For the multijet background the normalisation uncertainty, that has been evaluated in section 9.5, as well as a shape uncertainty is taken into account. The latter is derived by propagating the additional templates, that have also been defined in section 9.5, through the fit.

Interference For the interference between the EW signal and the QCD W + jets background, discussed in section 9.2.3, the pseudo data template is build with the reweighted QCD W + jets sample.

Signal and Background Modelling The modelling of EW signal as well as the QCD W + jets background have been tested with the additional samples from Sherpa with the pseudo data fits. The modelling of the QCD W + jets background is improved with the reweighting derived from the W + jets control region (see sec. 7.6). The reweighting

function has been varied with respect to the uncertainties of its parameters and finally the function that results in the largest uncertainty is used.

Statistical Uncertainty In addition to the above mentioned uncertainties, the uncertainty due to the limited statistics of the signal and background templates is evaluated. This uncertainty is uncorrelated between the bins of a histogram. The bin contents of the nominal templates are varied independently from each other according to a Poisson distribution with the mean of the distribution being the nominal bin content. This is done in separate fits for the signal, the QCD W + jets background and the other backgrounds and always repeated 1000 times. The width of the resulting distribution for μ_{ew} and μ_{qcd} is taken as the uncertainty.

Luminosity The effect of the luminosity uncertainty is tested by normalising all MC samples for the pseudo data template to the shifted luminosity.

10.3 Fit Results

The resulting scale factors of the fit are shown in table 10.1 for the combination of the two lepton channels, as well as for the two lepton channels separately as a cross check. The quoted uncertainties for μ_{ew} and μ_{qcd} are the statistical uncertainties from the fit.

Table 10.1: Results for μ_{ew} and μ_{qcd} for the fit in the electron and the muon channel as well as for the combined fit. The quoted uncertainties are the statistical uncertainties from the fit. The NDF are the number of bins in the M_{jj} distribution with the parameters of the fit subtracted.

channel	μ_{ew}	μ_{qcd}	χ^2/NDF
electron	0.87 ± 0.05	1.03 ± 0.02	22/11
muon	0.82 ± 0.05	1.03 ± 0.02	49/11
combined	0.85 ± 0.04	1.03 ± 0.01	72/24

The scale factor for the EW signal is found to be consistent between the electron and the muon channel within the statistical uncertainty of the fit. The EW signal is scaled down by at least 13% in all three fits while the SF for the QCD W + jets background is nearly consistent with 1 within the uncertainty. The goodness of the fit is tested by calculating the χ^2 of the distributions. This is divided by the degrees of freedom, which are the number of bins, with the free parameters of the fit subtracted. For the combined fit, the ratio is $\chi^2/\text{NDF} = 3$. The χ^2 takes only the statistical and not the systematic uncertainty into account. Figure 10.1 shows the M_{jj} distribution in the electron and muon channel separately. The SFs for the EW signal and the QCD W + jets background that are derived from the combined fit, have been applied. The data are shown as black points

with error bars corresponding to the statistical uncertainty. Some deviations between the

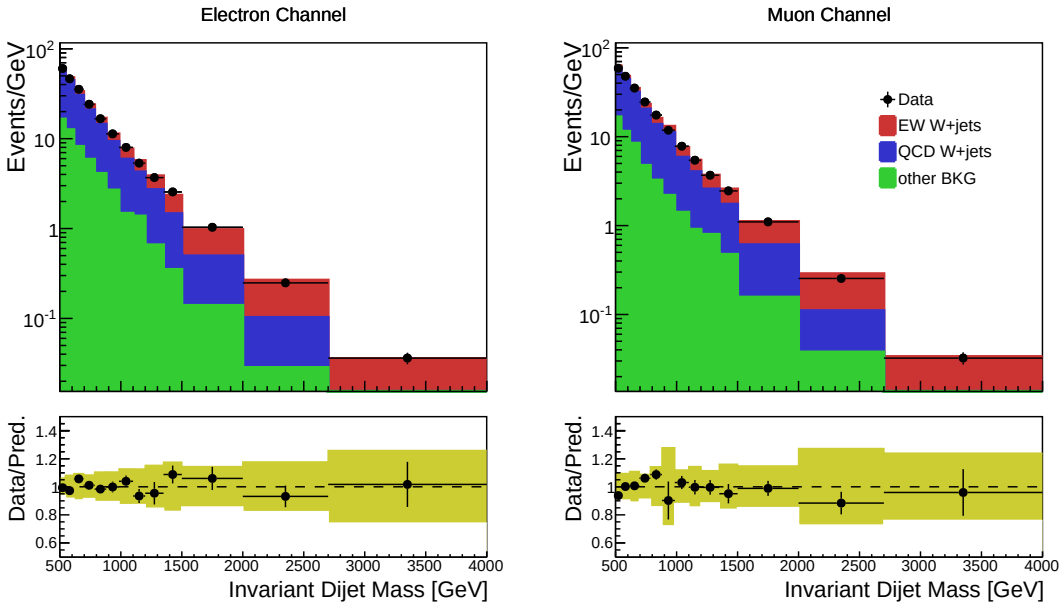

Figure 10.1: M_{jj} distribution for the electron (left) and the muon channel (right) after the SFs for the EW signal and the QCD W + jets background from the combined fit have been applied. The data are shown as black points with error bars corresponding to their statistical uncertainty. The yellow band in the ratio panel shows to the quadratic sum of the statistical and the systematical uncertainty of the prediction.

data and the prediction are found, especially in the low M_{jj} region. The yellow band in the ratio panel reflects the quadratic sum of the statistical and systematic uncertainty on the prediction, which is found to cover all deviations. In the high M_{jj} region, where the signal is the dominant component, an overall good modelling is found.

Table 10.2 gives the numbers for the EW signal and QCD W + jets background as well as the sum of the other backgrounds and the data where two-three bins of the M_{jj} distribution in figure 10.1 have been combined. The uncertainties on the processes refer to the statistical uncertainty. For the total prediction the statistical as well as the systematic uncertainties are given[1].

Table 10.3 shows the uncertainties obtained from the fit in the combined channel. For each uncertainty that has an up and down variation, the larger of the two components is used as a symmetric uncertainty.

[1]These numbers point out that the fifth bin in the M_{jj} distribution for the muon channel, where a large uncertainty was found, is due to a large statistical uncertainty of the QCD W + jets background. This comes most probably from an event with a large event weight.

Table 10.2: Event numbers for the SM prediction and the data in various bins of M_{jj} in the VBF phase space. The quoted uncertainties on the signal and the background predictions are statistical. Systematic uncertainties are given for the total SM prediction.

	Electron		
M_{jj} range [GeV]	500-695	695-880	880-1100
EW signal	626 ± 5	489 ± 9	410 ± 7
QCD W + jets	5837 ± 40	2344 ± 24	1209 ± 16
other BKG	2283 ± 73	922 ± 36	452 ± 31
Sum SM	8746 ± 83 (stat.) ± 1191 (syst.)	3755 ± 45 (stat.) $\pm$ 497 (syst.)	2071 ± 35 (stat.) $\pm$ 343 (syst.)
Data	8788	3752	2104
M_{jj} range [GeV]	1100-1350	1350-2000	2000-4000
EW signal	316 ± 7	371 ± 3	150 ± 2
QCD W + jets	598 ± 41	346 ± 30	59 ± 4
other BKG	237 ± 18	122 ± 12	24 ± 5
Sum SM	$1151 \pm$ 46(stat.) $\pm$ 476(syst.)	$839 \pm$ 33 (stat.) $\pm$ 353(syst.)	233 ± 7 (stat.) $\pm$ 68 (syst.)
Data	1087	899	221
	Muon		
M_{jj} range [GeV]	500-695	695-880	880-1100
EW signal	635 ± 6	458 ± 4	402 ± 5
QCD W + jets	6083 ± 66	2412 ± 30	1451 ± 202
other BKG	2234 ± 83	737 ± 39	393 ± 29
Sum SM	8952 ± 106(stat.) ± 1497(syst.)	3607 ± 49 (stat.) ± 598 (syst.)	2246 ± 204(stat.) ± 598(syst.)
Data	8802	3867	2138
M_{jj} range [GeV]	1100-1350	1350-2000	2000-4000
EW signal	307 ± 3	377 ± 5	160 ± 7
QCD W + jets	582 ± 14	417 ± 18	54 ± 5
other BKG	211 ± 18	150 ± 20	31 ± 7
Sum SM	1100 ± 23(stat.) ± 193(syst.)	$944 \pm$ 27(stat.) ± 231(syst.)	245 ± 11(stat.) $\pm$ 83(syst.)
Data	1095	918	220

Table 10.3: Uncertainties on μ_{ew}

Systematic	Uncertainty (%)
Signal Statistics	±2.5
Background Statistics	±2.7
Interference	±1.3
PDF CT10	±8.2
α_s	±0.4
Scale	±8.3
Shower	±7.0
Signal modelling	±8.7
QCD W + jets modelling	±9.1
JER	±6.0
JES	±2.9
JES η intercalibration model	±7.2
JES η intercalibration stat. and method	±1.4
JES μ offset	±0.9
JES NPV offset	±0.7
JES pileup p_{T}	±0.3
JES pileup ρ	±1.3
JES flavor composition	±4.1
JES flavor response	±4.3
JVF	±0.2
$\not{E}_T$ resolution soft terms	±0.3
$\not{E}_T$ scale soft terms	±0.1
Electron energy smearing	±0.1
Electron energy scaling	±0.2
Electron trigger SF	±0.2
Electron tight SF	±0.5
Electron reco SF	±0.2
Muon trigger	±0.7
Muon efficiency	±0.2
Muon momentum scale	±0.1
Muon momentum res ID	±0.1
Muon momentum res MS	±0.1
Diboson normalisation	±0.0
EW Z+jets normalisation	±0.1
Single top normalisation	±0.0
QCD $Z(\rightarrow ee/\mu\mu/\tau\tau)$ normalisation	±0.1
Top pair normalisation	±0.3
Top pair modelling	±4.0
Multijets normalisation	±0.9
Multijets modelling	±2.6
Luminosity	±1.8
Uncertainty	±22.8%

The dominant systematic uncertainty is due to the alternative QCD W + jets background sample, generated with SHERPA, resulting in an uncertainty of 9.1% on μ_{ew}. It has already been discussed that this samples does not describe the data very well in section 7.6 and that a reweighting was derived from the W + jets control region, to improve the modelling and reduce the uncertainty due to the SHERPA prediction. Without the reweighting from the W + jets control region the uncertainty on the final measurement due to the alternative background sample was found to be $> 20\%$. Other important uncertainty sources are the alternative EW sample from SHERPA, the PDF and scale variations as well as the experimental uncertainties due to the jet energy scale and jet energy resolution. The uncertainties in table 10.3 can be treated as uncorrelated and therefore can be added in quadrature to an overall systematic uncertainty on μ_{ew}, which is found to be $\pm 22.8\%$.
The measured signal strength can be converted into a fiducial cross section σ_{fid}:

$$\sigma_{\text{fid}} = \sigma_{\text{total, gen.}} \cdot A \cdot \mu_{\text{ew}} \tag{10.4}$$

where $\sigma_{\text{total,gen.}}$ is the cross section for the EW $W+$ jets production in a generator phase space, i.e. with only very loose cuts on the p_{T} of the objects applied at truth level, which are needed for the generation. This cross section is predicted with POWHEG at NLO in QCD. Furthermore, A denotes the acceptance from the generator phase space to the fiducial phase space of the measurement. This number is determined at truth level from the EW signal samples generated with POWHEG. The signal is generated separately for the W^+ and the W^- channel and therefore two acceptance values are calculated, which are equal for the electron and the muon channel. This is expected, as they are obtained from truth level, where no differences in the reconstruction and identification of the two lepton flavours exist. The acceptances are found to be $A_{W^+} = 0.061$ and $A_{W^-} = 0.052$. The statistical uncertainty on the acceptance is $< 1\%$ and is neglected in the following. No systematic uncertainty can be estimated as no sample with the same cuts or even looser cuts on generator level is available. The fact that the acceptance for W^+ is larger than for W^- can be explained by the kinematics of the signal process: The incoming quark that radiates the W^+ is more likely a valence quark, that, on average carries a larger momentum fraction. Those events have a higher probability to survive the selection criteria, especially the stringent jet p_{T} cuts, of the event selection.

Taking into account the acceptances and the cross sections from the generation, which are 2110.0 fb for W^+ and 1337.8 fb for W^-, the resulting fiducial cross section for the EW W + jets process is:

$$\sigma_{\text{fid}} = 337.1 \pm 15.8(\text{stat.}) \pm 76.9(\text{syst.}) \pm 6.1(\text{lumi}) \text{ fb} \tag{10.5}$$

This can be compared with the theoretical prediction determined with POWHEG, where the selection criteria for the fiducial phase space have already been applied at truth level. This is found to be $395 \pm 4(\text{scales}) \pm 17(\text{shower})$ fb. It can be concluded that the measured fiducial cross section agrees within the uncertainties with the theoretical prediction. The dominant uncertainties on the measured cross section arise from the theory prediction of the EW signal and the QCD W + jets background. The two largest components are due to the modelling of of signal and background probed with additional samples generated with SHERPA at LO in QCD.

11 — Limits on Anomalous Triple Gauge Couplings

In addition to the measurement of the cross section of the EW W + jets process, the coupling at the three boson vertex $WWZ/WW\gamma$ is tested. This is done by using the anomalous couplings approach, described in detail in section 2.7.3, with the corresponding effective Lagrangian given in equation 2.32. Limits are set at 95% confidence level on the CP conserving parameters g_1^Z, κ_Z and $\lambda_{Z/\gamma}$ as well as on the CP violating parameters $\tilde{\kappa}_Z$ and $\tilde{\lambda}_{Z/\gamma}$, which are tested in the LEP scenario (see sec. 2.7.3). The obtained limits are converted into limits in the EFT approach. One dimensional limits are set, where only one parameter is varied and the others are held constant at their SM values. In addition two dimensional limits are set, where the limits are calculated as a linear combination of two of the CP conserving parameters. As already discussed in section 2.7.3, the limits are set with a form factor of $\Lambda_{FF} = 4$ TeV and $\Lambda_{FF} = 100$ TeV, where the latter basically reflects a limit setting without a form factor, $\Lambda_{FF} = \infty$. The EW process is a t-channel process where the momentum of the two jets is directly related to the coupling at the three boson vertex via the mandelstam variable t. Therefore, the p_{T} of the leading jet is chosen as the sensitive variable to probe the couplings. As discussed in section 7.7, the cut on M_{jj} is tightened to 1 TeV to increase the purity of the EW process and therefore also the sensitivity for the coupling variations. The optimal cut on the leading jet p_{T} distribution is further found in an optimisation study where the expected limits are compared for various cuts on leading jet p_{T}. This is discussed in detail in section 11.4. The (technical) details of the MC prediction with varied couplings are given in section 11.1. Furthermore, it is found that many of the SM background samples do not contain enough statistics in the tail of the leading jet p_{T} distribution, such that an extrapolation is performed to extract reliable background numbers for the limit setting (section 11.2). In section 11.3 and section 11.5 the limit setting procedure and the uncertainties, that are taken into account, are discussed. In section 11.6 the results of the limit setting for the anomalous couplings approach and in section 11.7 for the EFT approach are discussed. Finally, in section 11.8 the obtained limits are compared to results from previous experiments.

11.1 Parameterisation of the Coupling Variation

The Sherpa generator has the ability to generate events with varied couplings in the ME and also to simulate the PS on those events with the built-in PS generator. A large number of events is generated with Sherpa 1.4.5 at truth level to parameterise the change in the number of predicted events due to the variation of the three boson coupling. In most samples only one parameter is varied, but a few samples are generated with the variation of two parameters to account for correlations that are needed for the two-dimensional limit

setting. A table that contains all available samples is given in appendix B.
The limit setting itself is based on the comparison to data and thus the predictions for the varied parameters are needed at reconstruction level. The number of predicted events at reconstruction level, $N_{\text{reco,aTGC}}$, is calculated in the following way:

$$N_{\text{reco,aTGC}} = \text{XS} \cdot a \cdot \mathcal{L}_{\text{int}} \cdot c_{\frac{r}{t}} \cdot k \tag{11.1}$$

The different components are defined as:

- cross section (XS): The cross section that refers to each of the individual samples, that are generated with SHERPA at truth level. The XS includes the main information about the change of the prediction as a function of the parameter variation. This will be explained in more detail below.
- a: Denotes the detector acceptance at truth level. It is defined as the number of events in the fiducial phase space (at truth level) divided by the total number of events (in the generated sample). Only minimal cuts, like loose p_{T} cuts on the partons, are applied during the generation and thus the other cuts, that define the phase space for the measurement, have to be applied after the generation at truth level.
- $\mathcal{L}_{\text{int}}$: Integrated luminosity that corresponds to the recorded data.
- $c_{\frac{r}{t}}$: The efficiency for selected events at truth level, t, to get reconstructed, r. This number is taken from the POWHEG samples that contains both, reconstruction level and truth level events. Details are given below.
- k: The XS measurement uses the EW signal sample from POWHEG, because it can calculate the ME at NLO in QCD. Unfortunately, POWHEG cannot vary the couplings and thus the variations are generated with SHERPA. As the variations of the couplings are a pure EW effect it can be separated from the QCD corrections taken from POWHEG and therefore a correction factor is introduced, that corrects the SHERPA samples to match the NLO QCD prediction from POWHEG. Also here more details are given below.

Cross section and acceptance The change of the cross section has a quadratic dependence on the parameter variation, as can be seen in figure 11.1, for the parameters Δg_1^Z and $\lambda_{Z/\gamma}$ with $\Lambda_{FF} = \infty$. The blue points are the cross sections of various generated samples each with a different value for the parameters in the range from -1 to 1. The errors on the blue points reflect the statistical uncertainty from the generation. As expected the change of the couplings leads, in most cases, to an increase of the XS. For $\lambda_{Z/\gamma}$ the parabola is symmetric around its SM value $\lambda_{Z/\gamma} = 0$. It can be seen in figure 11.1(a) that the SM value does not reflect the minimum of the parabola for Δg_1^Z as negative interference effects can lead to a reduction of the cross section for some variations. In both cases the generated points are fitted with a quadratic function that is shown as the red curve, which perfectly fits all generated points. Therefore, the generation of two extreme values,

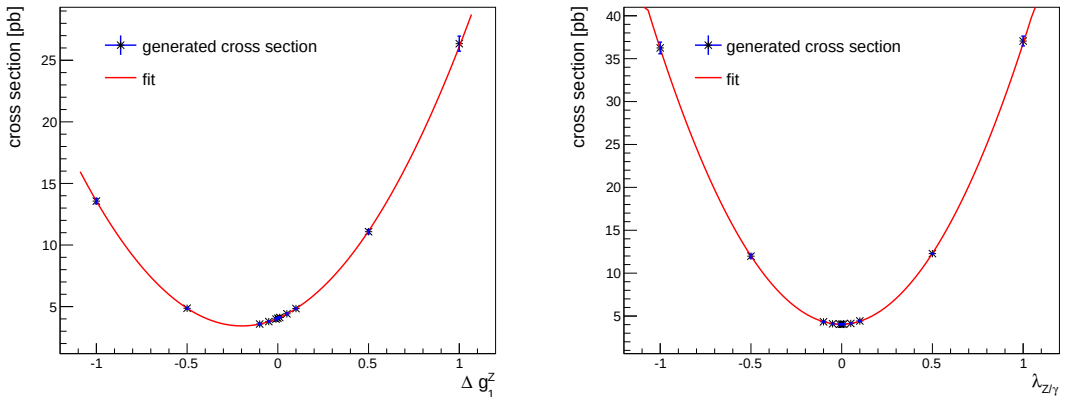

(a) Δg_1^Z (b) $\lambda_{Z/\gamma}$

Figure 11.1: The blue points show the generated cross section for $\Lambda_{FF} = \infty$ for various variations of Δg_1^Z and $\lambda_{Z/\gamma}$ with statistical errors from the generation. The red curve is a quadratic fit through the generated points.

like ± 1, for each parameter together with the SM prediction as a third point, would be sufficient to parameterise the dependence of the cross section on the TGC parameters. This has to be done separately for each TGC parameter for both tested form factors. The comparison between the generated cross section and the fitted parabola was tested for all five parameters for $\Lambda_{FF} = \infty$[1]. Although the parabolas can look different for the five parameters, the same good agreement between the generated and the interpolated cross sections, as seen above, is found for all parameters.
The limit setting is based on the assumption that not only the XS but also the number of predicted events at reconstruction level has a quadratic dependence on the coupling parameters. In equation 11.1 only the term XS $\cdot\, a$ is taken from the samples with the varied couplings. All other elements are treated independently from the variations and are equal for all generated samples. Not only the XS changes when varying one of the parameters, but also the kinematics and therefore the distributions are different for the various samples. Figure 11.2 shows the normalised leading jet p_{T} distribution for different values of $\lambda_{Z/\gamma}$ for $\Lambda_{FF} = \infty$ at truth level. The error bars reflect the statistical uncertainty of the samples. There is no difference in the shape between the SM value $\lambda_{Z/\gamma} = 0$ and the variation $\lambda_{Z/\gamma} = 0.01$. But once going higher with $\lambda_{Z/\gamma}$ the differences become significant. Already for $\lambda_{Z/\gamma} = 0.1$ the spectrum is found to be harder than for the SM case and gets even harder for $\lambda_{Z/\gamma} = 1$, which is the largest variation that is tested. For most parameters this is already much larger than the expected limits. The influence of the acceptance is tested using a similar approach as in figure 11.1. This time not only

[1]The following study for the acceptance is only possible for $\Lambda_{FF} = \infty$ as for $\Lambda_{FF} = 4$ TeV only the extreme values at ± 1 are generated for all five parameters. But as the change in the cross section for each parameter, and therefore also the change in the kinematic distributions, is larger for $\Lambda_{FF} = \infty$ the effect due to the acceptance is also assumed to be larger. Thus the estimated acceptance uncertainty for$\Lambda_{FF} = \infty$ should also cover the effect at $\Lambda_{FF} = 4$ TeV.

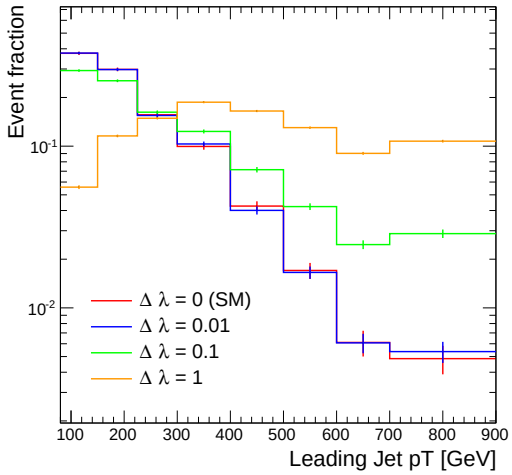

Figure 11.2: Comparison of the (normalised) p_{T} distributions of the leading jet with different variations of the parameter $\lambda_{Z/\gamma}$ for $\Lambda_{FF} = \infty$ at truth level. The error bars on the distribution reflect the statistical uncertainty of the samples.

the cross section is tested, but the product XS $\cdot\, a$. Each generated cross section in figure 11.1 (blue points) is multiplied with the acceptance derived from the corresponding file at truth level. In addition a parabola is calculated taking into account three values of XS $\cdot\, a$ from $\Delta g_1^Z = \pm 1$ and the SM value at $\Delta g_1^Z = 0$. The product XS $\cdot\, a$ from the generated points does not agree with this parabola, as it can be seen in figure 11.3. This figure shows the generated values of XS $\cdot\, a$ as blue points with error bars that reflect the statistical uncertainty due to the generated cross section and the acceptance, as well as the calculated parabola in pink. The x-axis shows only the innermost generated points at $\Delta g_1^Z = -0.1, -0.05, -0.01, 0, 0.01, 0.05, 0.1$, to better see the deviations. Because the point at $\Delta g_1^Z = 0$ is used to calculate the parabola it agrees by definition with the pink curve. The other generated points do not agree with the calculated parabola. The difference between the generated values of XS $\cdot\, a$ and the interpolated parabola have to be considered in the limit setting by introducing an additional uncertainty referred to as *acceptance uncertainty*. To derive the size of this uncertainty, the same comparison as for Δg_1^Z is done for the other four parameters, $\lambda_{Z/\gamma}$, κ_Z, $\tilde{\lambda}_{Z/\gamma}$, $\tilde{\kappa}_Z$, for $\Lambda_{FF} = \infty$. The deviation between the generated and the interpolated points, as a fraction of the generated values are shown in figure 11.4. The five parameters are each tested at eight intermediate working points, namely $\pm 0.01, \pm 0.05, \pm 0.1$ and ± 0.5, which gives in total 40 comparisons between generated and interpolated values. Unfortunately, $\tilde{\lambda}_{Z/\gamma} = 0.01$ had problems in the generation and was excluded, thus only 39 data points are shown in figure 11.4. The calculated points are found to be widely distributed in a region $\pm 50\%$ around the generated values with a small preference for being larger than the generated points. However, no distinct behaviour for the single parameters is found. Therefore, the RMS (0.137 as seen in figure 11.4) of all points is taken as an uncertainty on the signal due to the

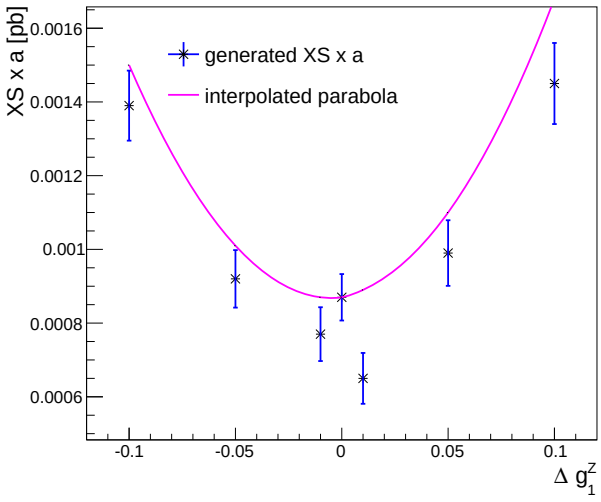

Figure 11.3: The blue points show the product XS $\cdot a$ from generated samples for various values of Δg_1^Z with statistical errors from the generation. The pink curve is a quadratic function calculated from the three points $\Delta g_1^Z = -1, 0, +1$.

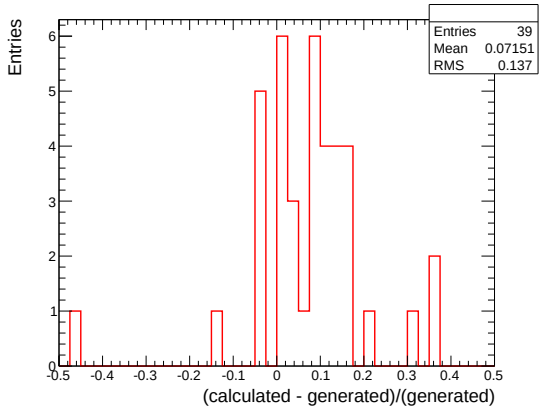

Figure 11.4: Deviation between the 39 generated and the corresponding calculated values for the product XS $\cdot a$ at $\Lambda_{FF} = \infty$. In total five parameters are tested each at eight intermediate points between the extreme values at ± 1 and 0.

acceptance. As already explained, this study is only done for $\Lambda_{FF} = \infty$ and the resulting uncertainty is adopted for $\Lambda_{FF} = 4$ TeV.

NLO QCD Correction As already mentioned, it would be preferred to use POWHEG for the simulation of the EW W + jets with varied couplings, as it provides the ME calculation at NLO in QCD. As it is not possible to vary the couplings in the generation from POWHEG, SHERPA is used. It has already been discussed in section 9.3 that in the M_{jj} shape between the POWHEG prediction and the prediction from SHERPA differences due to the ME generation and the PS are found, and that SHERPA on average predicts a lower invariant mass of the two tagging jets. This effect is now studied for the leading jet p_T. Figure 11.5 shows the leading jet p_T distribution at truth level in the high-M_{jj} phase space for the EW signal processes, generated with SHERPA in blue and with POWHEG in red. All TGC parameters are set to their SM values in SHERPA, such that the generation is

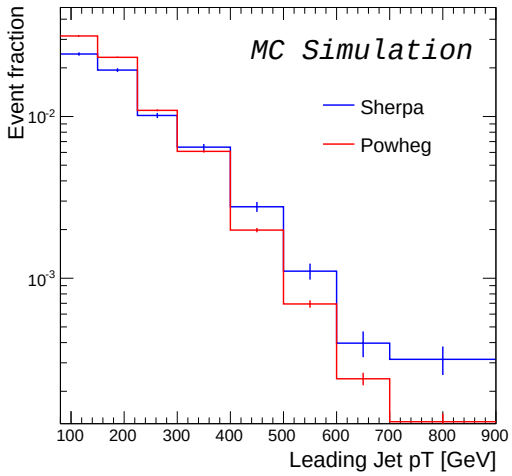

Figure 11.5: Comparison of the leading jet p_T distribution for the EW W + jets processes generated with POWHEG at NLO in QCD and SHERPA at LO in QCD in the high-M_{jj} phase space. The error bars reflect the statistical uncertainty on the samples.

comparable with POWHEG. It can be seen that SHERPA predicts a much harder spectrum for the jet p_T compared to POWHEG. This explains the smaller M_{jj} values in the LO generation, as softer jets are more forward in the VBF production. A correction factor k is extracted from the ratio of both generations, to match the SHERPA prediction to the NLO prediction from POWHEG. This correction factor is further applied to all SHERPA samples with variations of the couplings. It is assumed that the NLO/LO correction does not change with the variation of the couplings as the former is based on the QCD part of the generation and the latter on the electroweak one. As figure 11.5 shows, the correction factor k has a large dependence on the leading jet p_T. In the high-M_{jj} phase space with the nominal cut at leading jet $p_T > 80$ GeV it is found to be $k = 1.15 \pm 0.02$, whereas once

going higher in jet p_{T} the correction changes significantly. For a leading jet $p_{\mathrm{T}} > 600$ GeV the resulting factor is $k = 0.53 \pm 0.08$. The quoted uncertainties in both cases are due to the statistics of the SHERPA sample. The statistical uncertainty on the POWHEG sample is not considered here as this is already taken into account in the reconstruction level uncertainty.

Reconstruction Level Efficiency Up to now, all event numbers and corrections are derived at truth level. The SHERPA samples with the varied TGC parameters are not available at reconstruction level and therefore the corresponding event numbers at reconstruction level are calculated by multiplying the truth level number with the efficiency for truth level events to be selected at reconstruction level. The EW W + jets sample generated with POWHEG contains events at truth as well as at reconstruction level and is therefore used to determine the efficiency $c_{\frac{r}{t}} = n_{\text{fiducial, reco}}/n_{\text{fiducial, truth}}$. The same kinematic cuts are applied independently at truth and at reconstruction level and it is found that the majority of events are included in the numerator and the denominator[2]. Only a small fraction ($\approx 13\%$) of events appear only at reconstruction level. It can happen that events which fail the truth level selection undergo corrections at reconstruction level, e.g. p_{T} shifts of the objects due to JES corrections, and smear into the fiducial phase space at reconstruction level. The numerator and the denominator are not statistically independent as they are selected from the same events. To determine the statistical uncertainty on the efficiency the ratio has to be split into three independent samples:

- events that appear only at truth level: t
- events that appear only at reconstruction level: r
- events that fulfil both selections: b

The efficiency can be written as $c_{\frac{r}{t}} = \frac{b+r}{b+t}$. The uncertainty on b, t and r is calculated as the binomial uncertainty, by taking into account the total number of generated events in the sample. These uncertainties can be propagated to an uncertainty on $c_{\frac{r}{t}}$. As the efficiencies for the electron and the muon channel are not equal, they are determined independently from each other. The corresponding values (for the phase space with leading jet $p_{\mathrm{T}} > 600$ GeV) are 0.70 ± 0.06 and 0.62 ± 0.05 for the electron and muon channel, respectively.

11.2 Background Extrapolation

The EW W + jets signal sample and the QCD W + jets background sample have enough statistics to model the tail of the leading jet p_{T} distribution. All other backgrounds from MC and also the multijet template are limited in statistics and thus an extrapolation is

[2] To be more precise: With this definition $c_{\frac{r}{t}}$ is not really an efficiency, as the numerator is not a subset of the denominator.

needed to get an estimate of the predicted events. Certain backgrounds are grouped together to enhance the statistics in order to fit the leading jet p_{T} distribution with different numerical functions. Robust fits for the backgrounds are only possible if the events from the electron and the muon channel are combined. The remaining five groups of backgrounds are: the multijet background, where the data-driven templates for the electron and the muon channel are added up. In contrast to the lepton p_{T} distribution, which was found to be very different between the two channels (see sec. 8), the leading jet p_{T} distribution is quite similar (see fig. 7.7), thus it was decided to group them together. There is one group of background containing the top-quark-pair production, and another background describing the production of single top quarks. The three processes, WW, WZ and ZZ are added together to the *diboson* background and finally the remaining backgrounds, QCD and EW Z + jets production, summed to the last contribution, referred to as *other*. Several functions for the fit were tested and the following two functions are found to reflect the shape of the leading jet p_{T} distribution:

$$f_1(p_{\mathrm{T}}) = a \cdot e^{-b \cdot p_{\mathrm{T}}} \tag{11.2}$$

$$f_2(p_{\mathrm{T}}) = \frac{a}{(p_{\mathrm{T}} + b)^c} \tag{11.3}$$

Both fits describe the tail of the p_{T} distribution, as shown in figure 11.6 for the top-quark-pair production in figure 11.6(a) and the single top background in figure 11.6(b), which are the two dominant components. The plots with the fits for the other backgrounds can be found in figure C.1 and figure C.2 in appendix C. For all backgrounds the largest possible

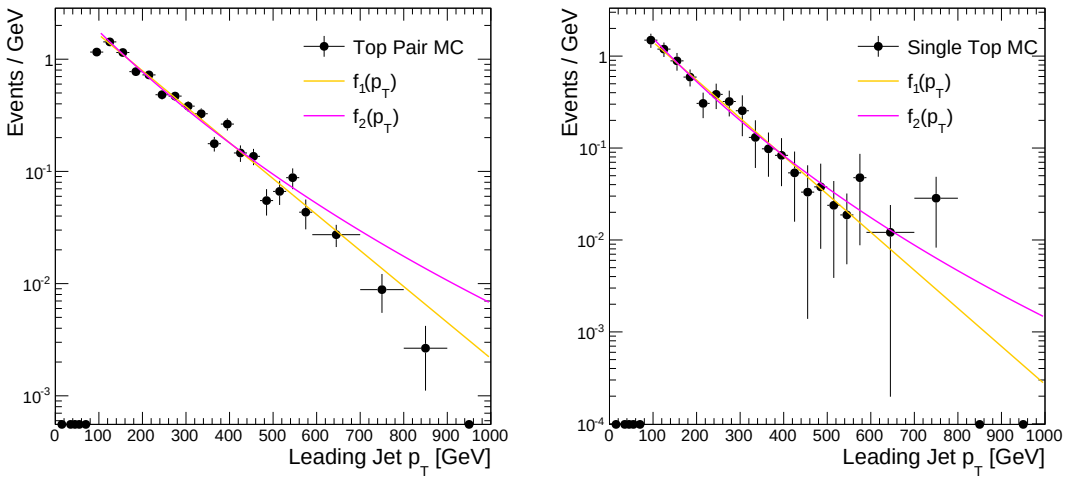

(a) Top quark pair background

(b) Single top quark backgrounds

Figure 11.6: Extrapolation of the leading jet p_{T} distribution for the top-quark pair and the single top production with two different numerical functions. The error bars reflect the statistical uncertainties on the MC prediction.

fit range is fitted and the predicted number of events is extracted by integrating over

the fit function up to 10000 GeV, which basically reflects ∞. The results for the two fit functions for the various backgrounds are summarized in table 11.1. The predicted event

Table 11.1: Results for background extrapolation in the phase space with leading jet $p_{\mathrm{T}} >$ 600 GeV. Each group of backgrounds is fitted separately in the given range with two different functions. The quality of the fit is tested by calculating the χ^2 for each distribution in the fit range. The NDF are the number of bins with the free parameters of the fit subtracted.

	Fit Range [GeV]	$f_1(p_{\mathrm{T}}) = a \cdot e^{-b \cdot p_{\mathrm{T}}}$		$f_2(p_{\mathrm{T}}) = \frac{a}{(p_{\mathrm{T}}+b)^c}$	
		χ^2/NDF	prediction	χ^2/NDF	prediction
Top Pair	110-590	31/14	5.6	33/13	10.1
Single Top	110-590	5/14	1.3	5/13	2.74
Diboson	110-470	12/10	0.5	12/9	0.9
Multijet	110-500	76/11	0.1	68/10	0.3
Other	110-590	18/14	0.8	22/13	1.7

numbers are exemplary shown for the region with leading jet $p_{\mathrm{T}} > 600$ GeV. The ratio of χ^2/NDF is always equal or slightly better for $f_1(p_{\mathrm{T}})$ as it is for $f_2(p_{\mathrm{T}})$, therefore $f_1(p_{\mathrm{T}})$ is used as the default fit function with its predicted event numbers being the central values. It can also be seen in table 11.1 that the predicted event numbers for the fit with $f_2(p_{\mathrm{T}})$ are always about a factor of 2 larger than the nominal ones. A conservative approach is therefore used and a 100% error is assumed on the nominal values.

11.3 Limit Setting

The limit setting is performed with the TGCLIM package that was developed by the EW working group in the ATLAS collaboration [107]. The description of the limit setting below follows the TGCLIM manual and reference [108]. A frequentist limit calculation is used to extract the 95% confidence level (CL) for the TGC parameters. This is done in a cut and count experiment and therefore the description of the limit setting procedure is only done for this case.

Constructing the negative log likelihood function As for the cross section measurement, the negative log likelihood function is constructed. The probability to observe N_{data} when a certain number of signal events, N_{sig}, and a certain number of background events, N_{bkg} is predicted, is given by the Poisson distribution:

$$P(N_{\mathrm{data}}, N_{\mathrm{sig}} + N_{\mathrm{bkg}}) = \frac{(N_{\mathrm{sig}} + N_{\mathrm{bkg}})^{N_{\mathrm{data}}}}{N_{\mathrm{data}}!} e^{-(N_{\mathrm{sig}}+N_{\mathrm{bkg}})} \tag{11.4}$$

This time all uncertainties (see chapter 9 and section 11.5) are directly considered in the fit for the limit setting: As N_{sig} and N_{bkg} are not perfectly known, their true value can be found within the uncertainty:

$$N_{\text{sig, true}} = N_{\text{sig}}(1 + \theta_s) \tag{11.5}$$

$$N_{\text{bkg, true}} = N_{\text{bkg}}(1 + \theta_b) \tag{11.6}$$

where $\boldsymbol{\theta}$ denotes a matrix containing the fractional uncertainties on the signal and the background. In addition N_{sig} depends on a parameter μ that should be tested in the following:

$$P(N_{\text{data}}, N_{\text{sig}} + N_{\text{bkg}}) \rightarrow P(N_{\text{data}}, N_{\text{sig}}(\boldsymbol{\mu})(1 + \theta_s) + N_{\text{bkg}}(1 + \theta_b))$$

The corresponding likelihood function $L(\boldsymbol{\mu}, \boldsymbol{\theta})$ can be constructed with an additional Gaussian constraint that accounts for the uncertainties and their correlations by taking into account the covariance matrix C:

$$L(\boldsymbol{\mu}, \boldsymbol{\theta}) = P(N_{\text{data}}, N_{\text{sig}}(\boldsymbol{\mu})(1 + \theta_s) + N_{\text{bkg}}(1 + \theta_b)) \times \frac{1}{(2\pi)} e^{-\frac{1}{2}(\boldsymbol{\theta} C^{-1} \boldsymbol{\theta})} \tag{11.7}$$

Profile Likelihood Ratio and the p-Value To determine the 95% confidence interval for a parameter $\boldsymbol{\mu}_{\text{test}}$, a large number of pseudo experiments is needed. In each pseudo experiment pseudo data, N_{ps}, are taken from a Poisson distribution with the mean of $N_{\text{sig}}(\boldsymbol{\mu}) + N_{\text{bkg}}$. The signal and the background contribution is allowed to fluctuate independently for each pseudo experiment within their uncertainties, this is further denoted by a shift $\boldsymbol{\theta_0}$. The resulting likelihood function for a pseudo experiment is given as:

$$L(N_{\text{ps}}, \boldsymbol{\theta_0}, \boldsymbol{\mu}, \boldsymbol{\theta}) = P(N_{\text{ps}}, N_{\text{sig}}(\mu)(1 + \theta_s) + N_{\text{bkg}}(1 + \theta_b)) \times \frac{1}{(2\pi)} e^{-\frac{1}{2}(\boldsymbol{\theta} - \boldsymbol{\theta_0} C^{-1} \boldsymbol{\theta} - \boldsymbol{\theta_0})} \tag{11.8}$$

This likelihood function can be used to build a profile likelihood ratio[3] [108]:

$$\lambda(N_{\text{ps}}, \boldsymbol{\theta_0}, \boldsymbol{\mu}_{\text{test}}) = \frac{\max_{\hat{\theta}} L(N_{\text{ps}}, \boldsymbol{\theta_0}, \boldsymbol{\mu}_{\text{test}}, \hat{\hat{\theta}})}{\max_{\hat{\mu}, \hat{\theta}} L(N_{\text{ps}}, \boldsymbol{\theta_0}, \hat{\boldsymbol{\mu}}, \hat{\boldsymbol{\theta}})}, \tag{11.9}$$

where the numerator is maximised for $\hat{\hat{\boldsymbol{\theta}}}$ for a given $\mu = \mu_{\text{test}}$, while the denominator is maximised (unconstrained) for $\hat{\boldsymbol{\mu}}$ and $\hat{\boldsymbol{\theta}}$, i. e. $\hat{\boldsymbol{\mu}}$ and $\hat{\boldsymbol{\theta}}$ are the true maximum likelihood estimators. The ratio is always positive, with a maximum at $\lambda(N_{\text{ps}}, \boldsymbol{\theta_0}, \boldsymbol{\mu}_{\text{test}}) = 1$, when $\boldsymbol{\mu}_{\text{test}} = \hat{\boldsymbol{\mu}}$. The profile likelihood ratio for each pseudo experiment is tested against the profile likelihood containing the measured data. If

$$\lambda(N_{\text{ps}}, \boldsymbol{\theta_0}, \boldsymbol{\mu}_{\text{test}}) < \lambda(N_{\text{data}}, 0, \boldsymbol{\mu}_{\text{test}}) \tag{11.10}$$

[3] A good choice for the estimator of a parameter α is the one that maximises the likelihood function, which is denoted as $\hat{\alpha}$.

the pseudo experiment is less likely than the measurement. For the limit setting 10000 pseudo experiments are performed and the p-value is calculated, which is defined as follows:

$$p - \text{value}(\boldsymbol{\mu}_{\text{test}}) = \frac{\text{Number of pseudo exp. less likely than the measurement}}{\text{All pseudo experiments}} \tag{11.11}$$

The limits are derived where the p-value is smaller 5%, which means, the tested value $\boldsymbol{\mu}_{\text{test}}$ can be excluded at 95% CL.

11.4 Optimisation

The optimal cut on the leading jet p_{T}, and therefore the definition of the final phase space for the limit setting, is found by testing the expected limits[4] on the three CP conserving parameters, g_1^Z, κ_Z and $\lambda_{Z\gamma}$ for $\Lambda_{FF} = \infty$, taking into account the statistical and (only) experimental uncertainties in each phase space. The optimisation is mainly driven by the signal and background numbers and the size of the uncertainties, therefore it is sufficient to test only three parameters and only for $\Lambda_{FF} = \infty$. Figure 11.7 shows the expected limits for the three CP conserving parameters for leading jet p_{T} cut from 300-800 GeV, where all values outside the given intervals are excluded at the 95 % confidence level. The

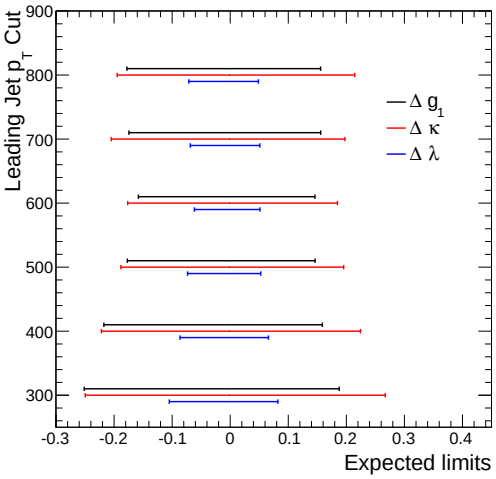

Figure 11.7: Expected limits at 95% CL for different leading jet p_{T} cuts for the three CP conserving parameters for $\Lambda_{FF} = \infty$.

smallest interval induces the most stringent limits. Starting at $p_{\text{T}} > 300$ GeV the limits are getting better by increasing the p_{T} cut, the best limits are found at $p_{\text{T}} > 600\,\text{G}e\text{V}$, which is used to define the phase space for the limit setting.

[4] Expected limits are calculated by using the sum of the SM signal and the backgrounds as the data in the fit.

11.5 Uncertainties

The sources of uncertainties, that are taken into account in the limit setting, are mostly the same as for the cross section measurement, described in chapter 9. Further details on the evaluation of the uncertainties for the limit setting are given below.

Experimental Uncertainties The experimental uncertainties due to the detector measurements are assumed to be 100% correlated between all processes. Therefore, all MC backgrounds and the SM signal are varied at the same time within the uncertainty. For all backgrounds, apart from the QCD W + jets production, the change in the number of predicted events is derived by performing the fit for the background extrapolation on the varied background shape. Instead of an uncertainty for each background, the shift in the total MC prediction is taken as the (fractional) uncertainty due to the tested uncertainty source. This results in an average uncertainty, which can be more easily considered in the limit setting and will not change the results much. The two most important processes, the QCD W + jets background and the EW W + jets production are anyway dominated by their theoretical uncertainty (see next section) and for all other background a 100% uncertainty is assumed on the event numbers from the extrapolation and thus the effect from the experimental uncertainty is anyway negligible. The resulting experimental uncertainties are given in table 11.2. As most of the experimental uncertainties are small, several components are already combined in the table, by adding them in quadrature.

Table 11.2: Experimental uncertainties for optimised phase space derived from MC samples.

	Uncertainty [%]
JER	2.9
JES	6.8
JVF	0.3
$\not{E}_T$	0.3
lepton	1.5

Theory Uncertainties As in the cross section measurement, the uncertainties on the QCD W + jets and the EW W + jets due to the choice of the renormalisation and the factorisation scale as well as the PDF choice (including α_s variation), the parton shower and the interference are evaluated separately, with the methods described in chapter 9. The interference between the EW signal and the QCD W + jets background gives a negligible effect on the background prediction and is therefore neglected. Another dominant source of uncertainty on the QCD W + jets background is due to the alternative MC prediction from Sherpa. The same reweighting as for the cross section measurement (see sec. 7.6)

is applied and results in an uncertainty of 18.8% on the QCD W + jets background. All theory uncertainties in the optimised phase space are shown in table 11.3. On the other

Table 11.3: Theoretical uncertainties for the optimised phase space for the QCD W + jets and the EW W + jets process.

	Uncertainty [%]
QCD W + jets Scale	7.8
QCD W + jets PDF	11.1
QCD W + jets Shower	0.5
QCD W + jets Sherpa	18.8
EW W + jets Scale	14.3
EW W + jets PDF	7.0
EW W + jets Shower	1.0

backgrounds a 100% uncertainty is already assumed from the extrapolation and therefore no further theory or normalisation uncertainties are taken into account.

Luminosity Uncertainty As in the cross section measurement the 1.9% uncertainty on the integrated luminosity is directly considered in the limit setting.

Acceptance uncertainty The acceptance uncertainty of 13.7% (see section 11.1) that was derived from the comparison of the additional generated samples with the calculated parabola, is taken into account as an uncertainty on the EW signal.

The resulting event numbers for the optimised phase space are given in table 11.4. For the EW W + jets and the QCD W + jets production, the statistical and the systematic uncertainties are quoted separately, while for all other backgrounds the combined uncertainty is given. Those are anyway dominated by the 100% uncertainty from the extrapolation.

11.6 Limits on the effective Lagrangian

The limits at 95% CL on the CP conserving as well as the CP violating parameters of the effective Lagrangian approach are set using a profile likelihood ratio, described in section 11.3. The limits are based on the predicted event numbers and uncertainties for the optimised phase space with leading jet $p_{\mathrm{T}} > 600\,\mathrm{G}e\mathrm{V}$, that are discussed in the previous section. In Table 11.5 the expected and observed limits for $\Lambda_{FF} = \infty$ and $\Lambda_{FF} = 4$ TeV are shown. All limits are also presented in figure 11.8 where the dashed lines refer to the expected limits, while the solid lines represent the observed limits. As expected,

Table 11.4: Event numbers for the EW W + jets and the background processes for the optimised phase space with leading jet $p_{\mathrm{T}} > 600\,\mathrm{GeV}$. For the EW W + jets and QCD W + jets process the statistical and systematic uncertainties are given. All other backgrounds have a 100% uncertainty from the background extrapolation.

	Combined
QCD W + jets	16.0 ± 1.2 (stat.) ± 3.9 (syst.)
Diboson	0.5 ± 0.5
$t\bar{t}$	5.6 ± 5.6
single top	1.3 ± 1.3
Multijet	0.1 ± 0.1
Other	0.8 ± 0.8
EW W + jets	10.5 ± 0.8 (stat.) ± 1.8 (syst.)
Total SM	34.8 ± 7.4 (stat. + syst.)
Data	30

Table 11.5: Expected and observed one dimensional limits at 95% CL for the CP conserving and the CP violating TGC parameters of the effective Lagrangian approach, tested with the LEP scenario. While one parameter is varied, the others are held constant at their SM values.

	$\Lambda_{FF} = 4$ TeV		$\Lambda_{FF} = \infty$	
	expected	observed	expected	observed
Δg_1^Z	[-0.390, 0.354]	[-0.339, 0.304]	[-0.163, 0.151]	[-0.142, 0.130]
$\Delta\kappa_1^Z$	[-0.375, 0.505]	[-0.315, 0.445]	[-0.183, 0.191]	[-0.158, 0.166]
$\lambda_{Z/\gamma}$	[-0.161, 0.117]	[-0.142, 0.098]	[-0.064, 0.053]	[-0.056, 0.045]
$\Delta\tilde{\kappa}_1^Z$	[-1.734, 1.793]	[-1.473, 1.534]	[-0.813, 0.771]	[-0.706, 0.665]
$\tilde{\lambda}_{Z/\gamma}$	[-0.127, 0.143]	[-0.109, 0.125]	[-0.058, 0.057]	[-0.050, 0.049]

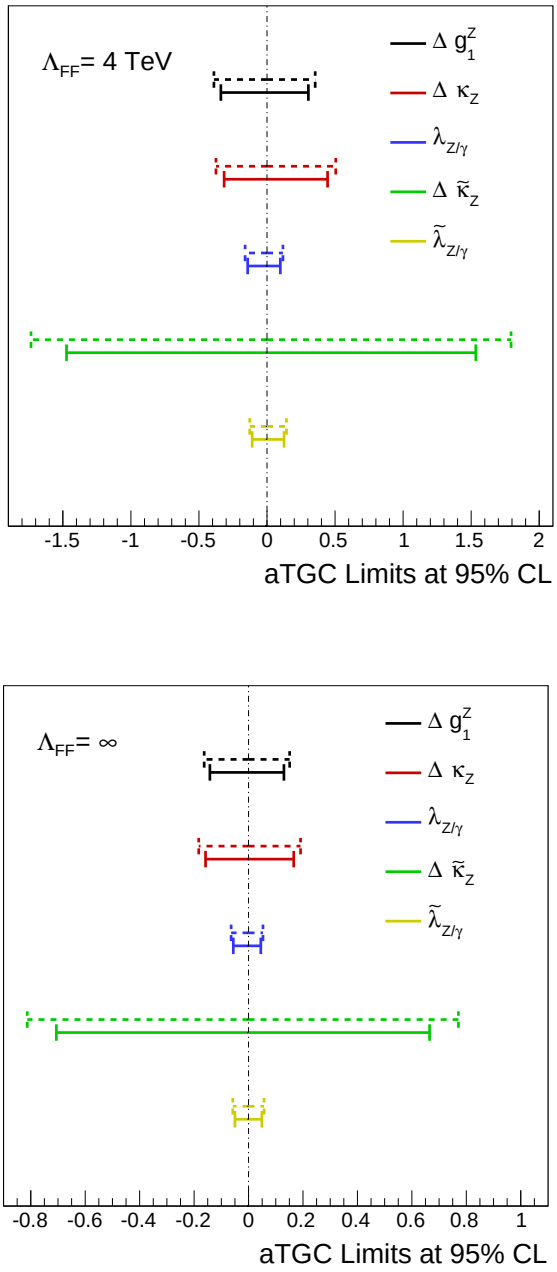

Figure 11.8: Expected (dashed line) and observed (solid line) one dimensional limits at 95% CL for the CP conserving as well as the CP violating aTGC parameters of the effective Lagrangian approach. All parameters are tested with the LEP scenario. The limits are set for $\Lambda_{FF} = 4$ T*e*V (upper plot) and $\Lambda_{FF} = \infty$ (lower plot).

the limits for $\Lambda_{FF} = \infty$ are more stringent, because the predicted variation in the event numbers for the TGC parameters is larger. For $\Lambda_{FF} = \infty$ and $\Lambda_{FF} = 4$ TeV the observed limits are always slightly more stringent than the expected limits due to a small deficit in data. It was also found that the given analysis has only very little sensitivity to the parameter $\Delta\tilde{\kappa}_Z$, resulting in limits that are much larger than 1 for $\Lambda_{FF} = 4$ TeV and close to 1 for $\Lambda_{FF} = \infty$. In figure 11.9 the two dimensional limits for the combination of two of the CP conserving parameters are given for $\Lambda_{FF} = \infty$ and $\Lambda_{FF} = 4$ TeV. Due to the relations with $\Delta\kappa_\gamma$ in the LEP scenario the parameters Δg_1^Z and $\Delta\kappa_Z$ are correlated, this was also seen in other analyses, e.g. [109]. Also for the two dimensional limits the observed limits are always slightly better than the corresponding expected limits. Again, the limits for $\Lambda_{FF} = \infty$ are more stringent than the limits for $\Lambda_{FF} = 4$ TeV. For the one dimensional as well as for the two dimensional limits it is found that all parameters are consistent with their SM values.

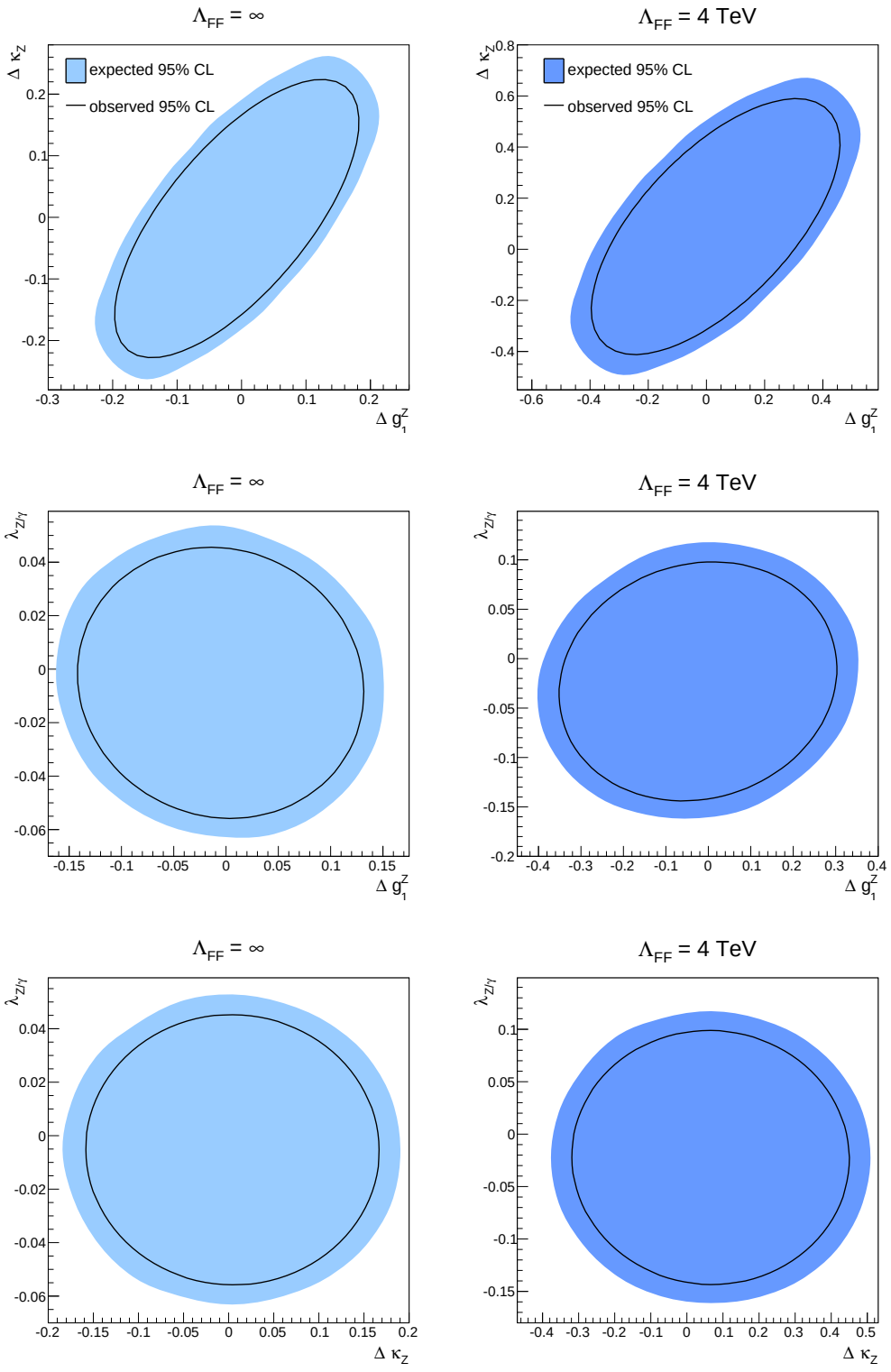

Figure 11.9: Expected and observed limits at 95% CL for the combination of two CP conserving aTGC parameters of the effective Lagrangian approach, tested with the LEP scenario. The limits are set for $\Lambda_{FF} = 4$ TeV and $\Lambda_{FF} = \infty$.

11.7 Effective Field Theory Interpretation

The limits for $\Lambda_{FF} = \infty$ from the effective Lagrangian can now be converted into limits for the CP conserving and CP violating parameters from the EFT with the relations given in section 2.7.2. The results are shown in table 11.6. The behaviour of the EFT limits is equal to the original limits from the effective Lagrangian, as they are just converted. Thus, the observed limits are slightly more stringent than the expected ones and the best sensitivity is found for $\frac{c_{WWW}}{\Lambda^2}$ and $\frac{c_{\tilde{W}WW}}{\Lambda^2}$ as they are directly connected to $\lambda_{Z/\gamma}$ and $\tilde{\lambda}_{Z/\gamma}$. As discussed in chapter 2.7.2 the EFT approach is only valid if the scale of new physics is far above the tested energies, otherwise the effective approach must not be used. The fact that the EFT approach allows a complete model-independent test of the triple gauge boson vertex, leads to the assumption that further measurements will quote their limits in terms of the EFT parameters and can directly be compared to the given analysis.

Table 11.6: EFT limits calculated limits on the anomalous coupling approach with $\Lambda_{FF} = \infty$ using the relations between the EFT parameters and those of the anomalous couplings in the restricted phase space with the leading jet $p_{\mathrm{T}} > 600$ GeV.

	expected	observed
$\frac{c_W}{\Lambda^2}$ [TeV^{-2}]	[-40.1, 37.2]	[-35.0, 32.0]
$\frac{c_B}{\Lambda^2}$ [TeV^{-2}]	[-203.6, 195.0]	[-177.0, 168.4]
$\frac{c_{WWW}}{\Lambda^2}$ [TeV^{-2}]	[-15.5, 12.8]	[-13.5, 10.9]
$\frac{c_{\tilde{W}}}{\Lambda^2}$ [TeV^{-2}]	[-793.4, 836.6]	[-684.3, 726.5]
$\frac{c_{\tilde{W}WW}}{\Lambda^2}$ [TeV^{-2}]	[-14.0, 13.8]	[-12.1, 11.9]

11.8 Comparison to other Limits

The above given limits from the anomalous couplings approach can be compared to results from previous measurements. The first collider experiment that had access to the required high energies was the LEP collider at CERN. In run II the energy was increased to $\sqrt{s} = 209\,\mathrm{G}e\mathrm{V}$ and one major goal of LEP II was to study the W boson pair production and the boson self-coupling. The process $e^+e^- \to W^+W^-$ is sensitive to the $WWZ/WW\gamma$ vertex and about 10000 W boson pairs were recorded at each of its four experiments. In addition to the W boson pair production, single W boson production in the process $e^+e^- \to e\nu_e W$ was also studied at LEP II. This can only happen in a VBF process at a lepton collider and is therefore sensitive to the triple gauge boson vertex. Limits on the single W boson production are not very stringent due to the small production cross section. Table 11.7 shows the observed one dimensional limits at 95% CL obtained by the L3 experiment at LEP for the parameters λ_γ and κ_γ [110].

Table 11.7: Observed limits on the CP conserving parameters λ_γ and κ_γ at 95% CL for single W boson production obtained by the L3 experiment at LEP

κ_γ	[-0.44, 0.29]
λ_γ	[-0.67, 0.59]

Furthermore, the results from all four LEP experiments, for the W-boson-pair and the single W boson production have been combined [111]. Because the collision energy at lepton colliders is well known, no form factors have to be applied for the limit setting. The CP conserving parameters g_1^Z, κ_γ, $\lambda_{Z/\gamma}$ of the effective Lagrangian have been tested with the LEP scenario and the resulting limits at 95% confidence level, are given in table 11.8, where κ_γ has been converted into κ_Z with the relations of the LEP scenario, given in section 2.7.3.

Table 11.8: Observed limits on the CP conserving parameters from the combination of the LEP experiments (using the LEP scenario). The limits are obtained at a center-of-mass energy of $\sqrt{s} = 209\,\mathrm{GeV}$ and therefore tested without a form factor.

g_1^Z	[-0.054, 0.021]
κ_Z	[-0.018, 0.028]
λ_γ	[-0.059, 0.017]

Those are the best available limits from lepton colliders to date and can be compared with the latest limits from hadron colliders. The DØ and the CDF experiment at the TeVatron tested the charged vector boson vertex in diboson production in proton-anti-proton collisions (see [112] and [113]). The obtained limits are less stringent than the ones from LEP and also less stringent than limits from the LHC and will not be considered further.

At the LHC the (charged) triple boson vertex is tested in boson pair production for proton-proton collisions (WW and WZ final states) as well as in single boson production due to VBF. The WZ final state is particularly sensitive to the WWZ vertex, whereas the WW can be produced via Z or γ. For $\sqrt{s} = 8$ TeV both final states are tested with and without form factors of $\Lambda_{FF} = 7$ TeV for the WW production [109] and of $\Lambda_{FF} = 2$ TeV and 15 TeV for WZ production [114] by the ATLAS experiment. The CMS collaboration published so far only limits for the WW production [115] for $\sqrt{s} = 8$ TeV. This analysis already used the EFT approach, thus no form factor is applied. The limits are converted into limits from the anomalous couplings approach making use of the relations given in section 2.7.3. All limits from the diboson production from hadron colliders can be found in table 11.9. To be comparable with the LEP II results only the limits without a form factor are given. The limits for WW production from the ATLAS collaboration are tested

with the LEP scenario, while the CMS experiment uses the HISZ basis [5]. For the WZ final state no scenario is needed as only the WWZ vertex contributes.

Table 11.9: Observed limits from the WW and WZ production probed by the ATLAS and the CMS experiment at $\sqrt{s} = 8\,\mathrm{T}e\mathrm{V}$. The couplings for the WW production are probed in the LEP and the HISZ scenario [5] for ATLAS and CMS. All limits are set in absence of a form factor.

	CMS: WW	ATLAS: WW	ATLAS: WZ
g_1^Z	[-0.046, 0.022]	[-0.016, 0.027]	[-0.019, 0.029]
κ_Z	[-0.022, 0.026]	[-0.025, 0.020]	[-0.19, 0.30]
λ_Z	[-0.024, 0.024]	[-0.019, 0.019]	[-0.016, 0.016]

The first limits on the WWZ vertex at space-like momentum transfer at hadron colliders have been performed with the ATLAS experiment at $\sqrt{s} = 8\,\mathrm{T}e\mathrm{V}$ in the measurement of electroweak Z + jets production [98](see section 6.5 for more details on the process). The electroweak Z + jets analysis sets limits on the CP conserving parameters g_1^Z and λ_Z with and without a form factor of $\Lambda_{FF} = 6$ TeV. The results without a form factor are given in table 11.10.

Table 11.10: Observed limits from the EW Z + jets production probed by the ATLAS experiment at $\sqrt{s} = 8\,\mathrm{T}e\mathrm{V}$ using $\Lambda = \infty$. These are the first limits from hadron colliders that are sensitive to the space-like momentum transfer of the three boson coupling.

g_1^Z	[-0.50 , 0.26]
λ_Z	[-0.15, -0.13]

Figure 11.10 shows a summary of the combined limits from LEP, the diboson limits from ATLAS and CMS as well as the limits from the EW Z + jets production together with the observed limits for $\Lambda_{FF} = \infty$ obtained in this analysis.

As expected the limits from the WW production (from ATLAS and CMS) and the combined limits from LEP are more stringent than the limits obtained from the EW W + jets production and for g_1^Z and κ_Z even approximately one order of magnitude better. Nevertheless, the limits on $\lambda_{Z/\gamma}$ are comparable between the diboson analyses, the combined LEP results and the EW W + jets production. When comparing the limits from the WW and the WZ final state, it can be seen that the limits for g_1^Z and $\lambda_{Z/\gamma}$ are comparable between the two channels, while for κ_Z the limits for the WZ final state are less stringent than the ones from the WW final state and also less stringent compared to the other limits from the WZ process. This is due to the fact that for the WZ final state the parameter κ_Z is proportional to $\sqrt{\hat{s}}$, while the other parameters are proportional

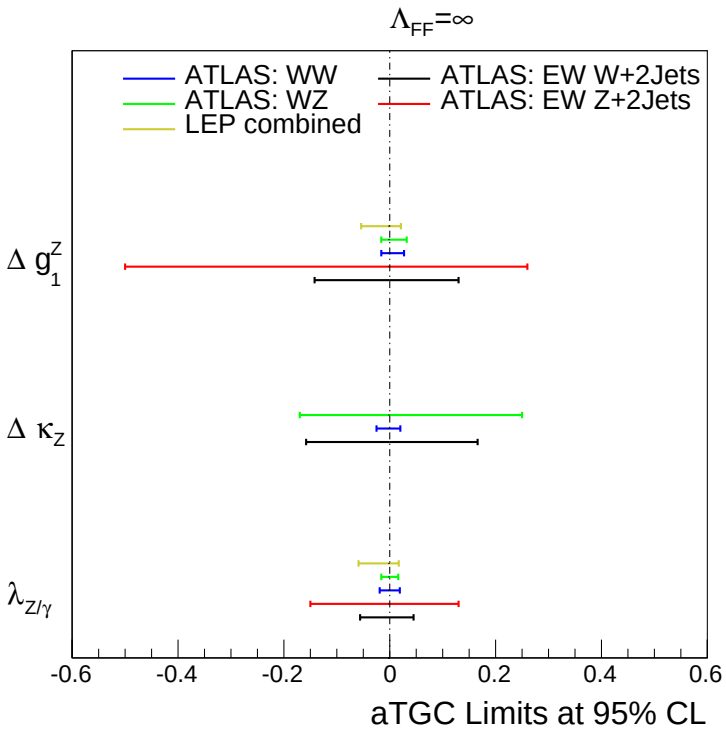

Figure 11.10: Observed limits for the CP conserving parameters of the effective Lagrangian approach for various analyses from the ATLAS and CMS experiment probed at $\sqrt{s} = 8\,\mathrm{T}e\mathrm{V}$ and the LEP experiment. The combined LEP limits, the WW from ATLAS and the EW W + jets production are probed with the LEP scenario. The limits from the WW analysis from CMS are set on the HISZ basis. The EW Z + jets anaylsis did not set limits for κ_Z. All limits are set without a form factor.

to $\hat{s}$. For the WW process all parameters are proportional to $\hat{s}$ and therefore they are all comparable. The limits on κ_Z from the WZ final state is even slightly less stringent than corresponding limits from the EW W + jets analysis. With the diboson results from ATLAS and CMS at $\sqrt{s} = 8\,\mathrm{T}e\mathrm{V}$ for the first time limits could be obtained from hadron colliders which are as good as the limits from LEP.

As already mentioned, the EW W + jets production is able to test the charged triple gauge boson vertex in a space-like momentum transfer. This was previously done by the EW Z + jets analysis, but only for g_1^Z and λ_Z. With the performed EW W + jets analysis those limits could be improved by approximately a factor of 2-5 and also complete the set of parameters by constraining κ_Z.

12 — Summary and Outlook

Due to the outstanding performance of the LHC during the first run (2010-2012) the observation of a new spin-0 particle with a mass of approximately 125 GeV could be announced on the 4th of July 2012. So far this particle is identified with the SM Higgs boson. Nevertheless, some properties of the new boson still have to be measured. With the confirmed presence of the Higgs boson the SM is complete. However, there are phenomena which are observed in measurements but can not be described by the SM. Therefore, the search for an extension of the known theory continues. The measurement of the EW W + jets production in proton-proton collision with $20\,\text{fb}^{-1}$ of data recorded with the ATLAS experiment at $\sqrt{s} = 8\,\text{T}e\text{V}$ in 2012, presented in this thesis, contributes to the search of new physics as well as to a deeper understanding of the topology of VBF events. The latter is particularly interesting as the second most frequent production of the Higgs boson is also via VBF.

The probability of W + jets events being produced by pure EW interaction is much smaller than the corresponding production of a W boson with jets from strong vertices. However, the VBF component of the EW signal introduces a characteristic event topology with two high energy forward jets. An event selection is developed that is mainly based on the kinematics of the tagging jets and is able to separate the small signal from the much larger background. The resulting event selection has an efficiency of $\approx 30\%$ for the signal and only about 3% for the main QCD W + jets background.

The QCD W + jets process and most of the other backgrounds are predicted by MC simulation with sufficient statistics. Only for the multijet background an adequate amount of events is difficult to achieve by the simulation and therefore a data-driven technique is developed to model the shape of this background. Events from collision data are selected by relaxing the isolation criteria for the leptons, which are expected to model the shape of the background in all relevant distributions. The normalisation of the background is determined with a fit to data.

The cross section of the EW W + jets is measured by performing a binned likelihood fit to the M_{jj} distribution using three templates, one for the EW signal, one for the QCD W + jets background and one for the other background. This fit is done simultaneously in the electron and the muon channel, where the signal and the QCD W + jets background are allowed to float independently, while the template with the minor backgrounds is held constant. With the resulting SF for the EW signal, that is obtained with respect to the MC prediction, of $0.85 \pm 0.04\,(\text{stat.}) \pm 0.19\,(\text{syst.})$, the fiducial cross section is determined to

$$\sigma_{\text{fid}} = 337.1 \pm 15.8(\text{stat.}) \pm 76.9(\text{syst.}) \pm 6.1(\text{lumi})\ \text{fb} \tag{12.1}$$

The measured cross section agrees within the uncertainties with the theoretical prediction from POWHEG of $\sigma_{\text{theory, fid}} = 395 \pm 4(\text{scales}) \pm 17(\text{shower})\,\text{fb}$. The dominant uncertainties

in the measurement arise from the theoretical uncertainties on the signal and the background prediction, with the largest components being the modelling of the EW signal and the QCD W + jets background as well as the PDF uncertainty, the choice of the factorisation and renormalisation scale and the PS. The dominant experimental uncertainties are due to the jet energy resolution and the jet energy scale.

The VBF component of the signal process is used to set limits on anomalous couplings of the charged three boson vertex $WWZ/WW\gamma$. For the limit setting a phase space is defined that has an even higher purity of the EW W + jets contribution of about 30%. This is achieved by tightening the cut on M_{jj} from 500 GeV to 1 TeV and on the leading jet p_{T} distribution from 80 GeV to 600 GeV. Most of the backgrounds do not contain enough events to make reliable predictions in this very restrictive phase space and therefore an extrapolation is performed by a fit with a numerical function, that extends the leading jet p_{T} distribution up to 1 TeV.

One dimensional limits are set on CP conserving parameters g_1^Z, κ_Z and $\lambda_{Z/\gamma}$ as well as on CP violating parameters, $\tilde{\kappa}_Z$ and $\tilde{\lambda}_{Z/\gamma}$, from the effective Lagrangian from the anomalous couplings approach. In addition two dimensional limits are set on the linear combination of two CP conserving parameters. The parameters are tested in the LEP scenario with ($\Lambda_{FF} = 4$ TeV) and without a form factor ($\Lambda_{FF} = \infty$). All parameters are found to be consistent with their SM values. The limits can further be compared with results on CP conserving parameters from previous analyses. As expected the results are not as stringent as the limits that were achieved from the measurement of WW and the WZ production with the ATLAS and the CMS experiment at $\sqrt{s} = 8$ TeV as the cross section of those processes is much higher. The obtained limits are also less stringent than the LEP limits which have been the best limits so far. Nevertheless, the obtained limits improved the limits on the WWZ vertex with space-like momentum transfer which were set using EW Z + jets production, by roughly a factor of two. In addition the limits probed in this analysis are the first limits on the WWZ vertex using single W-boson production at hadron colliders and contributed significantly to understand the space-like momentum transfer at the WWZ vertex and the nature of EW physics.

The limits that are performed without the form factor are further converted into limits from an EFT, which provides a different approach to parameterise deviations from the SM in a model-independent way. It can be assumed that further measurements will quote their limits in terms of the EFT and can directly be compared to this analysis.

There are a few points where the performed measurement can be improved. The cross section measurement is dominated by the systematic uncertainties, where the largest contributions arise from the theoretical uncertainties on the signal and the background prediction. For the EW signal and the QCD W + jets background the dominant components of the theory uncertainties are found from the modelling that was tested with an additional Sherpa sample. The Sherpa prediction is only available at LO in QCD. Even though a reweighting on the QCD W + jets background is performed to improve the modelling of the Sherpa prediction in the M_{jj} distribution, it still gave the largest uncertainty. It is therefore essential to have alternative predictions at NLO in QCD for the two most

important components of the measurement. Ideally those new predictions can make use of filters in the generation, which would allow to simulate more events in the tail of the M_{jj} distribution. The analysis would also benefit from signal and background generations with smaller uncertainties due to the choice of the PDF as well as the renormalisation and factorisation scale. The dominant source from the experimental uncertainties are due to the jet energy scale and resolution. Those may be improved in the future with better understanding of the detector.

In addition it was already mentioned that the estimate of the multijet background is developed and optimised for the electron channel and only adopted to the muon channel. It is very likely that this estimate can be improved by studying the muon identification criteria, such that they can be (partially) relaxed to increase the statistics of the template and also improve the modelling in some distributions. However, it was seen that the multijet background has only a minor effect on the cross section extraction.

Furthermore, there are investigations ongoing to constrain the uncertainties in a control region, that is similarly defined as the one in section 7.6. The uncertainties are correlated between the signal and the control region and thus only the change between the two regions has to be considered. It is expected that this reduces the total uncertainty for the cross section measurement by a factor of 2.

In the limit setting the theoretical uncertainties are also found to have the largest impact on the analysis. Thus, the limits setting would also benefit from the above mentioned improvements on the prediction of the QCD W + jets background and the EW signal. Another important point is the limited statistics of the minor backgrounds which results in a 100% uncertainty due to the extrapolation strategy. The generation of the backgrounds can also benefit from high-M_{jj} filters that reduce the statistical uncertainty in the interesting phase space.

In addition, it would also be useful for the limit setting to vary the couplings of the three boson vertex in predictions at NLO in QCD.

Besides the improvement of the analysis strategy, it would also be interesting to perform the measurement at higher energies as provided by Run II of the LHC with $\sqrt{s} = 13\,\mathrm{T}e\mathrm{V}$. This will substantially improve the limit setting for the $WWZ/WW\gamma$ vertex as much higher energies can be tested. With more statistics in the high energy regime a differential limits setting in, e.g. the leading jet p_{T} distribution can be performed and potentially increase the sensitivity on the parameters.

Acknowledgements

I would now like to thank all the people which supported me during the years of my PhD. I am pretty sure I forget someone:

First and foremost, special thanks to Prof. Dr. Christian Zeitnitz for giving me the opportunity to contribute to physics research and for supporting me in my choice of thesis topic. In addition he enabled me to stay at CERN for 14 month and to attend conferences in Warsaw and New York as well as the summer school in Hungary. I learned a lot from you, not only about particle physics but how to install an oven and how to change a bulb in my car. I have benefited so often from your patience and even learned how to be patient myself (at least a bit).

I am truly indebted and thankful to Dr. Frank Ellinghaus for taking on me and my analysis, and putting substantial amounts of time into this. You know that this thesis would not have been finished without your enduring support, even in times of injury. I very much enjoyed our uncountable coffee breaks, the football events and stadium visits, especially when you managed to get us tickets to see Bayern Munich. I would also like to thank his wife Dr. Julia Ellinghaus, who had to stand a lot of multijet and aTGC discussions in the past few months. It is great that you both found your way to Wuppertal.

I would also like to thank PD Dr. Ulrike Blumenschein, for being the co-referee of this thesis and the continuous support on the analysis. At the beginning as the convenor of the WZ sub-group as well as in her time in Wuppertal and nowadays as the Standard Model convenor, she has always shown her interest in this analysis and promoted us with the deep knowledge.

I would also like to express my gratitude to all present and former members of the VBF W group for the support in the past four years and the many fruitful discussions. In particular I would like to thank Dr. James Henderson for developing the VBFramework, which made VBF a lot more fun, and his always open skype chat that helped me out so often with ROOT and Python problems.

I would like to thank all the people that contributed to increasing the quality of this thesis by proof reading and many physics discussion (in alphabetic order): Arwa Bannoura, Benedikt Bergenthal, Dr. Frank Ellinghaus, Dr. Gunar Ernis, Dr. Tobias Flick, Dr. Geoffrey Gilles, Dr. Klaus Hamacher, Dr. Marisa Sandhoff and Dr. Marcelo Vogel.

My sincere thanks goes to Dr. Gunar Ernis for being a great office mate and a good friend especially in the not-so-easy times after coming back from CERN in fall 2013. I am so grateful for your support in questions of physics and programming. I very much enjoyed our discussions on gender issues, although I know you did not...

Besides Gunar, I shared the office with many other people and I have always been lucky: It was a lot of fun. Thank you to all present and former office mates.

A big thank also to the "Gridpiloten" Dr. Torsten Harenberg und Dr. Marisa Sandhoff for the kind support in all questions somehow related to "computing", for sharing gossip and providing tons of sweets to desperate PhD students. Just the two of them managed to keep the computing infrastructure up on approximately 365 days per year, including last minute fixes on Christmas Eve.

There are so many other great people in the WHEP group. I really much enjoyed working with you all. This is not an exhaustive list: Mathias, Frank V., der kleine Oskar, Arwa, Benedikt, Dominik, Christian...

I would also like to thank a few people from the non-physics background (also not an exhaustive list): Karoline with "my" little Julian, Natascha and Daniel, Janine with Laura, Hannah, Christine, Klaus...

Last but not least, a special thank you to my family, who supported me (not only financially) throughout all of my academic studies.

A — Reconstruction Level Distributions in the VBF Phase Space

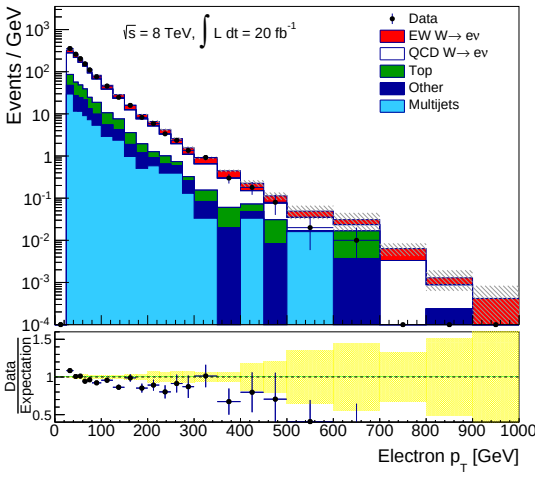

(a) electron channel

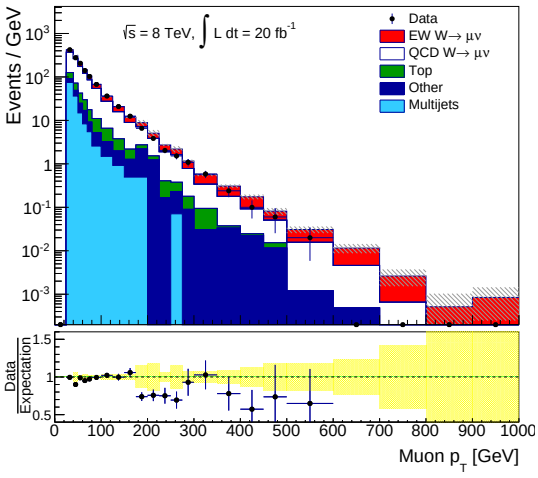

(b) muon channel

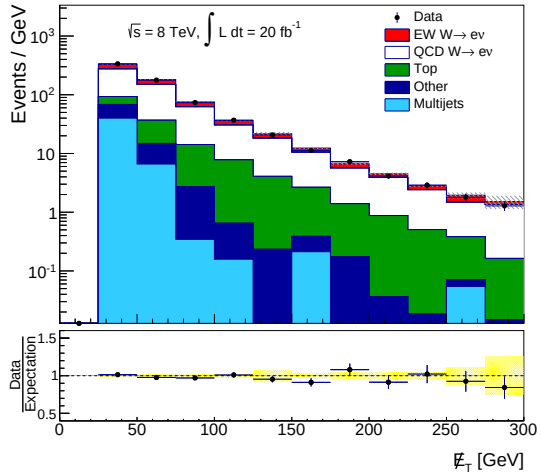

(c) electron channel

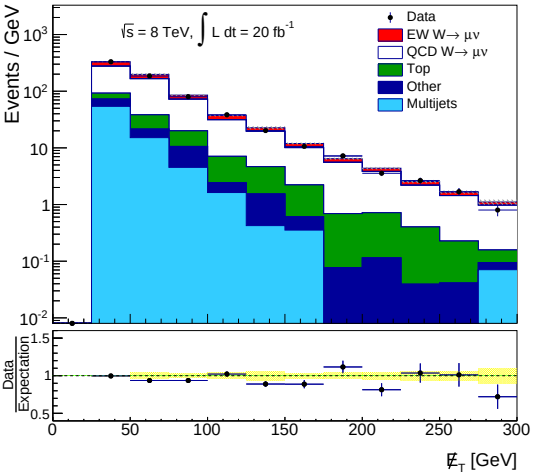

(d) muon channel

Figure A.1: Lepton p_{T} and $\not{E}_T$ distribution in the VBF phase space for the electron and muon channel. The data are shown as black points with error bars corresponding to the statistical uncertainty. The lower plot panel shows the comparison of the stacked signal and background components with the data. The grey shaded band in the upper panel and the yellow band in the lower panel indicate the statistical uncertainty on the sum of predicted signal and background.

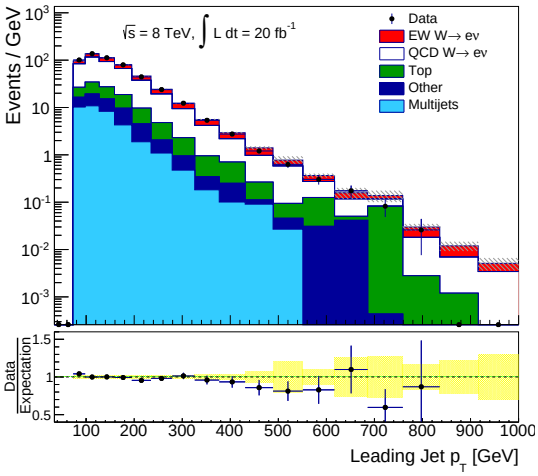

(a) electron channel

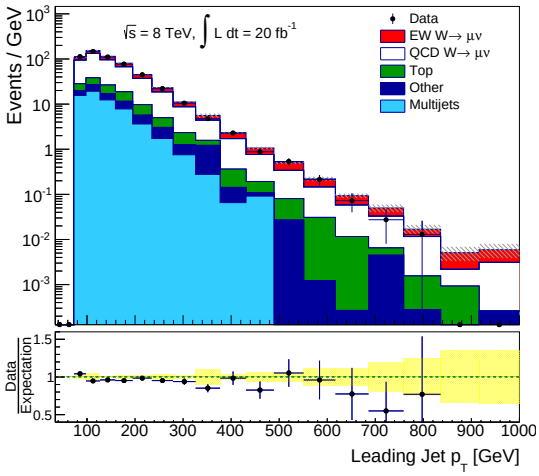

(b) muon channel

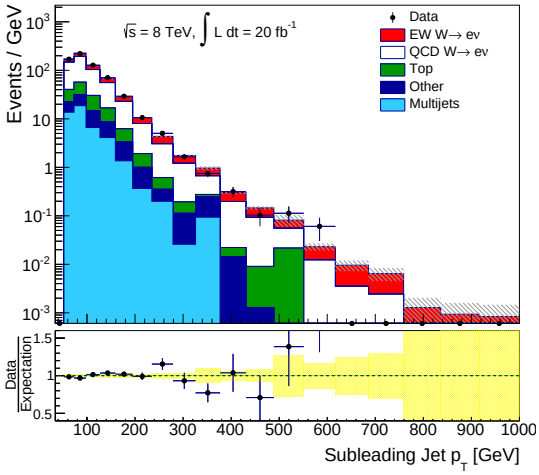

(c) electron channel

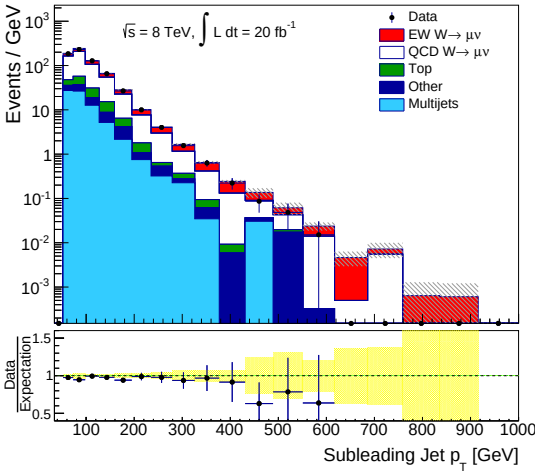

(d) muon channel

Figure A.2: Leading and subleading jet p_{T} distribution in the VBF phase space for the electron and muon channel. The data are shown as black points with error bars corresponding to the statistical uncertainty. The lower plot panel shows the comparison of the stacked signal and background components with the data. The grey shaded band in the upper panel and the yellow band in the lower panel indicate the statistical uncertainty on the sum of predicted signal and background.

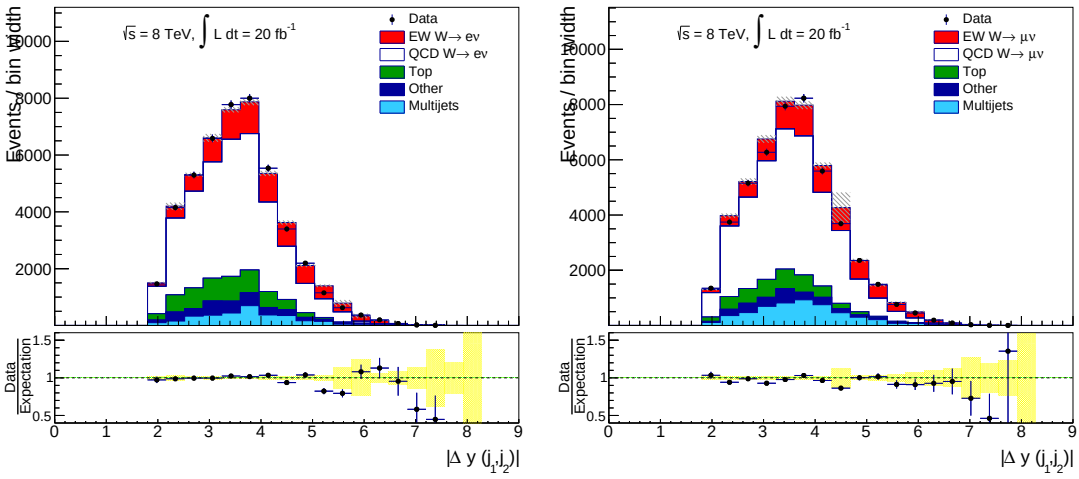

(a) electron channel

(b) muon channel

Figure A.3: $|\Delta y_{jj}|$ distribution in the inclusive W + jets phase space for the electron and muon channel. The data are shown as black points with error bars corresponding to the statistical uncertainty. The lower plot panel shows the comparison of the stacked signal and background components with the data. The grey shaded band in the upper panel and the yellow band in the lower panel indicate the statistical uncertainty on the sum of predicted signal and background.

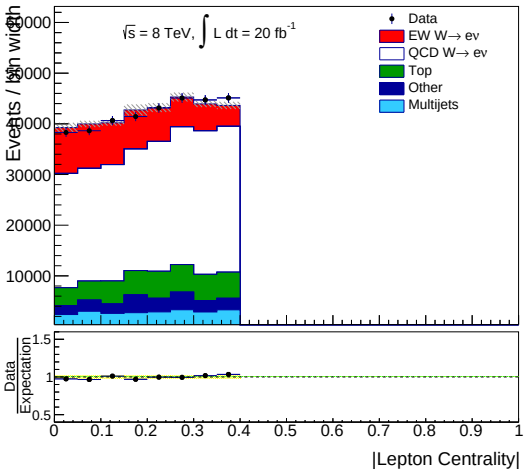

(a) electron channel

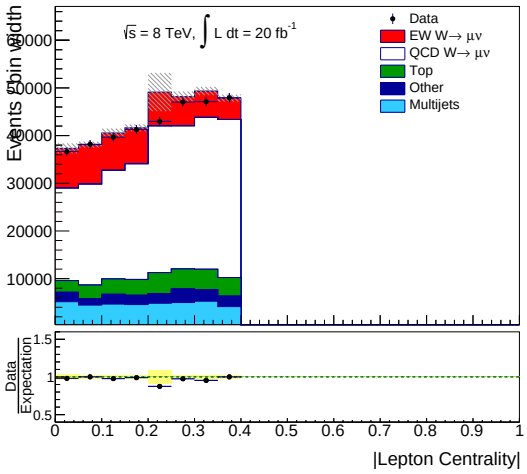

(b) muon channel

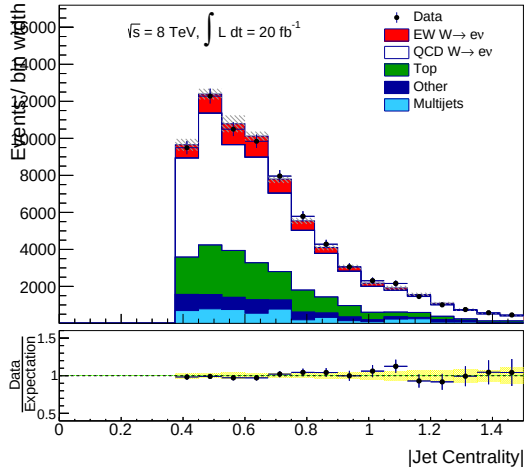

(c) electron channel

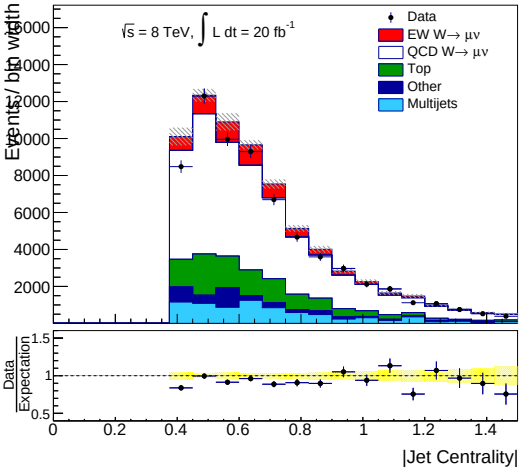

(d) muon channel

Figure A.4: Lepton und Jet Centrality distribution in the inclusive W + jets phase space for the electron and muon channel. The data are shown as black points with error bars corresponding to the statistical uncertainty. The lower plot panel shows the comparison of the stacked signal and background components with the data. The grey shaded band in the upper panel and the yellow band in the lower panel indicate the statistical uncertainty on the sum of predicted signal and background.

B — Samples for Limit Setting

Table B.1 summarises the samples that are generated with SHERPA 1.4.5 at truth level with TGC parameter variations. The samples in table B.1 are the minimal set of samples that are needed for the one dimensional and the two dimensional limit setting. The samples are generated for $\Lambda_{FF} = 4$ TeV as well as for $\Lambda_{FF} = \infty$.

Table B.1: Overview of the samples with TGC variations generated with SHERPA 1.4.5. The full set of samples were generated for $\Lambda_{FF} = 4$ TeV and also for $\Lambda_{FF} = \infty$.

	g_1^Z	κ_Z	λ_Z	$\tilde{\kappa}_Z$	$\tilde{\lambda}_Z$
Sample 0 (SM)	1	1	0	1	0
Sample 1	0	1	0	1	0
Sample 2	2	1	0	1	0
Sample 3	1	0	0	1	0
Sample 4	1	2	0	1	0
Sample 5	1	1	-1	1	0
Sample 6	1	1	1	1	0
Sample 7	2	2	0	1	0
Sample 8	2	1	1	1	0
Sample 9	1	2	1	1	0
Sample 10	1	1	0	0	0
Sample 11	1	1	0	2	0
Sample 12	1	1	0	1	-1
Sample 13	1	1	0	1	1

In addition samples have been generated for $\Lambda_{FF} = \infty$ where the variation for each parameter is set to $-1, -0.5, -0.1, -0.05, -0.01, 0, 0.01, 0.05, 0.1, 0.5, 1$.

C — Plots for Background Extrapolation

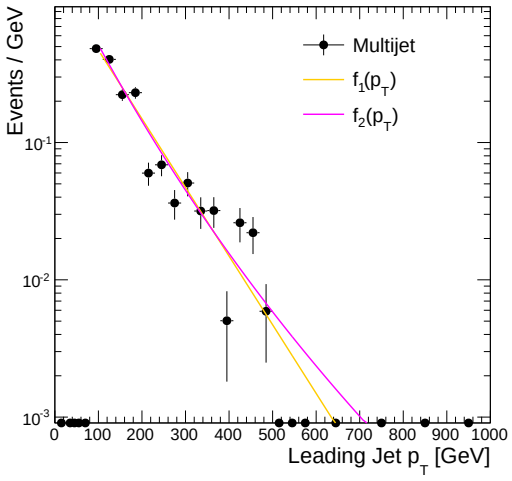

(a) Multijet Background

Figure C.1: Extrapolation of the leading jet p_{T} distribution for the multijet background with two different numerical functions. The error bars reflect the statistical uncertainties on the prediction.

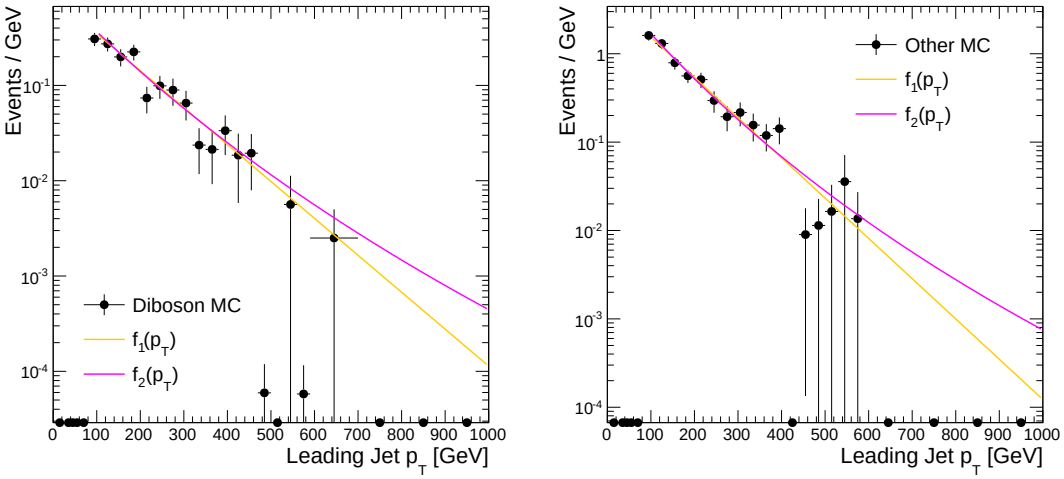

(a) Diboson Backgrounds

(b) Other Backgrounds

Figure C.2: Extrapolation of the leading jet p_{T} distribution for the diboson background and the sum of other minor backgrounds with two different numerical functions. The error bars reflect the statistical uncertainties on the MC prediction.

Bibliography

[1] D. J. Griffiths. *Introduction to elementary particles*. Wiley-VCH-Verlag, Weinheim, 2nd edition, 2008.

[2] M. E. Peskin and D. V. Schroeder. *An Introduction to Quantum Field Theory*. Westview Press, 1995.

[3] U. Baur and D. Zeppenfeld. Unitarity Constraints on the Electroweak Three Vector Boson Vertices. *Phys. Lett.*, B201:383, 1988.

[4] K. Hagiwara, R.D. Peccei, D. Zeppenfeld, and K. Hikasa. Probing the weak boson sector in $e^+e^- \to \mathrm{W}^+\mathrm{W}^-$. *Nuclear Physics B*, 282:253 – 307, 1987.

[5] K. Hagiwara, S. Ishihara, R. Szalapski, and D. Zeppenfeld. Low energy effects of new interactions in the electroweak boson sector. *Phys. Rev. D*, 48:2182–2203, Sep 1993.

[6] H. Aihara et al. Anomalous gauge boson interactions. 1995.

[7] K. A. Olive et al. Review of Particle Physics. *Chin. Phys.*, C38:090001, 2014.

[8] ATLAS Collaboration. Observation of a new particle in the search for the Standard Model Higgs boson with the ATLAS detector at the LHC. *Phys. Lett. B*, 716:1, 2012.

[9] CMS Collaboration. Observation of a new boson at a mass of 125 GeV with the CMS experiment at the LHC. *Phys. Lett. B*, 716:30, 2012.

[10] S.L. Glashow. Partial Symmetries of Weak Interactions. *Nucl.Phys.*, 22:579–588, 1961.

[11] S. Weinberg. A Model of Leptons. *Phys.Rev.Lett.*, 19:1264–1266, 1967.

[12] A. Salam and J.C. Ward. Electromagnetic and Weak Interactions. *Physics Letters*, 13(2):168–171, 1964.

[13] D. J. Gross and F. Wilczek. Ultraviolet Behavior of Nonabelian Gauge Theories. *Phys.Rev.Lett.*, 30:1343–1346, 1973.

[14] H. D. Politzer. Reliable Perturbative Results for Strong Interactions? *Phys.Rev.Lett.*, 30:1346–1349, 1973.

[15] H. Fritzsch, M. Gell-Mann, and H. Leutwyler. Advantages of the color octet gluon picture. *Physics Letters B*, 47(4):365–368, 1973.

[16] C. Quigg. Spontaneous Symmetry Breaking as a Basis of Particle Mass. *Rept.Prog.Phys.*, 70:1019–1054, 2007.

[17] J. H. Christenson, J. W. Cronin, V. L. Fitch, and R. Turlay. Evidence for the 2π decay of the k_2^0 meson. *Phys. Rev. Lett.*, 13:138–140, Jul 1964.

[18] P. W. Higgs. Broken symmetries, massless particles and gauge fields. *Phys. Lett.*, 12:132–133, 1964.

[19] F. Englert and R. Brout. Broken Symmetry and the Mass of Gauge Vector Mesons. *Phys. Rev. Lett.*, 13:321–322, 1964.

[20] P. W. Higgs. Spontaneous symmetry breakdown without massless bosons. *Phys. Rev.*, 145:1156–1163, 1966.

[21] G.S. Guralnik, C.R. Hagen, and T.W.B. Kibble. Global conservation laws and massless particles. *Phys. Rev. Lett.*, 13:585–587, 1964.

[22] N. Cabibbo. Unitary Symmetry and Leptonic Decays. *Phys. Rev. Lett.*, 10:531–533, Jun 1963.

[23] M. Kobayashi and T. Maskawa. CP-Violation in the Renormalizable Theory of Weak Interaction. *Progress of Theoretical Physics*, 49(2):652–657, 1973.

[24] R. P. Feynman. Space-time approach to quantum electrodynamics. *Phys. Rev.*, 76:769–789, Sep 1949.

[25] G. Gounaris et al. Triple gauge boson couplings. In *AGS / RHIC Users Annual Meeting Upton, New York, June 15-16, 1995*, 1996.

[26] C. Grojean, W. Skiba, and J. Terning. Disguising the oblique parameters. *Phys. Rev.*, D73:075008, 2006.

[27] Dieter Zeppenfeld. private communication.

[28] J. C. Collins, D. E. Soper, and G. F. Sterman. Factorization of Hard Processes in QCD. *Adv. Ser. Direct. High Energy Phys.*, 5:1–91, 1989.

[29] J. Gao et al. CT10 next-to-next-to-leading order global analysis of QCD. *Phys. Rev.*, D89(3):033009, 2014.

[30] Durham University. The durham hepdata project. http://hepdata.cedar.ac.uk/pdf/pdf3.html, 2015.

[31] D Linglin. Experimental observation of isolated large transverse energy electrons with associated missing energy at $\sqrt{s} = 540$ GeV. 1983.

[32] A. Straessner. *Electroweak Physics at LEP and LHC*. Springer-Verlag, Berlin Heidelberg, 1st edition, 2010.

[33] ATLAS Collaboration. The ATLAS Experiment at the CERN Large Hadron Collider. *JINST*, 3:S08003, 2008.

[34] CMS Collaboration. The CMS experiment at the CERN LHC. *JINST*, 3:S08004, 2008.

[35] LHCb Collaboration. The LHCb Detector at the LHC. *JINST*, 3:S08005, 2008.

[36] ALICE Collaboration. The ALICE experiment at the CERN LHC. *JINST*, 3:S08002, 2008.

[37] N. Cabibbo and G. Parisi. Exponential hadronic spectrum and quark liberation. *Physics Letters B*, 59(1):67 – 69, 1975.

[38] K. Schindl. The injector chain for the LHC. (CERN-OPEN-99-052):6 p, Jan 1999.

[39] J. Haffner. The CERN accelerator complex. Complexe des accélérateurs du CERN. Oct 2013. General Photo.

[40] K. Schindl. The PS Booster as Preinjector for LHC. *Part. Accel.*, 58(CERN-PS-97-011. CERN-PS-97-11. CERN-PS-97-011):63–78. 16 p, 1997.

[41] R Cappi. The PS in the LHC injector chain. *Part. Accel.*, 58(CERN-PS-97-016-CA):79–89. 13 p, Apr 1997.

[42] T. Linnecar. Preparing the SPS for LHC. *Part. Accel.*, 58:91–101, 1997.

[43] M. Lamont. Status of the lhc. *Journal of Physics: Conference Series*, 455(1):012001, 2013.

[44] J. Pequenao. Computer generated image of the whole ATLAS detector. Mar 2008.

[45] J. Pequenao. Computer generated image of the ATLAS inner detector. Mar 2008.

[46] J. Pequenao. Computer Generated image of the ATLAS calorimeter. Mar 2008.

[47] ATLAS Collaboration. Energy linearity and resolution of the atlas electromagnetic barrel calorimeter in an electron test-beam. *Nuclear Instruments and Methods in Physics Research Section A: Accelerators, Spectrometers, Detectors and Associated Equipment*, 568(2):601 – 623, 2006.

[48] J. Pequenao. Computer generated image of the ATLAS Muons subsystem. Mar 2008.

[49] M. Bruschi. The ATLAS luminosity monitor. *Nucl. Instrum. Meth.*, A623:371–373, 2010.

[50] O. Adriani et al. The LHCf detector at the CERN Large Hadron Collider. *JINST*, 3:S08006, 2008.

[51] S. Franz and P. Barrillon. Alfa—measuring absolute luminosity with scintillating fibres. *Nuclear Instruments and Methods in Physics Research Section A: Accelerators, Spectrometers, Detectors and Associated Equipment*, 610(1):35 – 40, 2009.

[52] https://twiki.cern.ch/twiki/bin/view/AtlasPublic/LuminosityPublicResults.

[53] https://atlas.web.cern.ch/Atlas/GROUPS/DATAPREPARATION/DataSummary/2012/runtable.html.

[54] M. Limper, S. Bentvelsen, and A.P. Colijn. *Track and vertex reconstruction in the ATLAS inner detector*. PhD thesis, Amsterdam University, 2009.

[55] R. E. Kalman. A new approach to linear filtering and prediction problems. *Transactions of the ASME–Journal of Basic Engineering*, 82(Series D):35–45, 1960.

[56] R. Fruhwirth. Application of Kalman filtering to track and vertex fitting. *Nucl. Instrum. Meth.*, A262:444–450, 1987.

[57] G. Piacquadio, K. Prokofiev, and A. Wildauer. Primary vertex reconstruction in the ATLAS experiment at LHC. *J. Phys. Conf. Ser.*, 119:032033, 2008.

[58] ATLAS Collaboration. Electron performance measurements with the ATLAS detector using the 2010 LHC proton–proton collision data. *Eur. Phys. J. C*, 72:1909, 2012.

[59] ATLAS Collaboration. Measurement of the muon reconstruction performance of the ATLAS detector using 2011 and 2012 LHC proton–proton collision data. *Eur. Phys. J. C*, 74:3130, 2014.

[60] M. Cacciari, G. P. Salam, and G. Soyez. The Anti-k(t) jet clustering algorithm. *JHEP*, 04:063, 2008.

[61] ATLAS Collaboration. Jet energy measurement with the ATLAS detector in proton–proton collisions at $\sqrt{s} = 7$ TeV. *Eur. Phys. J. C*, 73:2304, 2013.

[62] S. Catani, F. Krauss, R. Kuhn, and B. R. Webber. QCD matrix elements + parton showers. *JHEP*, 11:063, 2001.

[63] J. Alwall et al. Comparative study of various algorithms for the merging of parton showers and matrix elements in hadronic collisions. *Eur. Phys. J.*, C53:473–500, 2008.

[64] J. Baglio et al. Release Note - VBFNLO 2.7.0. 2014.

[65] K. Arnold et al. VBFNLO: A Parton Level Monte Carlo for Processes with Electroweak Bosons – Manual for Version 2.5.0. 2011.

[66] K. Arnold et al. VBFNLO: A Parton level Monte Carlo for processes with electroweak bosons. *Comput. Phys. Commun.*, 180:1661–1670, 2009.

[67] P. Nason. A New method for combining NLO QCD with shower Monte Carlo algorithms. *JHEP*, 11:040, 2004.

[68] S. Frixione, P. Nason, and C. Oleari. Matching NLO QCD computations with Parton Shower simulations: the POWHEG method. *JHEP*, 11:070, 2007.

[69] S. Alioli, P. Nason, C. Oleari, and E. Re. A general framework for implementing NLO calculations in shower Monte Carlo programs: the POWHEG BOX. *JHEP*, 06:043, 2010.

[70] T. Gleisberg et al. Event generation with SHERPA 1.1. *JHEP*, 02:007, 2009.

[71] B. P. Kersevan and E. Richter-Was. The Monte Carlo event generator AcerMC versions 2.0 to 3.8 with interfaces to PYTHIA 6.4, HERWIG 6.5 and ARIADNE 4.1. *Comput. Phys. Commun.*, 184:919–985, 2013.

[72] T. Stelzer and W. F. Long. Automatic generation of tree level helicity amplitudes. *Comput. Phys. Commun.*, 81:357–371, 1994.

[73] T. Sjostrand, S. Mrenna, and P. Z. Skands. PYTHIA 6.4 Physics and Manual. *JHEP*, 05:026, 2006.

[74] T. Sjostrand, S. Mrenna, and P. Z. Skands. A Brief Introduction to PYTHIA 8.1. *Comput. Phys. Commun.*, 178:852–867, 2008.

[75] C Gennaro et al. Herwig 6: an event generator for hadron emission reactions with interfering gluons (including supersymmetric processes). *Journal of High Energy Physics*, 2001(01):010, 2001.

[76] J. M. Butterworth, J. R. Forshaw, and M. H. Seymour. Multiparton interactions in photoproduction at HERA. *Z. Phys.*, C72:637–646, 1996.

[77] J. M. Butterworth and J. R. Forshaw. Photoproduction of multi-jet events at hera: a monte carlo simulation. *Journal of Physics G: Nuclear and Particle Physics*, 19(10):1657, 1993.

[78] S. Frixione and B. R. Webber. Matching NLO QCD computations and parton shower simulations. *JHEP*, 06:029, 2002.

[79] E. Barberio, B. van Eijk, and Z. Was. PHOTOS: A Universal Monte Carlo for QED radiative corrections in decays. *Comput. Phys. Commun.*, 66:115–128, 1991.

[80] S. Agostinelli et al. GEANT4: A Simulation toolkit. *Nucl. Instrum. Meth.*, A506:250–303, 2003.

[81] ATLAS Collaboration. Summary of ATLAS Pythia 8 tunes. ATL-PHYS-PUB-2012-003, 2012.

[82] J. M. Campbell, R. K. Ellis, P. Nason, and G. Zanderighi. W and Z bosons in association with two jets using the POWHEG method. *JHEP*, 08:005, 2013.

[83] S. Alioli, P. Nason, C. Oleari, and E. Re. Vector boson plus one jet production in POWHEG. *JHEP*, 01:095, 2011.

[84] K. Hamilton, P. Nason, and G. Zanderighi. MINLO: Multi-Scale Improved NLO. *JHEP*, 10:155, 2012.

[85] J. Butterworth et al. Single Boson and Diboson Production Cross Sections in pp Collisions at sqrts=7 TeV. Technical Report ATL-COM-PHYS-2010-695, CERN, Geneva, Aug 2010.

[86] M. Cacciari, M. Czakon, M. Mangano, A. Mitov, and P. Nason. Top-pair production at hadron colliders with next-to-next-to-leading logarithmic soft-gluon resummation. *Phys.Lett.*, B710:612–622, 2012.

[87] P. Baernreuther, M. Czakon, and A. Mitov. Percent Level Precision Physics at the Tevatron: First Genuine NNLO QCD Corrections to $q\bar{q} \to t\bar{t} + X$. *Phys.Rev.Lett.*, 109:132001, 2012.

[88] M. Beneke, P. Falgari, S. Klein, and C. Schwinn. Hadronic top-quark pair production with NNLL threshold resummation. *Nucl.Phys.*, B855:695–741, 2012.

[89] M. Czakon, P. Fiedler, and A. Mitov. The total top quark pair production cross-section at hadron colliders through $O(\alpha_S^4)$. 2013.

[90] M. Czakon and A. Mitov. NNLO corrections to top pair production at hadron colliders: the quark-gluon reaction. *JHEP*, 1301:080, 2013.

[91] M. Czakon and A. Mitov. NNLO corrections to top-pair production at hadron colliders: the all-fermionic scattering channels. *JHEP*, 1212:054, 2012.

[92] M. Czakon and A. Mitov. Top++: A Program for the Calculation of the Top-Pair Cross-Section at Hadron Colliders. 2011.

[93] P. Kant et al. HatHor for single top-quark production: Updated predictions and uncertainty estimates for single top-quark production in hadronic collisions. *Comput. Phys. Commun.*, 191:74–89, 2015.

[94] M. Aliev et al. HATHOR: HAdronic Top and Heavy quarks crOss section calculatoR. *Comput.Phys.Commun.*, 182:1034–1046, 2011.

[95] ATLAS Collaboration. Performance of the ATLAS Electron and Photon Trigger in *pp* Collisions at $\sqrt{s} = 7$ TeV in 2011. ATLAS-CONF-2012-048, 2012.

[96] ATLAS Collaboration. Performance of the ATLAS muon trigger in *pp* collisions at $\sqrt{s} = 8$ TeV. *Eur. Phys. J. C*, 75:120, 2015.

[97] ATLAS Collaboration. Tagging and suppression of pileup jets with the ATLAS detector. ATLAS-CONF-2014-018, 2014.

[98] ATLAS Collaboration. Measurement of the electroweak production of dijets in association with a Z-boson and distributions sensitive to vector boson fusion in proton–proton collisions at $\sqrt{s} = 8$ TeV using the ATLAS detector. *JHEP*, 1404:031, 2014.

[99] ATLAS Collaboration. Electron and photon energy calibration with the ATLAS detector using LHC Run 1 data. *Eur. Phys. J. C*, 74:3071, 2014.

[100] ATLAS Collaboration. Electron efficiency measurements with the ATLAS detector using the 2012 LHC proton–proton collision data. ATLAS-CONF-2014-032, 2014.

[101] ATLAS Collaboration. Monte Carlo Calibration and Combination of In-situ Measurements of Jet Energy Scale, Jet Energy Resolution and Jet Mass in ATLAS. ATLAS-CONF-2015-037, 2015.

[102] ATLAS Collaboration. Determination of the jet energy scale and resolution at ATLAS using Z/γ–jet events in data at $\sqrt{s} = 8$ TeV. ATLAS-CONF-2015-057, 2015.

[103] ATLAS Collaboration. Pile-up subtraction and suppression for jets in ATLAS. ATLAS-CONF-2013-083, 2013.

[104] A Dattagupta et al. Observation and measurement of Electroweak W + 2 jets production at high dijet mass. (ATL-COM-PHYS-2014-413), May 2014.

[105] ATLAS Collaboration. Improved luminosity determination in pp collisions at $\sqrt{s} =$ 7 TeV using the ATLAS detector at the LHC. *Eur. Phys. J. C*, 73:2518, 2013.

[106] ATLAS Collaboration. Luminosity Determination in pp Collisions at $\sqrt{s} = 8$ TeV using the ATLAS Detector at the LHC. (ATL-COM-DAPR-2015-014), Aug 2015. Journal draft for EdBoard review.

[107] Atlas twiki: Tgclim package (internal). `https://twiki.cern.ch/twiki/bin/view/AtlasProtected/TGClimPackage`. Accessed: 2016-04-25.

[108] G. Ranucci. The Profile likelihood ratio and the look elsewhere effect in high energy physics. *Nucl. Instrum. Meth.*, A661:77–85, 2012.

[109] ATLAS Collaboration. Measurement of total and differential W^+W^- production cross sections in proton-proton collisions at $\sqrt{s} = 8$ TeV with the ATLAS detector and limits on anomalous triple-gauge-boson couplings. 2016.

[110] M. Acciarri et al. Production of single W bosons at $\sqrt{S} = 189$-GeV and measurement of $WW\gamma$ gauge couplings. *Phys. Lett.*, B487:229–240, 2000.

[111] S. Schael et al. Electroweak Measurements in Electron-Positron Collisions at W-Boson-Pair Energies at LEP. *Phys. Rept.*, 532:119–244, 2013.

[112] V. M. Abazov et al. Limits on anomalous trilinear gauge boson couplings from WW, WZ and $W\gamma$ production in $p\bar{p}$ collisions at $\sqrt{s} = 1.96$ TeV. *Phys. Lett.*, B718:451–459, 2012.

[113] T. Aaltonen et al. Measurement of the WZ Cross Section and Triple Gauge Couplings in $p\bar{p}$ Collisions at $\sqrt{s} = 1.96$ TeV. *Phys. Rev.*, D86:031104, 2012.

[114] ATLAS Collaboration. Measurements of $W^{\pm}Z$ production cross sections in pp collisions at $\sqrt{s} = 8$ TeV with the ATLAS detector and limits on anomalous gauge boson self-couplings. 2016.

[115] CMS Collaboration. Measurement of the W^+W^- cross section in pp collisions at $\sqrt{s} = 8$ TeV and limits on anomalous gauge couplings. 2015.